

Atomistic Understanding of Two-dimensional Electrocatalysts from First Principles

Xunhua Zhao, Zachary H Levell, Saerom Yu, and Yuanyue Liu*

Cite This: *Chem. Rev.* 2022, 122, 10675–10709

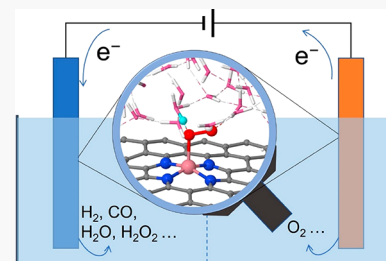
Read Online

ACCESS |

Metrics & More

Article Recommendations

ABSTRACT: Two-dimensional electrocatalysts have attracted great interest in recent years for renewable energy applications. However, the atomistic mechanisms are still under debate. Here we review the first-principles studies of the atomistic mechanisms of common 2D electrocatalysts. We first introduce the first-principles models for studying heterogeneous electrocatalysis then discuss the common 2D electrocatalysts with a focus on N doped graphene, single metal atoms in graphene, and transition metal dichalcogenides. The reactions include hydrogen evolution, oxygen evolution, oxygen reduction, and carbon dioxide reduction. Finally, we discuss the challenges and the future directions to improve the fundamental understanding of the 2D electrocatalyst at atomic level.



CONTENTS

1. Introduction	10675
2. Methods	10676
2.1. Computational Hydrogen Electrode Model (CHEM)	10676
2.2. Constant-potential Models	10678
2.3. Explicit Solvation	10679
2.4. Reaction Kinetics	10680
3. Hydrogen Evolution Reaction (HER)	10680
3.1. MX_2	10680
3.2. X–C	10685
3.3. M–X–C	10685
4. Oxygen Evolution Reaction (OER)	10685
5. Oxygen Reduction Reaction (ORR)	10687
5.1. 4e Reaction	10687
5.1.1. X–C	10687
5.1.2. M–X–C	10689
5.2. 2e Reaction	10693
5.2.1. M–X–C	10693
5.2.2. X–C	10695
6. Carbon Dioxide Reduction (CO_2R)	10698
6.1. M–X–C	10698
6.2. X–C	10701
6.3. MX_2	10702
7. Conclusion and Perspective	10702
Author Information	10703
Corresponding Author	10703
Authors	10703
Notes	10704
Biographies	10704
Acknowledgments	10704
References	10704

1. INTRODUCTION

Electrochemistry at the interface between solid and water is ubiquitous in nature and is at the center of many technologies promising to address the energy and environmental issues. For example, hydrogen fuel cells utilize electrochemical oxygen reduction reaction (ORR) and hydrogen oxidation reaction (HOR) to convert H_2 fuels to electricity; water electrolysis uses hydrogen evolution reaction (HER) and oxygen evolution reaction (OER) to get H_2 fuel from electricity. Electrochemical carbon dioxide reduction (CO_2R) can convert CO_2 , which causes the greenhouse effect, to value-added products such as CO, methanol, ethanol, etc.

To improve these technologies, it is critical to have highly active, selective, stable, and cost-effective electrocatalysts to accelerate the reactions. Two-dimensional (2D) materials have emerged as promising candidates. These materials have a thickness of only one/few atomic layer(s) and possess unconventional physical and chemical properties. Various 2D materials have demonstrated electrocatalytic performance comparable or exceeding the conventional catalysts for a variety of reactions. For example, Linyou Cao et al.¹ reported that monolayer MoS_2 , with an optimal density of S vacancies and crumpled on Ti coated flexible polymer substrates, has a better catalytic activity for HER than Pt and shows no degradation in performance after being continuously tested for over 2 months. Myers, Xie, Cullen, Litster, and Wu et al.² showed that single Fe

Special Issue: Computational Electrochemistry

Received: November 23, 2021

Published: May 13, 2022



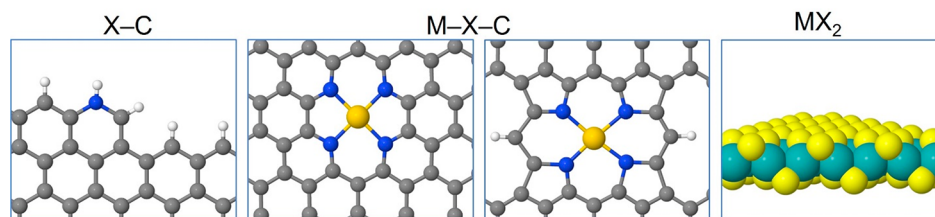


Figure 1. Common types of 2D electrocatalysts. X–C, nonmetal-element (e.g., N) doped graphene; M–X–C, single metal atom embedded in graphene or X doped graphene; MX₂, transition metal dichalcogenides.

atoms coordinated by N in graphene, synthesized by depositing N–C species on the catalyst surface via chemical vapor deposition, demonstrated competitive activity to that of Pt/C catalysts and dramatically enhanced stability and durability under practical operating conditions in proton exchange membrane fuel cells (PEMFCs). To further develop these catalysts, it is important to have a deep understanding of the atomistic mechanism.

There are numerous 2D materials, and many other reviews^{3–7} have covered their synthesis, characterizations, and electrocatalytic performance, mainly from an experimental perspective. Here we review the theoretical mechanistic understanding of the common 2D electrocatalysts and the corresponding reactions. The common types of 2D electrocatalysts include (Figure 1): X doped graphene (X–C, where X is a nonmetal element and often N), single metal atom embedded in graphene or X doped graphene (M–X–C, where M represents a metal element), and transition metal dichalcogenides (MX₂). These 2D materials have been extensively reported as electrocatalysts for HER, OER, ORR (both 4-electron and 2-electron pathways), and CO₂R. For each reaction and catalyst type, we focus on the most common material in experiments. For example, among X–C for ORR, N–C is the most common catalyst and thus is our focus, although codoping with multiple elements in graphene has also been reported. It should be noted that although these materials have been extensively studied, there is still much debate on the catalytic mechanism. Therefore, it is valuable to review the current understandings on these “model” catalysts. Such understandings may also be useful to less common 2D electrocatalysts or even conventional non-2D catalysts.

First-principles methods, especially density function theory (DFT), are powerful tools to obtain an atomistic understanding of the materials and processes.^{8–11} They have been widely used to study catalysis. Compared with thermocatalysis, where the models for first-principles calculations are relatively simple, the electrocatalysis at solid–liquid interface is much more complicated due to dynamic electronic charge on surface and solvation effects. Consequently, there exist different models for first-principles calculations, which differ by different approximations to the complex system. These models sometimes give very different understandings of the electrocatalysis. This disagreement also motivates us to review the current first-principles models and the understandings from them, especially for 2D electrocatalysts.

This review is organized in the following way: first we review the first-principles models for studying heterogeneous electrochemistry. Then we will review four reactions, HER, OER, CO₂R, and ORR; for each reaction, we will focus on the atomistic understandings brought by the first-principles calculations for the most common 2D electrocatalysts. Finally, we will give a perspective on how to move the field forward.

2. METHODS

2.1. Computational Hydrogen Electrode Model (CHEM)

The computational hydrogen electrode model (CHEM) is popularized by Nørskov et al.¹² and has been widely used to study electrocatalysis. To introduce this model, we consider a simple example, the Volmer reaction in acidic water:



where the H⁺_{aq} represents a proton in the aqueous solution, * represents a catalyst, and H* denotes the catalyst with adsorbed H. One of the most important questions is what is the free energy difference between the reactants and the product, i.e., the free energy change for the reaction (ΔG)? If one knows the free energy of each species involved in the reaction, then ΔG is simply:

$$\Delta G = G(\text{H}^*) - G(*) - G(\text{H}^+_{\text{aq}}) - \mu_{\text{e}} \quad (2)$$

Here the G(H⁺_{aq}) depends on the pH of the solution following the Nernst equation,

$$G(\text{H}^+_{\text{aq}}(\text{pH})) = G(\text{H}^+_{\text{aq}}(\text{pH} = 0)) - 0.059\text{pH} \quad (3)$$

The chemical potential (Fermi level) of electrons depends on the electrode potential. If the electrode potential is *U* referenced to the standard hydrogen electrode (SHE), then:

$$\mu_{\text{e}}(U_{\text{SHE}}) = \mu_{\text{e}}(0_{\text{SHE}}) - |e|U_{\text{SHE}} \quad (4)$$

Substituting eqs 2 and 3 into eq 1, we have

$$G = G(\text{H}^*) - G(*) - G(\text{H}^+_{\text{aq}}(\text{pH} = 0)) - \mu_{\text{e}}(0_{\text{SHE}}) + 0.059\text{pH} + |e|U_{\text{SHE}} \quad (5)$$

where pH and *U*_{SHE} are the preset parameters, μ_e(0_{SHE}) is experimentally measured to be $-(4.44 \pm 0.02)$ eV at 298.15 K with respect to vacuum level¹³ (which happens to be canceled in this case as shown later).

The G(H*), G(*), and G(H⁺_{aq}) terms can be calculated from first-principles methods such as density functional theory (DFT). In principle, these calculations should include the solution in the models. However, it will significantly increase the computational cost as the liquid solution has numerous atomic configurations that are difficult to sample sufficiently. Thus, as an approximation, one can neglect the solvation effect or use the implicit solvation method (which often treats the solution as continuous medium and is computationally much cheaper than the full explicit solvation) for G(H*) and G(*). However, it is still difficult to determine the G(H⁺_{aq}(0)) from first-principles, which not only involves the solvation (which is strong) but also the proton concentration. To avoid direct calculation of the G(H⁺_{aq}(0)), one can deduce it from the reaction where the energies of other species can be more easily calculated or are

experimental measured. Such reaction can be that in the SHE, where the following thermodynamic equilibrium exists:

$$G(\text{H}^+_{\text{aq}}(0)) + \mu_e(0_{\text{SHE}}) = G(\text{H}_2)/2 \quad (6)$$

where H_2 is at the standard state (room temperature and 1 atm). The free energy of gas is usually easier to calculate from first-principles (or in conjunction with experimental data) than the solvated species. Substituting eq 6 into eq 5, we get:

$$\Delta G = G(\text{H}^*) - G(*) - G(\text{H}_2)/2 + 0.059\text{pH} + |e|U_{\text{SHE}} \quad (7)$$

All of the terms on the right side are available and thus ΔG can be obtained. Note that the energy given by many first-principles computation software is often the total energy of a fixed-nuclei structure under Born–Oppenheimer approximation. To get the free energy, one also needs to include the vibration, rotation, and translation contributions.

The potential is also often referenced to the reversible hydrogen electrode (RHE). Unlike SHE, the μ_e is not fixed but varies with pH so that

$$G(\text{H}^+_{\text{aq}}(\text{pH})) + \mu_e(0_{\text{RHE}}) = G(\text{H}_2)/2 \quad (8)$$

Thus:

$$\begin{aligned} \mu_e(U_{\text{RHE}}) &= \mu_e(0_{\text{RHE}}) - |e|U_{\text{RHE}} \\ &= G(\text{H}_2)/2 - G(\text{H}^+_{\text{aq}}(\text{pH})) - |e|U_{\text{RHE}} \end{aligned} \quad (9)$$

By substituting eq 9 into eq 2, we have

$$\Delta G = G(\text{H}^*) - G(*) - G(\text{H}_2)/2 + |e|U_{\text{RHE}} \quad (10)$$

This equation suggests that if U_{RHE} is fixed, then the ΔG does not change with pH.

The example given above considers an acid condition. Under neutral or alkaline condition, the H source is a water molecule instead of hydronium. Thus, the Volmer reaction should be written as



where the subscript “1” denotes liquid state. The free energy change should be calculated as

$$\Delta G = G(\text{H}^*) + G(\text{OH}^-_{\text{aq}}) - G(*) - G(\text{H}_2\text{O}_1) - \mu_e \quad (12)$$

Under thermodynamic equilibrium of water self-ionization, we have

$$G(\text{H}^+_{\text{aq}}) + G(\text{OH}^-_{\text{aq}}) = G(\text{H}_2\text{O}_1) \quad (13)$$

By substituting eq 13 into eq 12, the $G(\text{H}_2\text{O}_1)$ will disappear, and we will recover eq 2 and eventually get eq 7 or 10 depending on the reference of the potential. This indicates that different H sources do not change the forms of these two equations.

The essence of the CHEM is that the free energy of solvated ion, which is difficult to directly calculate from first-principles, can be deduced from the equilibrium reaction where the energies of other species can be more easily calculated or have been experimentally measured. This idea is not limited to a proton but can be extended to other ions.¹⁴ For example, the free energy of 1 M Fe^{2+} in aqueous solution can be obtained through the reaction at equilibrium:



where the subscript “s” denotes the solid state. Therefore:

$$G(\text{Fe}^+_{\text{aq}}) = G(\text{Fe}_s) - 2\mu_e \quad (15)$$

The μ_e here is defined by the standard electrode potential for eq 14, which is -0.44 V vs SHE (i.e., $\mu_e = -4.00$ eV). The $G(\text{Fe}_s)$ can be calculated from first principles. With these two quantities, the $G(\text{Fe}^+_{\text{aq}})$ can be readily determined.

As another example of the application of CHEM, we consider a step of ORR in acidic aqueous solution:



Its free energy change is

$$\begin{aligned} \Delta G &= G(\text{OH}^*) + G(\text{H}_2\text{O}_1) - G(*\text{OOH}) - G(\text{H}^+_{\text{aq}}) \\ &\quad - \mu_e \end{aligned} \quad (17)$$

Following the previous derivation, this equation can be converted to a form that is computationally more feasible:

$$\begin{aligned} \Delta G &= G(\text{OH}^*) + G(\text{H}_2\text{O}_1) - G(*\text{OOH}) - G(\text{H}_2)/2 \\ &\quad + |e|U_{\text{RHE}} \end{aligned} \quad (18)$$

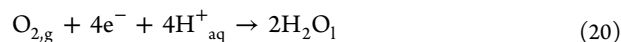
where the $G(\text{OH}^*)$, $G(*\text{OOH})$, and $G(\text{H}_2)$ can be easily calculated from first principles. To get the $G(\text{H}_2\text{O}_1)$ (the free energy of liquid water at room temperature), we again can take the advantage of the equilibrium:



where H_2O_g is the gas state with room-temperature vapor pressure, whose free energy can be more easily obtained than the liquid phase. With all these quantities, we can calculate the ΔG for reaction 16 through eq 18.

In practice, for a reaction with multiple steps, one can use the CHEM to calculate the free energy change of each step under a preset potential. On the basis of these free energy changes, one can obtain the free energies of the intermediates referenced to the reactants of the first step. These relative free energies can be put together in a diagram (“thermodynamic free energy diagram”) to compare the thermodynamics of each step. Often, the potential is set to be the equilibrium potential for that reaction (e.g., 0 V vs RHE for HER). In this case, the free energy of the final state in the diagram will be identical to that of the initial state. Using this diagram, one can identify the “thermodynamic rate-limiting step”, which is the step that gives the highest free energy increase (or least free energy decrease). Also, one can calculate the “thermodynamic onset potential”, which is the potential that drives all the steps downhill in thermodynamics.

It should be noted that first-principles methods such as DFT may not well reproduce the experimental equilibrium potential for an electrochemical reaction. For example, the standard electrode potential for 4e ORR:



calculated from DFT (PAW pseudopotential, PBE functional) is only 1.14 V, different from the experimental value 1.23 V. In other words, in the thermodynamic free energy diagram calculated by summing up the free energy changes of individual steps calculated under the experimental equilibrium potential, the final state ($* + 2\text{H}_2\text{O}$) will be higher than the initial state ($* + \text{O}_2 + 4e$) by $(1.23 - 1.14) * 4 = 0.36$ eV. The mismatch is mainly because the PBE functional is not able to accurately describe the

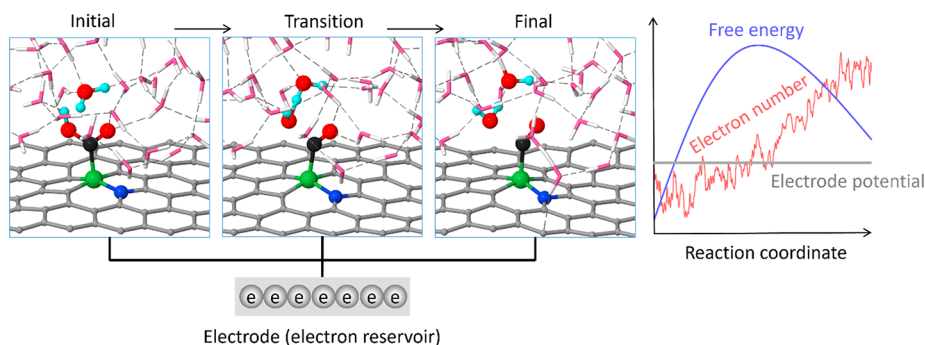


Figure 2. Schematics of the elementary steps of electrochemistry at solid–liquid interface under constant electrode potential. Consequently, the number of electrons at the interface fluctuates and evolves along the reaction pathway. This is different from thermal reactions with constant electron number.

electronic energy of the O_2 molecule. To avoid this problem, most literature often manually correct the energy of the reactant or product. In the case of ORR, the $G(O_{2,g})$ is corrected as

$$\begin{aligned} G(O_{2,g}) &= 2G(H_2O_l) - G(4H^+_{aq}) - G(4e^-) \\ &= 2G(H_2O_l) - 2G(H_{2,g}) + 4 \times 1.23 \text{ eV} \end{aligned} \quad (21)$$

where the $G(H_2O_l)$ is determined from eq 19. By this way, the final state ($* + 2H_2O$) of 4e ORR will have exactly the same energy as the initial state ($* + O_{2,g} + 4e^- + 4H^+_{aq}$) under the experimental equilibrium potential (1.23 V), so that one does not need to calculate the free energy change for the last step. The correction applied to O_2 energy is 0.38 eV for PBE functional, which could make a significant difference in the O_2 adsorption step.

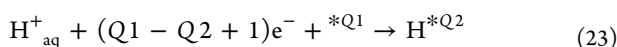
For another example, the standard electrode potential for CO_2 reduction to CO:



calculated from DFT (PAW pseudopotential, PBE functional) is -0.29 V, which is different from the experimental value -0.11 V. To avoid this problem, most literature manually set the free energy of the final state ($* + CO_g + H_2O_l$) to be same as that of the initial state ($* + CO_2 + 2e^- + 2H^+_{aq}$), under the experimental equilibrium potential of -0.11 V. Thus, the free energy change of the last step (which can be either $*CO \rightarrow CO_g$, or $*COOH + e^- + H^+_{aq} \rightarrow CO_g + H_2O_l$, depending on if CO can be chemically adsorbed on the $*$ or not) does not need to be explicitly calculated.

2.2. Constant-potential Models

There are several issues for the CHEM. The first issue is that when calculating $G(*)$ and $G(*ad)$ (where “ad” represents an adsorbed species), the catalyst (w/ or w/o adsorbate) is assumed to be charge neutral. However, in reality, the catalyst is charged due to the exchange of electrons between the catalyst and the electrode to reach the equilibrium for electrons, as illustrated in Figure 2. Under equilibrium, the Fermi level (E_F) of the catalyst should match that of the electrode, which is defined by the electrode potential (U). Moreover, for an elementary step, the U is fixed and thus the E_F is fixed (giving the name “constant potential”). To emphasize the charge on the catalyst, let us rewrite eq 1 as



where $Q1$ and $Q2$ are the charges in the systems of $*$ and H^* . Note that to balance the charge, the number of electrons involved becomes $Q1 - Q2 + 1$ instead of 1. Then the free energy change should be calculated as

$$\begin{aligned} \Delta G &= G(H^*Q2) - G(*Q1) - G(H^+_{aq}) \\ &\quad - (Q1 - Q2 + 1)\mu_e \end{aligned} \quad (24)$$

Following the derivation in the previous section, we will get:

$$\begin{aligned} \Delta G &= G(H^*Q2) - G(*Q1) - G(H_2)/2 + 0.059pH \\ &\quad + |e|U - (Q1 - Q2)\mu_e \end{aligned} \quad (25)$$

By comparing with eq 7, in order to account for the net electronic charges (which are often located on the surface and are thus referred as surface charges), we not only need to recalculate the free energy of catalyst (with and without adsorbate) under charge but also must add the correction of $-(Q1 - Q2)\mu_e$.

The immediate question is how to determine the charge for the catalyst, or generally speaking, the surface charge on the solid in electrochemical condition. An intuitive approach is to tune the number of electrons of the solid until its E_F matches that of the electrode¹⁵ (alternatively, one can also solve the Kohn–Sham equations of electronic DFT directly in the grand canonical ensemble at fixed potential¹⁶). For an electrode potential of U_{SHE} , the target E_F is set by eq 4. The problem is how do we know the E_F of solid referenced to the $\mu_e(0_{SHE})$?

To solve this problem, one can use a common reference, the electrostatic potential in the bulk solution, to measure both the E_F and the $\mu_e(0_{SHE})$. In reality, the net electronic charges on the solid will attract opposite ionic charges in the solution, forming an electrostatic potential profile that converges to a constant with increasing distance from the solid. This behavior can be reproduced in simulation by combining DFT with the implicit solvation model that contains mobile ions, where the solid (and relevant species involved in the reaction) are treated by DFT and the solution (or part of it) is treated as an atomic-structureless medium. One can extract the converged electrostatic potential in the implicit region and use it as a reference to measure the E_F .

The challenge is to get the $\mu_e(0_{SHE})$ in reference to the electrostatic potential in the bulk solution. In principle, if one knows the atomic structure of the solid surface and its net electronic charge in the SHE, one can obtain it from the DFT in conjunction with implicit solvation model as described in the last paragraph. While such information may be unambiguous, it

can alternatively be obtained by combining DFT with experimental data. First, one can calculate the solution-referenced Fermi level for a charge-neutral metal surface ($\mu_{e,PZC}$ vs solution), where the potential of zero charge (PZC) vs SHE is experimentally known as ΔU_{PZC} . Assuming that the DFT correctly reproduces the μ_e of such system, the solution-referenced Fermi level for SHE will be

$$\mu_e(0_{SHE}) \text{ vs solution} = \mu_{e,PZC} \text{ vs solution} - |e|\Delta U_{PZC} \quad (26)$$

In practice, one can consider multiple metal surfaces, plot their $\mu_{e,PZC}$ vs solution with respect to the $|e|\Delta U_{PZC}$, and linearly fit the data points by fixing the slope to be 1. The intercept will be $\mu_e(0_{SHE})$ vs solution. With this quantity in hand, one can determine the value of the $\mu_e(U_{SHE})$ vs solution for any U_{SHE} (eq 4). Now we have referenced both the E_F of the solid and the $\mu_e(U_{SHE})$ to the solution; by matching them, one can obtain the net electronic charge of the system.

There are different implicit models for the solvent and/or the ionic charge, which can give different E_F and $\mu_e(0_{SHE})$ vs solution. In general, the implicit solvation models can be classified into two types:¹⁷ the continuum model (e.g., polarizable continuum model (PCM), conductor-like screening model (COSMO)), the structured implicit model (e.g., the reference interaction site method (RISM), and the classical density-functional theory (classical-DFT)). The ionic charge can be distributed in the form of a plane/slab or, more physically, through the Poisson–Boltzmann (PB) model or the modified Poisson–Boltzmann (MPB) model. For example, Otani et al.¹⁸ developed the “effective screening medium” (ESM) method. The atomic region is sandwiched between two semi-infinite continuous media, which can be vacuum, dielectric, or metal, by imposing proper boundary conditions and using Green’s function technique. When modeling the charged solid surface, the counter charge is distributed on the surface of “metal” region.¹⁹ The ESM method is recently combined with the RISM solvation model for the counter charge distribution.²⁰ Peterson et al.²¹ proposed a “solvated jellium” model. The counter charge is distributed as a “jellium” in a slab, which is placed on top of the explicit atomic region and contains implicit solvent. Todorova et al.²² distributed the counter charge on an explicit layer of Ne atoms, which has a large band gap. By tuning the nuclear charges of the Ne atoms, the electrons can transfer from the solid to the Ne layer or vice versa, thereby charging the solid. Richard Hennig et al. developed a “VASPsol” solvation model²³ and extended it by using the linearized PB equation to describe the ionic charge distribution in the solution.²⁴ Using PAW pseudopotential and PBE functional, they obtained -4.6 eV for $\mu_e(0_{SHE})$ vs solution. Ravishankar Sundararaman et al. developed a “charge-asymmetric nonlocally determined local-electric” (CANDLE) solvation model²⁵ and treated the counter charge distribution by the linearized PB equation.¹⁶ These methods are implemented in the software JDFTx.²⁶ They benchmarked the $\mu_e(0_{SHE})$ vs solution to be -4.66 eV, using PBE functional and the GBRV ultrasoft pseudopotentials. Nicola Marzari et al.²⁷ described the solvent via the self-consistent continuum solvation (SCCS) model, and the ionic charge is distributed on a Gaussian-shaped plane.

These approaches all distribute the ionic charge in a limited region. A different approach is to distribute it uniformly through the unit cell, which is the default option in many first-principles calculation software. However, the uniformly distributed background charge does not provide a region where the electric

field is screened entirely. Hence, this approach lacks a reasonable reference for the E_F . Neurock et al.²⁸ addressed this issue and developed a method known as the “double reference method”. In this method, a layer of water far from the solid surface is fixed in position. Assuming the electrostatic potential of this water layer (ϕ_w) remains unchanged regardless of the solid charge, one can use it as a reference to calculate the relative position of the Fermi level. Because the relative difference between the ϕ_w and the vacuum level can be obtained from the system without net electronic charge, one can obtain the Fermi level referenced to vacuum level for charged solid.

These methods directly introduce the net electronic charge into the supercell and tune it to reach the desired Fermi level. Alternatively, one can also correct the energetics of the charge-neutral or constant-charge simulation to include the effect of constant potential. For example, Rossmel et al.²⁹ developed a “cell-extrapolation” method by calculating reaction energetics in increasingly larger sized supercells. Nørskov et al.³⁰ developed a “charge-extrapolation” method, using only one supercell at constant charge. The assumptions are that the “chemical” and electrostatic contributions to reaction energetics are separable, and the electrostatic contributions are described by a basic capacitor model. Goddard et al.³¹ developed a “grand canonical potential kinetics (GCP-K)” method. It first calculates the reaction energetics at different charges and then transforms the free energy to that under constant potential.

The effect of surface charge/constant potential can be significant in heterogeneous electrochemistry. Particularly, if the charge significantly changes the site’s electronic structure, or the occupation of its electronic states, then the charge will strongly change the site’s reactivity. This is the case for many low-dimensional electrocatalysts, which usually have a low density of electronic states (i.e., low quantum capacitance). Thus, a small amount of charge can significantly shift the relative position of Fermi level or directly modify the electronic structure. For example, Liu et al.³² showed that the *H formation energy on N dopant in graphene can change by >1 eV after the surface charge effect is considered. Therefore, when studying 2D electrocatalysts, it is necessary to consider such effects, which were overlooked in many papers. The importance of surface charge is also manifested through the site’s charge capacity: a higher charge capacity will result in more electrons/holes accumulated at the catalytic site under the working potential, which facilitates the charge transfer to the reaction species and thus lowers the barrier of electrochemical step.³³ The surface charge can also explain some potential-dependent phenomena. For example, for ORR on Co–N₄ catalyst, as the electrode potential decreases, the selectivity of H₂O₂ against hydroxide increases. This is explained by the change in the surface charge: a lower potential gives more negative charges on the catalyst and its adsorbate (*–O–OH), which results in a stronger attraction of H from the water solvent to the former O in *–O–OH, making the intermediate closer to H₂O₂.³⁴

2.3. Explicit Solvation

Another factor that is overlooked in the CHEM is the explicit solvation. Chan et al.³⁵ performed extensive ab initio molecular dynamics (AIMD) simulations to benchmark solvation at charge-neutral metal/water interfaces against commonly applied continuum solvent models. They considered a variety of adsorbates, including *CO, *CHO, *COH, *OCCHO, *OH, and *OOH, on various facets of Cu, Au, and Pt solvated by water. Directional hydrogen bonds and steric water competition

are identified to be critical for a correct description of solvation at the metal/water interfaces. Consequently, they found that the most frequently applied implicit solvation methods, which do not capture these properties, do not provide more accurate energetics over simulations in vacuum. They also found that most of the computed benchmark solvation energies linearly scale with hydrogen bonding or competitive water adsorption, but they strongly differ across surfaces. Thus, they concluded that the solvation energies of adsorbates are nontransferable between metal surfaces, in contrast to standard practice. This work suggests one should evaluate the effect of explicit solvation case by case.

Specifically for 2D electrocatalysts, Wang et al.³⁶ studied the role of the solvent environment in the ORR catalyzed by the Mn–N₄ single atom catalyst using AIMD simulations with explicit water molecules. It is found that the solvent environment facilitates the transformation of O₂ from the end-on configuration to the more stable side-on configuration. Furthermore, the solvent forms hydrogen bonds with the adsorbates, elongates the Mn–O bond, and thus facilitates the protonation for *O and *OH intermediates. Finally, the solvent also changes the thermodynamic free energy diagram. Specifically, to get the structures of explicitly solvated intermediates for building the diagram, for a given intermediate, they first performed a ~12 ps MD simulation to equilibrate the system and then randomly picked several snapshots from the MD simulations without a loss of generality to anneal each snapshot to 0 K and obtain the minimum-energy structure. The most stable structure from the annealing simulations was further optimized and was considered to be the representative structure of the intermediate.

Liu et al.³³ showed that hydrogen bonding plays important roles in CO₂R on Ni–N_xC_y catalyst. First, it stabilizes the chemisorption of CO₂, which would otherwise be physically adsorbed with the linear structure. Second, the hydrogen bonding between water and the polar intermediates help proton transfer from water to the intermediates, which improves the selectivity of the reaction (CO₂R in this case) that produces these intermediates over the HER, whose intermediates do not form hydrogen bonding with water. The importance of the explicit solvation is also demonstrated in the study of ORR selectivity.³⁴ It is found that the selectivity dependence on potential and pH can be explained by the proton affinity to the O in *–O–OH. For the Co–N₄ catalyst, decreasing potential promotes proton adsorption to the O bonded with the site, thereby increasing the H₂O₂ selectivity. In contrast, for the carbon catalyst, the proton prefers the O in OH, leading to a lower H₂O₂ selectivity in acid condition.

2.4. Reaction Kinetics

Another limitation of the CHEM is that it only gives the thermodynamics. However, the reaction rate is more directly related to the kinetics, and thus the kinetic information plays a more decisive role in evaluating the catalyst performance or the feasibility of a catalytic mechanism. Many of the reaction steps directly involve water as a reactant/product, hence it must be explicitly included in the model. For simplicity, many studies consider a couple of or a mono/bilayer of water molecules with preset structures for initial and final states, and then find transition states and their corresponding energy barriers using methods such as nudged elastic band (NEB). The effect of surface charge/constant potential can be incorporated as

described in the last section to obtain the kinetics under the constant potential.

However, using a limited number of water molecules may not sufficiently capture the solvation effect, especially when polar species are involved. Including more water molecules inevitably expand the phase space: multiple water/solvation configurations can exist at a given reaction state, as illustrated in Figure 2. In this case, the “static” barrier-calculation method (e.g., NEB) is not suitable, as it requires well-defined structures for the intimal and final states as input. “Dynamic” methods, such as the “blue moon” approach,³⁷ umbrella sampling,³⁸ and metadynamics³⁹ can be used to evaluate the barrier. These methods sample the phase space of the system and compute the free energy profile along the predefined reaction coordinate(s). It should be noted that the conventional phase space consists of only atomic positions and momenta; for heterogeneous electrochemistry, the phase space needs to be expanded to include the charge states due to the constant potential effect.

Liu et al.³⁴ recently proposed a promising model for atomistic simulation of electrochemical kinetics at solid–water interface. This model, named the “constant potential-hybrid solvation-dynamic model” (CP-HS-DM), includes the dynamic surface charge and explicit solvation and provides the kinetic information especially for electrochemical step. Specifically, this model uses several layers of water molecules for explicit solvation and continuous dielectric medium with ionic charges described by PB model for implicit solvation. It slowly changes the reaction coordinate (ϵ) value from the initial state to the final state by constrained AIMD (slow-growth approach^{40,41}). Accompanying the structure change, the electron number also changes following the grand canonical ensemble under constant potential, as illustrated in Figure 2.⁴² The mean force acting on ϵ is then calculated at every ϵ value and integrated to yield the (relative) free energy based on thermodynamic integration. The CP-HS-DM has been used to study the kinetics of ORR and successfully explains the selective formation of H₂O₂ on certain catalysts.

3. HYDROGEN EVOLUTION REACTION (HER)

HER usually refers to the reaction that electrochemically converts water to H₂: $2\text{H}^+ + 2\text{e}^- \rightarrow \text{H}_2$ (in acidic condition), or $2\text{H}_2\text{O} + 2\text{e}^- \rightarrow \text{H}_2 + 2\text{OH}^-$ (in alkaline or neutral condition). It is the cathodic reaction in (photo)electrochemical water splitting, which is a promising approach to produce H₂, a critical chemical reagent and fuel. The HER proceeds through the following steps (using acid condition as an example): (1) $\text{H}^+ + \text{e}^- \rightarrow * \text{H}$ (Volmer step), (2) $2* \text{H} \rightarrow \text{H}_2$ (Tafel step), or (3) $\text{H}^+ + \text{e}^- + * \text{H} \rightarrow \text{H}_2$ (Heyrovsky step).

3.1. MX₂

Among MX₂, MoS₂ is the most representative catalyst for HER. Therefore, we will focus on MoS₂. Nørskov et al.⁴³ used CHEM to predict that MoS₂ edge is active for HER (Figure 3a) and experimentally verified that MoS₂ nanoparticles supported on graphite are a promising catalyst. The edge activity was confirmed by Chorkendorff et al.,⁴⁴ who synthesized MoS₂ on Au(111) and showed that the activity for HER correlates linearly with the total length of the exposed edges of crystalline MoS₂. Nielsen and Goddard et al.⁴⁵ performed DFT calculations to study the kinetics of HER on the Mo side (10 $\bar{1}$ 0) of the MoS₂ edge (Figure 4). Specifically, they constructed a cluster model (Mo₁₀S₂₁). To describe the solution, they used four H₂O molecules together with the Poisson–Boltzmann implicit

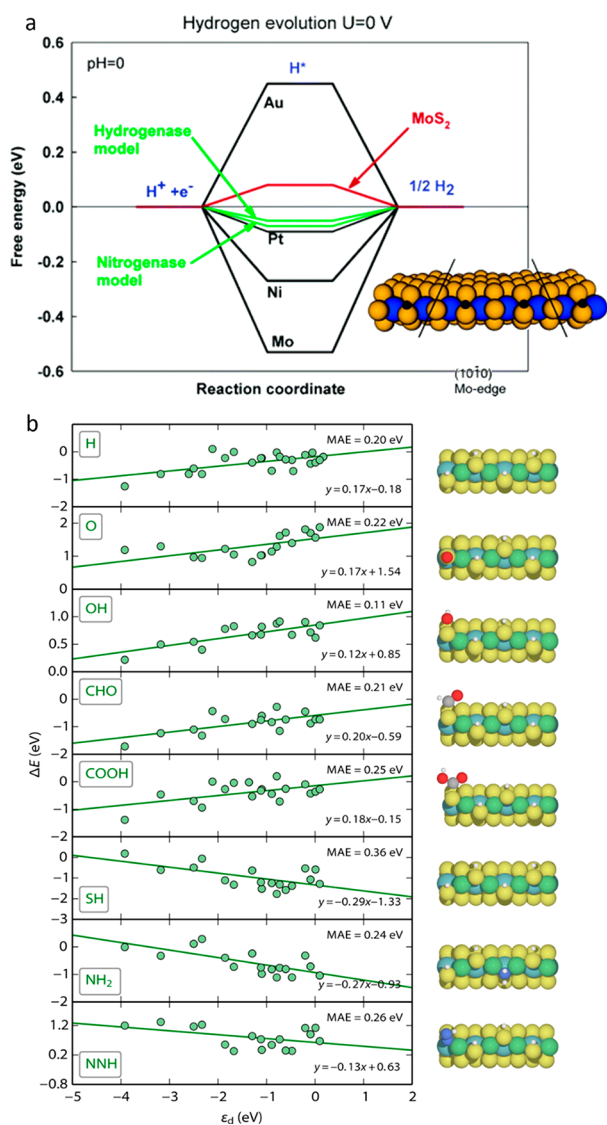


Figure 3. (a) Thermodynamic free energy diagram for HER on MoS₂ edge with the structure shown in the inset (Mo edge with 0.5 ML S coverage and 0.5 ML H coverage). Adapted with permission from ref 43. Copyright 2005 American Chemical Society. (b) Adsorption energy of various key reaction intermediates (ΔE) as a function of the d-band center (ϵ_d). H, O, OH, CHO, and COOH are adsorbed onto S sites at the stable S and H coverages, whereas SH, NH₂, and NNH are adsorbed into a S defect at the stable coverage. Typical adsorption configurations for 0.5 ML S and 0.75 ML H are shown as examples (blue = Mo, yellow = S, green = edge-most metal, white = H, red = O, dark blue = N, gray = C). Adapted with permission from ref 46. Copyright 2014 American Chemical Society.

solution. They found that the reaction proceeds through Volmer–Heyrovsky mechanism as follows: the edge is first reduced by one electron, followed by protonation to create a S-bound H with a small barrier of 0.27 eV. The structure is further reduced by one more electron, followed by the migration of H onto the Mo atom with a relatively high barrier of 0.89 eV. The edge is protonated again by hydronium with a barrier of 0.78 eV. Finally, the metal hydride reacts with a proton from solution, forming dihydrogen with a barrier of 1.02 eV and leaving a positively charged catalyst. The last step is the rate limiting step.

Nørskov et al.⁴⁷ proposed a different reaction pathway (Figure 5). Different from the cluster model used by Goddard et

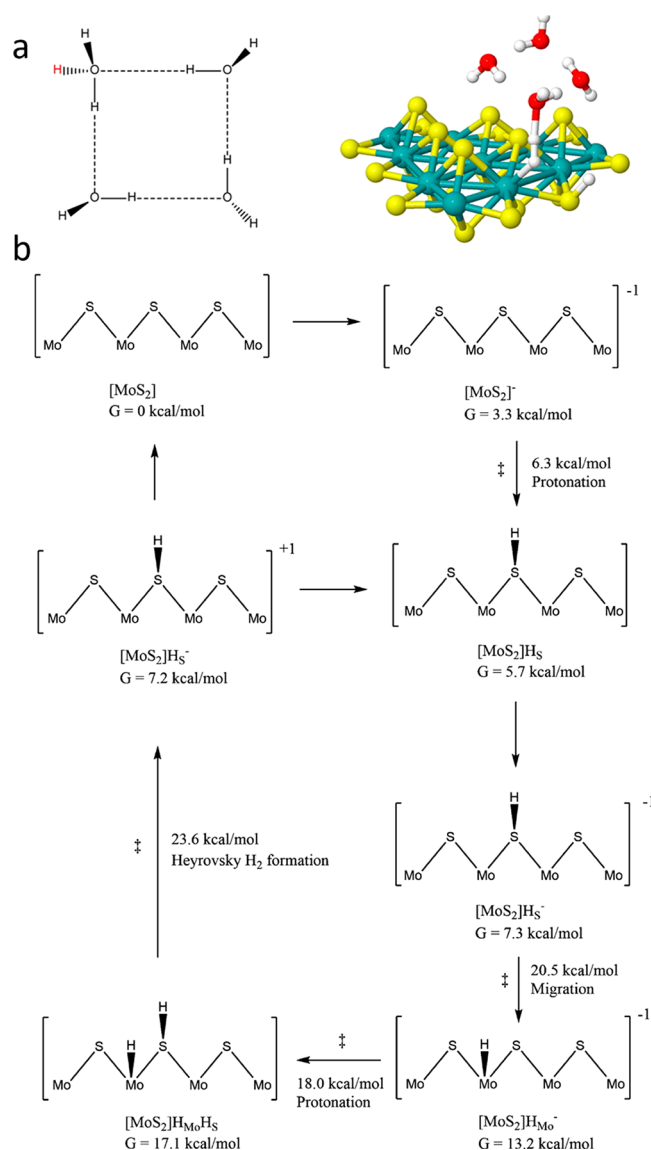


Figure 4. (a) Cluster model for studying HER on MoS₂ edge, which contains four water molecules, 1 proton, and the Poisson–Boltzmann continuum solvation. (b) Overall reaction mechanism for HER on the Mo-edge cluster. Adapted with permission from ref 45. Copyright 2015 American Chemical Society.

al.,⁴⁵ they used a periodic model and more water molecules around the edge. The barrier is determined by nudged elastic band method and its potential dependence is obtained by the charge-extrapolation method. In contrast to Goddard's work⁴⁵ that suggests the H migrates from S to Mo and then reacts with proton to form H₂, they found that the Mo site is only involved in the transition state. The rate limiting step is still the Heyrovsky step: the adsorbed H at the S site reacts with a proton from waters to form H₂, with a transition state where H is bonded to Mo (see Figure 5). The barrier for this step is found to be 0.62 eV under 0 V vs SHE. The authors further calculated the barrier for MoSe₂ (0.74 eV), WS₂ (0.6 eV), and WSe₂ (0.84 eV) edges. In comparison to transition metal electrocatalysts, they found that the activation barrier of the Heyrovsky reaction on 2D-TMDs scales with the hydrogen adsorption energy exactly as for transition metals except that all activation energies are displaced upward by 0.4 eV. This higher Heyrovsky activation barrier is responsible for the substantially lower activity of 2D-

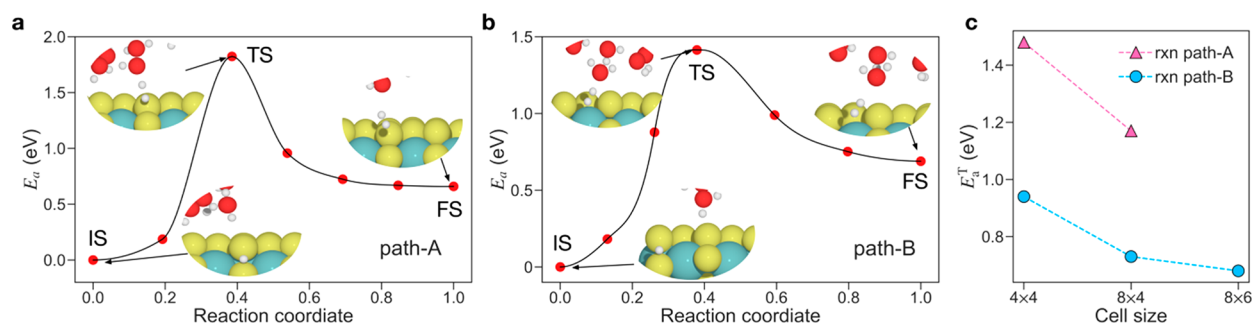


Figure 5. (a,b) Two minimum energy pathways of the Heyrovsky reaction on a 4×4 unit cell of MoS_2 . Insets show the initial state (IS), transition state (TS), and final state (FS) structures. (c) Charge-extrapolated Heyrovsky barriers as a function of the cell size under 0 V vs SHE. The barriers for cell size convergence were all calculated with the 0.5 ML hydrogen coverage for consistency. Note that the barriers in a and b are converted to c to account for the constant-potential effect. Adapted with permission from ref 47. Copyright 2022 American Chemical Society.

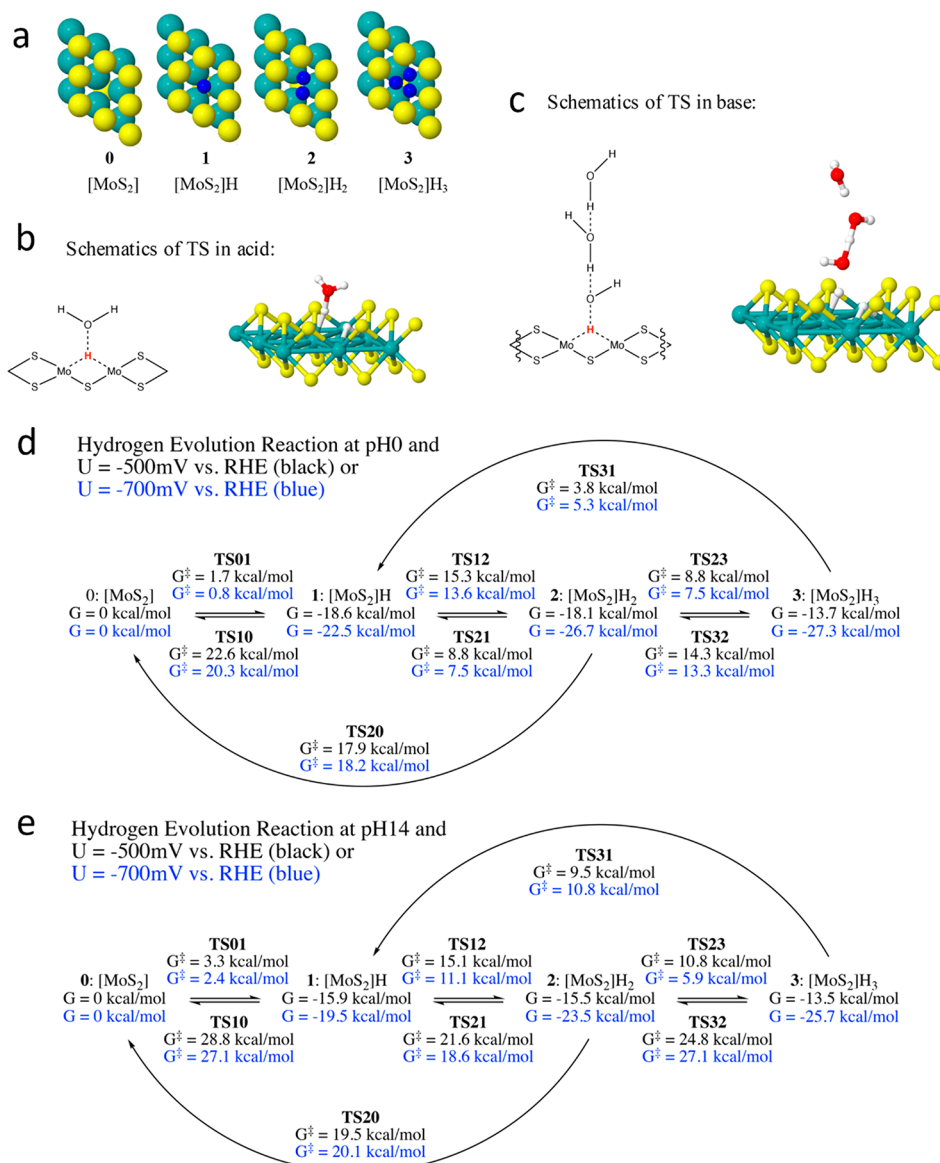


Figure 6. HER on S vacancy of MoS_2 . (a) Four possible states for hydrogen adsorption at the S vacancy site with different number of H. (b,c) Transition states as the system evolves from $[\text{MoS}_2]\text{H}$ to $[\text{MoS}_2]\text{H}_2$ in acidic conditions and in basic conditions, respectively. (d,e) Free energies for all the reaction intermediates and transition states involved in HER. Adapted with permission from ref 31. Copyright 2018 American Chemical Society.

TMDs. Using Bader charge analysis, they further showed that this higher activation barrier stems from the more positively

charged adsorbed hydrogen on the chalcogenides interacting repulsively with the incoming proton. This mechanism is

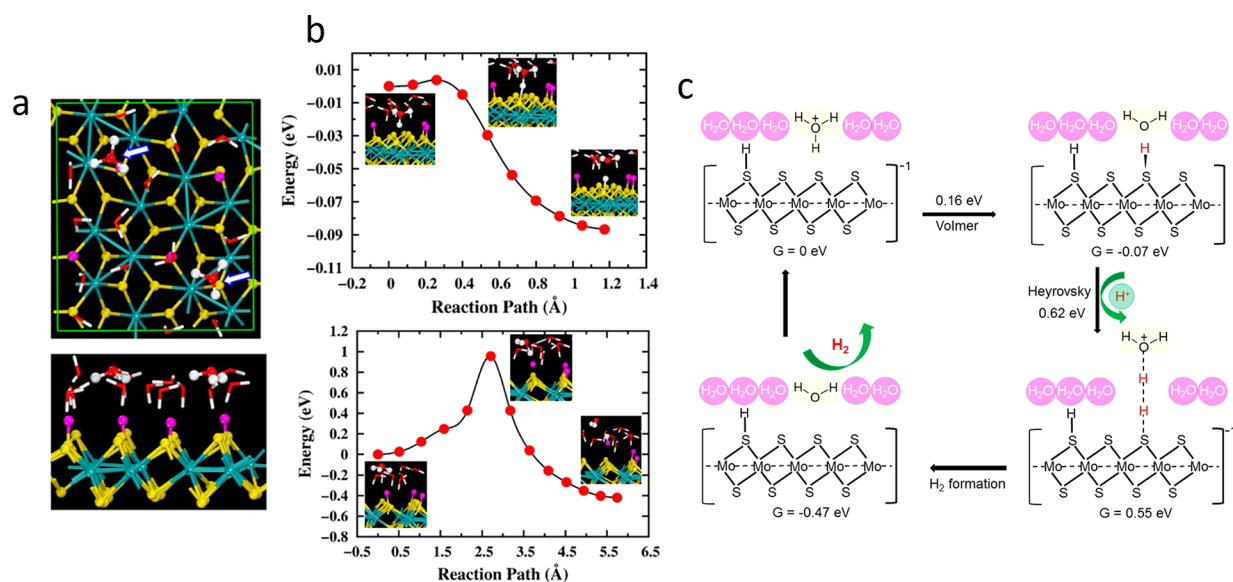


Figure 7. Mechanism of HER on T-MoS₂. (a) Solvated 1T-MoS₂ system with $6 \times 4\sqrt{3}$ supercell, at 25% surface H coverage with $1/8$ proton concentration in the water layer. (b) Minimum-energy pathways of Volmer and Heyrovsky reactions, respectively. Note these energies are without the correction for constant-potential effect. (c) Schematic of HER mechanism. Relative free energy (G) values and activation energies (for the Volmer and Heyrovsky steps) are also shown. Adapted with permission from ref 58. Copyright 2017 American Chemical Society.

consistent with ref 33, that suggested the charge of the site plays an important role in determining the electrochemical barrier.

In addition to the edges, the S vacancies and grain boundaries also possess HER activity. Nørskov and Zheng et al.⁴⁸ used argon plasma to create S vacancies and strain in MoS₂, which activates the basal plane. DFT calculations show that the S vacancies create electronic gap states that allow hydrogen to bind directly to exposed Mo atoms. The formation free energy of *H (ΔG_{H}) can be further manipulated by the strain, which tunes the catalytic activity. Proper combinations of S vacancy and strain give the ΔG_{H} close to 0 eV, yielding high HER activity. The role of strain is confirmed in the work by Bard and Zheng et al.,⁴⁹ who used scanning electrochemical microscopy to determine the HER kinetic data for both unstrained S vacancies and strained S vacancies on the basal plane of MoS₂ monolayers. They found that the strained S vacancy has an electron-transfer rate 4 times higher than that of the unstrained S vacancy. Cao et al.⁵⁰ measured the turnover frequency (TOF) of the edge sites, sulfur vacancies, and grain boundaries to be 7.5, 3.2, and 0.1 s^{-1} , respectively, and typical Tafel slopes to be 65–75, 65–85, and 120–160 mV/dec. Unlike the linear dependence on the length of the edge sites and grain boundaries, the catalytic activity shows a maximum with the density of sulfur vacancies in the range of 7–10%. They also showed that the catalytic activity of the sulfur vacancies is also related to the crystalline quality close to the vacancies, as higher crystalline quality nearby may enable higher catalytic activity at the vacancies. Other works report that engineering grain boundaries can improve HER performance,^{51,52} as DFT calculations based on CHEM show that some structures of grain boundaries can have ΔG_{H} close to zero.^{51,52} Wang et al.⁵³ studied a variety of point defects and grain boundaries in MoS₂ using DFT-CHEM. They found that six types of defects (i.e., V_{S} , V_{MoS_3} , MoS₂ point defects; 4|8a, S bridge, and Mo–Mo bond grain boundaries) can activate the otherwise-inert basal plane of MoS₂. Particularly, the V_{S} and MoS₂ point defects and S bridge and 4|8a grain boundaries exhibit high activity in both Heyrovsky and Tafel steps. They

explained the activity differences across different defects using a modified band-center model.

Goddard III et al.³¹ studied the kinetics of HER on S vacancy of MoS₂, using GCP-K method (Figure 6). They found that under potentials of -0.5 V and -0.7 V vs RHE, one of the exposed Mo atoms near the S vacancy is adsorbed with H ($[\text{MoS}_2]\text{H}$). Then it will continue to bind two hydrogen atoms sequentially, leading to $[\text{MoS}_2]\text{H}_3$. Then the H₂ molecule is formed via the Tafel mechanism, returning the $[\text{MoS}_2]\text{H}_3$ to the initial state $[\text{MoS}_2]\text{H}$. The rate-limiting step is the Volmer step in which the second hydrogen atom is adsorbed.

Doping can activate the basal plane of MoS₂ as well. Deng and Bao et al.⁵⁴ demonstrated that the catalytic activity of basal plane S atoms of MoS₂ can be triggered by single-atom metal doping in HER. Pt-doped few-layer MoS₂ nanosheets were found to have significantly enhanced HER activity compared with pure MoS₂. Furthermore, they screened 14 additional metals by calculating ΔG_{H} based on DFT CHEM, which predicts Co-doped MoS₂ is also a good HER catalyst. This was further confirmed in their experiment.

Transforming MoS₂ from the semiconducting (H) phase to metallic (T) phase (less stable) also activates the basal plane for HER, thanks to the lowered ΔG_{H} and increased electrical conductivity.^{55–57} Jiang et al.⁵⁸ used DFT to study the mechanism of HER on the basal plane of T-MoS₂ (Figure 7). They first calculated the ΔG_{H} for H at different H coverages using CHEM and found that ΔG_{H} is close to 0 for H coverage of 12.5–25%. Taking the H coverage of 25%, they examined the reaction energy and barrier for the Volmer, Tafel, and Heyrovsky steps of the HER process. The acid solution was modeled with one layer of water containing proton(s). By varying the proton concentration, the electrode potential can be tuned and extracted from work function. The water structure is obtained from AIMD simulations. Figure 7a presents the optimized structure of 1T-MoS₂ ($6 \times 4\sqrt{3}$ supercell) at 25% H coverage under two solvated protons. The calculated electrode potential for this system is -0.22 V vs normal hydrogen electrode. They also considered a larger supercell ($9 \times 4\sqrt{3}$) to extrapolate the

reaction energy/barrier for a fixed electrode potential. The reaction pathway and energies are shown in Figure 7b,c: the Volmer step (where the H is adsorbed on the surface) has a small barrier of 0.16 eV, followed by the Heyrovsky step that has a barrier of 0.62 eV and thus limits the overall reaction rate.

Beyond MoS₂, other semiconducting MX₂ (e.g., WS₂, MoSe₂, WSe₂, MoTe₂) are also active for HER, and the catalytic origins are similar to MoS₂ (i.e., the activity comes from the edges, X vacancies, and/or grain boundaries). Strategies used to improve MoS₂ HER performance have also been applied to these materials. For example, Chhowalla et al.⁵⁹ demonstrated that transforming WS₂ from the semiconducting H phase to metallic T phase activates the basal plane for HER. Lu and Jiao et al.⁶⁰ used mild Ar plasma treatment to introduce Se and Pt vacancies and Pt clusters in PtSe₂ and found a high HER performance.

Some metallic MX₂ are intrinsically basal plane active for HER. Wood⁶¹ and Yakobson et al.⁶² used DFT to unravel electronic factors underlying catalytic activity on MX₂ surfaces (Figure 8). By comparing the electronic structure before and

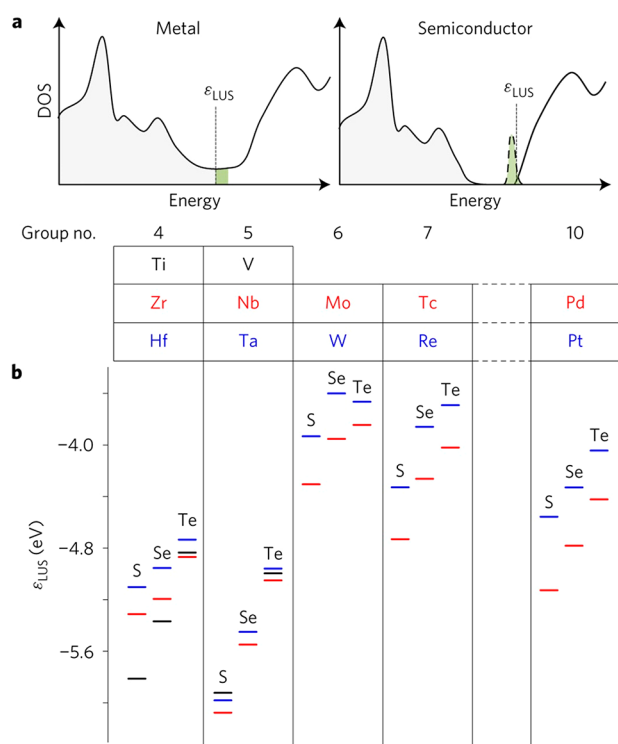


Figure 8. (a) Schematic of the MX₂ DOS, showing initial filled (gray) and empty states, as well as newly filled (green) states following dilute H adsorption. In metals, the Fermi level is slightly elevated, whereas in semiconductors, a shallow state appears near the conduction band edge; in each case, the newly occupied states closely follow the energy of lowest unoccupied state, designated as ϵ_{LUS} . (b) Computed values of the ϵ_{LUS} descriptor for all MX₂ candidates. Row 4/5/6 elements are shown in black/red/blue, with the different chalcogens separated into columns within each group. Adapted with permission from ref 62. Copyright 2017 Nature.

after H adsorption on the basal plane, they found that the energy of lowest unoccupied state (ϵ_{LUS}) is important to the H binding strength. On the basis of this descriptor, they screened various MX₂ in the most stable phase and found that (hexagonal phase) TaS₂ and NbS₂ are highly basal-plane active, which was verified experimentally. Beyond high catalytic activity, these materials are found to exhibit an unusual ability to optimize their

morphology for enhanced charge transfer and accessibility of active sites as the HER proceeds, offering a practical advantage for scalable processing.

Metallic (T' phase) MoTe₂ also shows self-optimizing behavior in HER. McGlynn and Ganin et al.⁶³ showed that the catalytic performance of T'-MoTe₂ is improved dramatically when the electrode is held at cathodic bias. As a result, the overpotential required to maintain a current density of 10 mA cm⁻² decreases from 0.32 V to just 0.178 V. This rapid and reversible activation process is attributed to the adsorption of H onto Te sites on the surface of T'-MoTe₂.

Liu, Lu, and Su et al.⁶⁴ synthesized 2D PtTe₂ (note that PtTe₂ is semiconductor for monolayer while metallic for bilayer or thicker) nanosheets with well-dispersed single atomic Te vacancies by electrochemically exfoliating bulk PtTe₂ crystals, in which large numbers of atomically defined undercoordinated and stabilized Pt sites are exposed. The following heat treatment causes migration of the random vacancies to form ordered clusters. Both electrochemical measurements and DFT calculations show that the heat treatment-induced clustering PtTe₂ can effectively tailor the ΔG_H on the undercoordinated Pt sites. Consequently, the catalyst exhibits much-enhanced HER activity with an exceptionally low overpotential (22 mV at 10 mA cm⁻²) and Tafel slope (29.9 mV per dec⁻¹) and displays negligible activity decay after 20 000 continuous potential cycles and chronopotentiometry test at high current densities (200 mA cm⁻²) for 24 h.

To understand the adsorption of chemical species on the edges of MX₂, Abild-Pedersen et al.⁴⁶ performed DFT calculations (Figure 3b). They considered both the (1010) M-edge and ($\bar{1}010$) S-edge terminations for a wide range of pure and doped MX₂: H-MoS₂, H-WS₂, H-NbS₂, and H-TaS₂, and transition-metal-doped S-edges of MoS₂ with a wide range of metal dopants: Ag, Au, Co, Ni, Os, Pd, Pt, Rh, and Ru (assuming 100% substitution of Mo atoms at the edge). They determined their sulfur coverage under realistic operating conditions and calculated an extensive set of chemisorption energies for several important reactions. They showed that the d-band center, ϵ_d , of the edge-most metal site at 0 ML S coverage is a general electronic descriptor for both structure and adsorption energies. A negative linear correlation between adsorbate-S binding and S-metal binding allows ϵ_d to describe the adsorption of species on both metal and sulfur sites.

It should be noted that although ΔG_{*H} has been widely used to assess HER catalyst performance, it may not explain the experimental observations that are dominated by kinetics. For example, Peterson et al.⁶⁵ found that for Pt(111), the $\Delta G_{H^*} \sim 0$ argument cannot explain why other metal candidates have the similar ΔG_H as Pt(111) but exhibit orders-of-magnitude lower HER activity than Pt. Using the solvated jellium (SJ) method²¹ and CI-NEB method, they studied the kinetic details of the HER steps on Pt(111) and Au(111) and illustrated that the HER activity depends on not only the thermodynamics but also the kinetic paths which distinguish Pt and Au. As another example, Liu et al.⁶⁶ showed that for Ni-N-C catalyst, despite ΔG predicting that HER is thermodynamically more favorable than CO₂R, HER has a higher kinetic barrier than CO₂R, consistent with the high selectivity of CO₂R observed in experiments. These examples suggest that more kinetic studies are needed to better understand and predict HER catalysts.

3.2. X–C

Qiao et al.⁶⁷ reported various heteroatom-doped graphene materials as efficient catalysts for HER. They considered a variety of dopants (B, N, O, S, P, with different configurations, Figure 9a) and used CHEM DFT to calculate the ΔG_{H} on

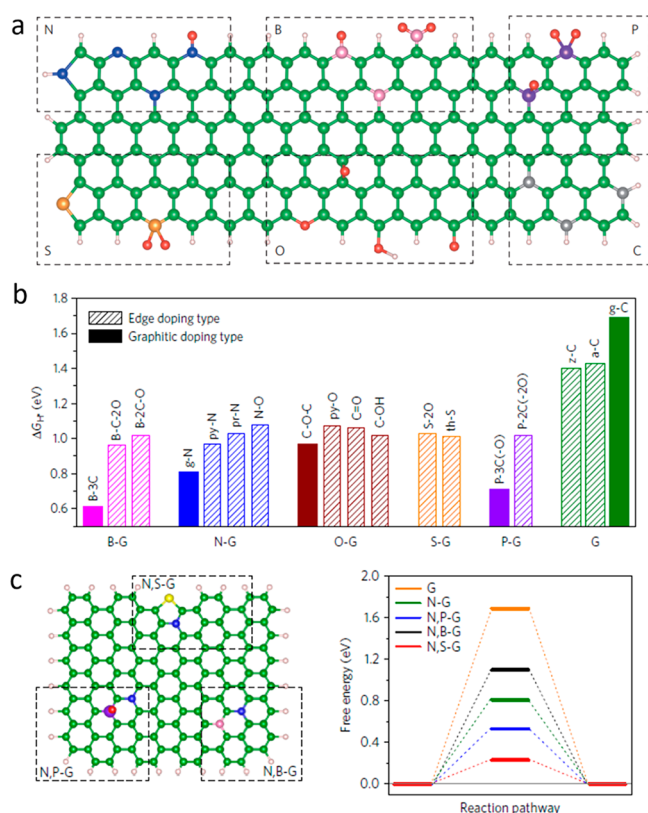


Figure 9. HER on doped graphene. (a) Schematic structures of the dopants including N, B, P, S, O, and C, represented in blue, pink, purple, gold, red, and green/gray, respectively. (b) Corresponding free energies of H adsorption (ΔG_{H}^*). (c) Schematic structures of dual-doped graphene, and the corresponding ΔG_{H}^* . Adapted with permission from ref 67. Copyright 2016 Nature.

different sites. The corresponding ΔG_{H} values are summarized in Figure 9b, with the lowest being 0.61 eV (on B-3C model). The experimentally measured exchange current density per site increases with decreasing ΔG_{H} . They also considered the dual-doping case based on g-N with the secondary element to be P, S, or B. As is shown in Figure 9c, the most active dual-doped graphene model is N₂S–C, represented by a low ΔG_{H} value of 0.23 eV, which is significantly less than that for N–C (0.81 eV). Likewise, N₂P–C exhibited a low ΔG_{H} (0.53 eV); while conversely, N₂B–C exhibited a large ΔG_{H} (1.10 eV). The active sites are usually the carbons next to the dopants. They further synthesized various dual-doped graphene samples and compared the resulting HER activities with single-doped ones. Indeed, experiments found that N₂S–C and N₂P–C exhibit a lower overpotential, while N₂B–C has a higher one than that for the N–C, consistent with the predictions by ΔG_{H} . The ΔG_{H} is found to be correlated with the highest peak of the density of electronic states projected on the active center. A higher peak position gives a lower occupancy of the antibonding states and thus to a stronger binding with H.

3.3. M–X–C

A variety of single metal atom (e.g., Pt,⁶⁸ Co,⁶⁹ Mo,⁷⁰ W⁷¹) embedded in N doped graphene or nondoped C (e.g., Ni^{72,73}) has been reported to be active for HER. Cheng, Cao, and Cheng Zeng et al.⁷⁴ used DFT to study the binding strength of H (and other species relevant to the ORR and OER) on single metal atom embedded in N doped or nondoped graphene and extracted a universal and simple descriptor that correlates the binding energies (Figure 10). The descriptor is defined as

$$\varphi = \theta_{\text{d}} \times [E_{\text{M}} + \alpha \times (n_{\text{N}} \times E_{\text{N}} + n_{\text{C}} \times E_{\text{C}})] / E_{\text{O}/\text{H}}$$

where θ_{d} is the number of valence electrons in the d orbital of the metal atom, E_{N} and E_{C} represent the electronegativity of nitrogen and carbon elements, n_{N} and n_{C} represent the number of nearest-neighbor N and C atoms, and α is the correction coefficient which is set to 5/4 for M-pyrrole-N₄ while 1 for the other sites (to account for the difference in the number of C and N atoms in the M-containing ring). The increase of φ linearly increases ΔG_{OH} (i.e., decreases the binding strength; Figure 10b), which can be explained by the d-band center theory: a higher φ suggests that the M would possess more valence electrons, downshifting the d-band center (relative to the Fermi level) and making the antibonding states more filled, which weaken the binding. The increase of φ also linearly increases ΔG_{H} , when $\varphi > 27$, while for $\varphi < 27$, an inverse trend is observed (Figure 10c), which is explained by the upshift of the bonding orbitals due to the upshift of the d orbitals that weakens the adsorption. On the basis of the CHEM-DFT calculations of the overpotentials, the authors further suggest good catalysts such as Fe-pyridine/pyrrole-N₄ for the ORR, Co-pyrrole-N₄ for the OER, and Mn-pyrrole-N₄ for the HER (Figure 10b,c).

4. OXYGEN EVOLUTION REACTION (OER)

OER usually refers to the electrochemical generation of O₂ from water: 2H₂O → 4e[−] + 4H⁺ + O₂. It is the anodic reaction in (photo)electrochemical water splitting and is much slower than the cathodic HER. The OER typically proceeds through: H₂O → *OH → *O → *OOH → *O₂ → O₂.

Shakir, Duan, and Huang et al.⁷⁵ reported a general approach to a series of M–N₄ catalysts, identified by systematic X-ray absorption fine structure analyses, direct transmission electron microscopy imaging, and first-principles simulations. They found that for OER, the activity follows the trend: Ni > Co > Fe. DFT calculations based on CHEM were conducted to understand the atomistic mechanism. It is found that the C atoms coordinated to N can participate in the OER process, depending on the M. For Fe and Co, all intermediates bind more strongly to the M site than the C site, therefore the reaction proceeds through the single-site mechanism (Figure 11a). In contrast, for Ni, O* and OH* prefer to reside at the C site, while the OOH* is favorably adsorbed on the M atom (dual-site mechanism, Figure 11b). As shown in Figure 11b, the Fe–N₄ has the strongest binding to all the intermediates compared with other Ms, and the potential-limiting step is the oxidation of *O → *OOH with a thermodynamic barrier of 0.97 eV. For Co–N₄, the potential-limiting step is *OH → *O with a thermodynamic barrier of 0.52 eV. The Ni–N₄ with dual-site mechanism shows the smallest limiting barrier of 0.42 eV, and the potential limiting step is *O → *OOH. For comparison, the authors also calculated the thermodynamic free energy diagram of Ni–N₄ with the single-site mechanism, which gives a significantly larger limiting barrier of 1.24 eV, suggesting that

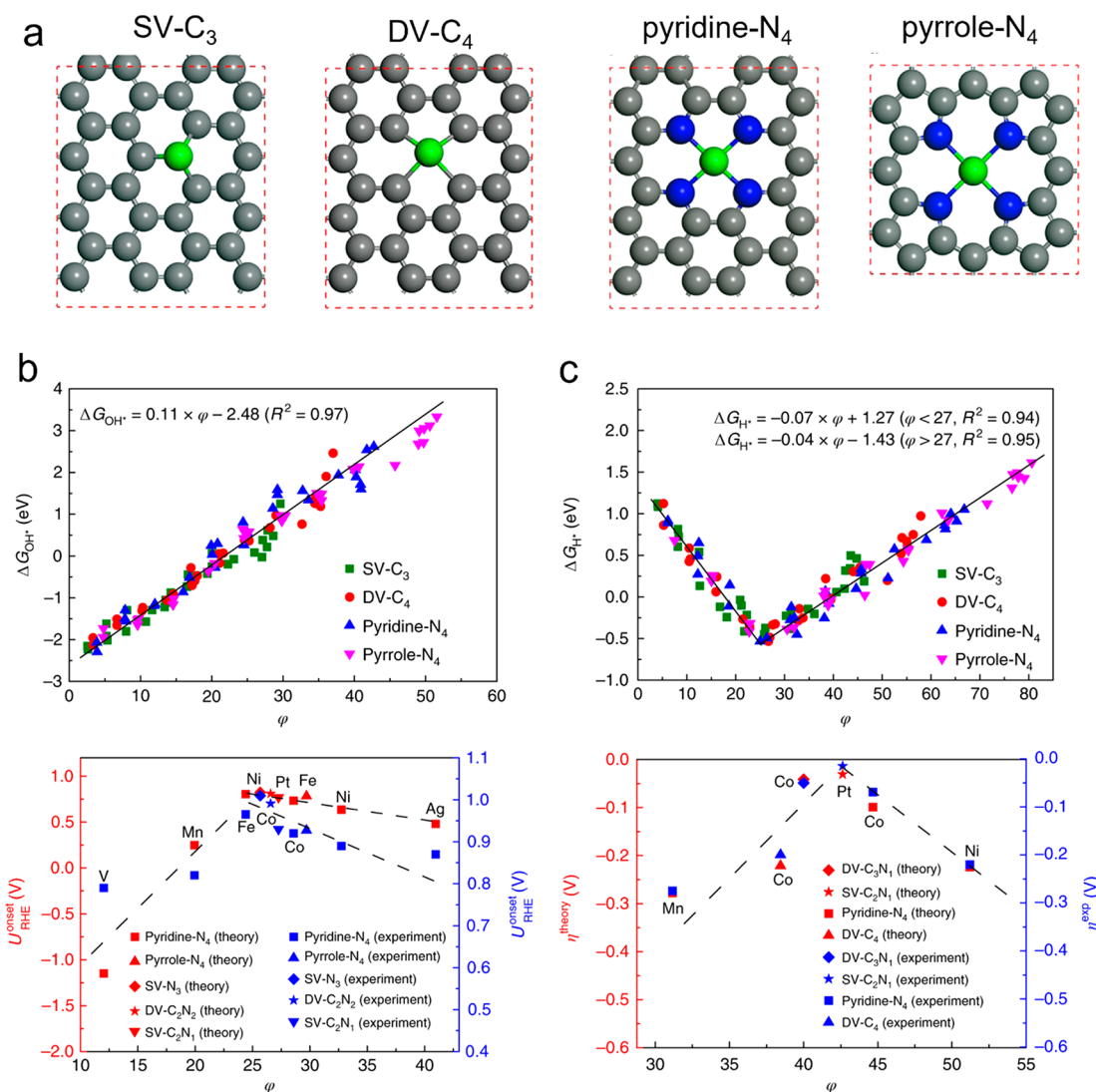


Figure 10. (a) Models of M-C and M-N-C. The unit cells are marked in red. (b) (top) Adsorption free energy of OH; (bottom) theoretical and corresponding experimental onset potentials for ORR. (c) (top) Adsorption free energy of H; (bottom) theoretical and corresponding experimental overpotentials for HER. The x -axes in (b) and (c) are the descriptor ϕ . Adapted with permission from ref 74. Copyright 2018 Nature.

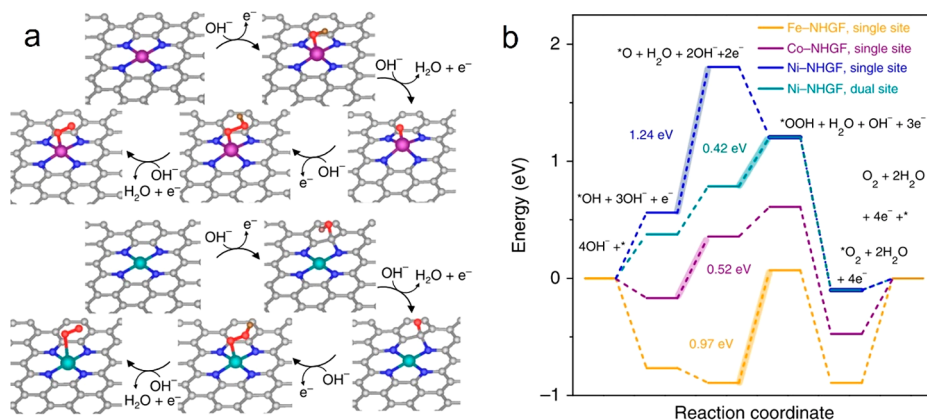


Figure 11. Proposed reaction scheme of OER through the single-site (a) and dual-site (b) mechanisms. Adapted with permission from ref 75. Copyright 2018 Nature.

this mechanism is impossible. Considering that the O₂ adsorption is strong on Fe and Co, they also considered the O₂ adsorption on the other side of the M-N-C and recalculated the free energy diagram. The backside O₂

adsorption increases the barrier for Co, while this does not change that for Fe. The first-principles calculations were also performed to simulate the EXAFS and XANES spectra to aid the structure identification.

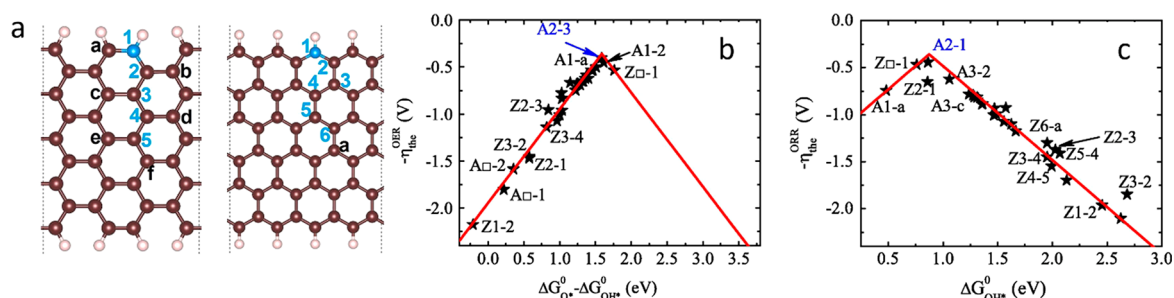


Figure 12. (a) N-doped armchair (A) and zigzag (Z) graphene nanoribbon structures. Numbers denote substitutional sites and reaction sites. Symbols a–f denote reaction sites apart from those denoted by numbers. For example, A2–3 means the N substitutes site 2 but the adsorption occurs at site 3. □ denotes nondoped graphene. (b,c) Volcano plots for OER and ORR on different sites, respectively. Adapted with permission from ref 79. Copyright 2014 Elsevier.

Some other forms of Ni single atom catalyst also exhibit high OER activity. For example, Yao et al.⁷³ showed that single Ni atoms trapped in to graphene defects (Ni–C) can catalyze OER or HER, depending on the site structure. The derived catalyst exhibits good activity, with an overpotential of 0.07 V at 10 mA/cm² for HER and of 0.27 V at 10 mA/cm² for OER. DFT calculations based on CHEM for three different structures suggest that the single Ni atom adsorbed on top of the Stone–Wales defect (D5775) is best for HER, while that embedded in divacancy is the best for OER. Wu and Jiang et al.⁷⁶ reported single Ni atom bonded with O embedded in graphene as an efficient OER catalyst with a low overpotential of 0.224 V. The authors proposed the structure to be Ni–O₄ with OH adsorption on the back side (due to its strong binding). The DFT calculations based on CHEM show that the overpotential is 0.48 V, and the potential limiting step is *OH → *O.

N doped graphene is also an efficient OER catalyst.⁷⁷ Nakanishi et al.⁷⁸ reported that in alkaline media, the N doped graphene generates a current density of 10 mA cm⁻² at the overpotential of 0.38 V, which are comparable to those of iridium and cobalt oxide catalysts. They attributed the high activity to the pyridinic-nitrogen- or/and graphitic-nitrogen-related active sites. Xia et al.⁷⁹ performed CHEM DFT calculations and found that the A2–3 site (the basal-plane C atom bonded to the graphitic N near the armchair edge, Figure 12b) has the lowest OER overpotential of 0.4 V, with the rate-limiting step of *O → *OOH. Dai and Liu et al.⁸⁰ reported that N-doped graphene nanoribbon networks exhibit superb bifunctional electrocatalytic activities for both ORR and OER, with an excellent stability in alkaline electrolytes. It was experimentally demonstrated that the electron-donating quaternary (graphitic) N sites were responsible for ORR, whereas the electron-withdrawing pyridinic N served as active sites for OER.

Layered double hydroxides (LDHs) have been widely studied as catalysts for OER. Among them, NiFe- and CoFe-based LDHs are the most active,⁸¹ and they are also the common active phases of other highly active OER catalysts.⁸¹ LDHs can be exfoliated to atomically thin (2D) layers,⁸² with improved stability (especially at industrial operating conditions such as elevated operating temperatures (e.g., at 80 °C) and large current densities (e.g., at 500 mA cm⁻²))⁸³ and higher activity.^{82,83} Similar to MoS₂, LDHs typically have their active sites located at the edges (instead of basal planes). There have been many studies on the catalytic mechanism of bulk LDHs, while the studies on 2D LDHs are limited. For example, Liu and Guo et al.⁸⁴ synthesized monolayer NiCo hydroxides and found that during OER, the valence states of Ni and Co oscillate. They

attributed such observation to the sequential dehydrogenation and deoxygenation steps. They also showed that Co doping can tune the electronic structure by the Jahn–Teller effect, which reduces the dehydrogenation/deoxygenation potential and thus the OER overpotential. The readers may learn useful insights that may be applicable to the 2D LDHs from the literature studying the bulk LDHs for OER. Of special note is that the LDHs can undergo phase transformation during OER,^{81,85} and the Fe doping is essential to the high activity.⁸⁶

It is worth mentioning that some materials can catalyze multiple reactions. For example, on the basis of DFT-CHEM calculations, Zeng and Wang et al.⁸⁷ found that single nickel atom supported on β12 boron monolayer can catalyze both OER and HER, with low thermodynamic overpotentials of 0.40 and 0.06 V, respectively, making it a good bifunctional catalyst for overall water splitting. Qiao et al.⁸⁸ synthesized a cobalt–C₃N₄ catalyst with activity comparable to that of precious metal benchmarks for the ORR and OER in alkaline media. This high activity is attributed to the Co–N₂ coordination.

5. OXYGEN REDUCTION REACTION (ORR)

ORR converts O₂ to H₂O using 4 electrons (4e) for each O₂, or to H₂O₂ using 2 electrons (2e) for each O₂. The corresponding overall reactions are O₂ + 4H⁺ + 4e⁻ → 2H₂O (in acid condition), O₂ + 2H₂O + 4e⁻ → 4OH⁻ (in alkaline condition), for the 4e reaction, and O₂ + 2H⁺ + 2e⁻ → H₂O₂ (in acid condition), O₂ + 2H₂O + 2e⁻ → H₂O₂ + 2OH⁻ (in alkaline condition), for the 2e reaction. The 4e reaction is used in the fuel cell to convert fuels to electricity. The 2e reaction provides a green and decentralized way to produce H₂O₂, an important chemical that is widely used as bleach, disinfectant, and precursor for other chemicals.

5.1. 4e Reaction

A commonly proposed pathway of 4e ORR is through the following transformation of the intermediates: *O₂ → *OOH → *O → *OH → *O, although some other pathways have been proposed as discussed later.

5.1.1. X-C. Out of all forms of X–C for ORR, N doped graphene is the most well-known catalyst. Therefore, we focus on it in this review. Xia et al.⁷⁹ used CHEM to calculate the thermodynamic free energy diagram of the ORR on different sites, as shown in Figure 12. They found that the C atom at the armchair edge near the graphitic N is the most active site, with ORR overpotential of 0.445 V. The rate-limiting step on this site is the formation of *OOH. Note that the adsorption energy/barrier of O₂ is not considered.

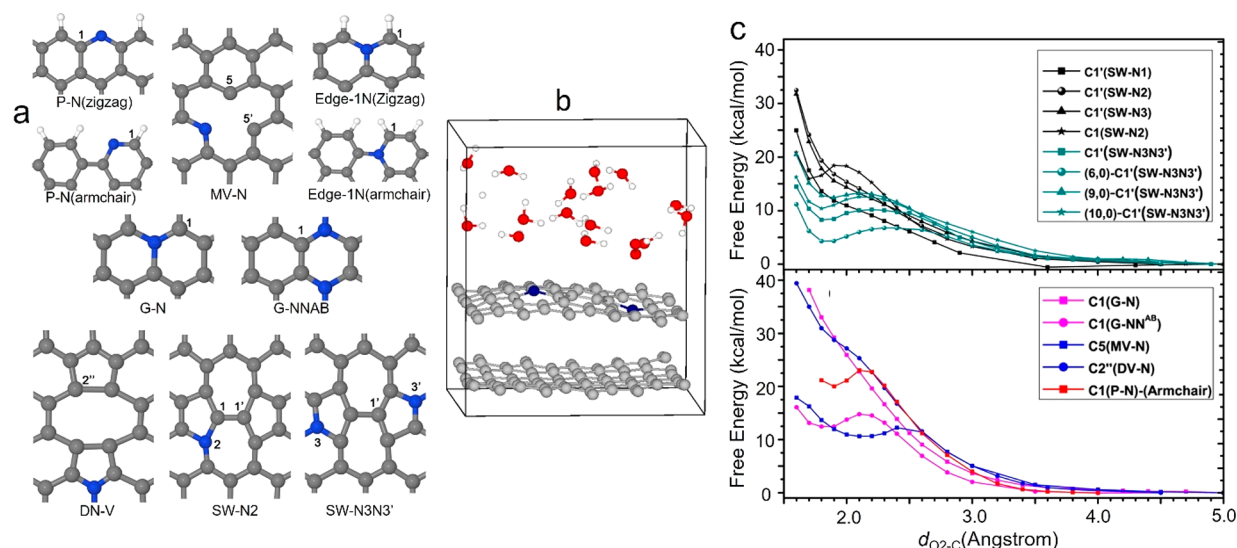


Figure 13. (a) Local atomic structures around N in N-doped graphene. The sites where O₂ is approaching in the simulation are labeled by numbers. Gray, blue, and white balls denote carbon, nitrogen, and hydrogen atoms, respectively. (b) Supercell for the simulation of O₂ molecule adsorption. (c) Free energy profiles for O₂ adsorption for given carbon sites in N-doped graphene and carbon nanotubes. (top) Graphitic N at Stone–Wales defects; (bottom) graphitic N (in perfect graphene and at divacancy) and pyridinic N (at monovacancy and along armchair edge). Adapted with permission from ref 89. Copyright 2014 American Chemical Society.

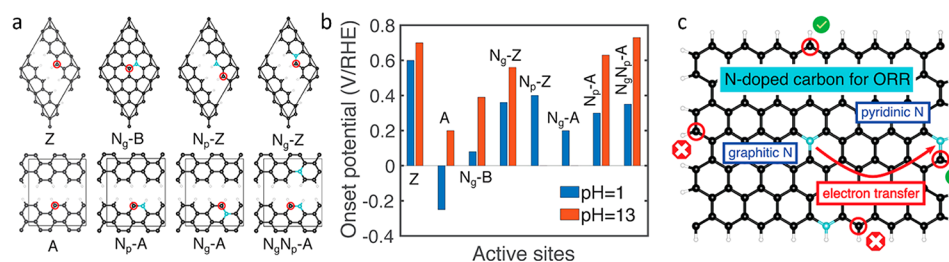


Figure 14. (a) Atomic structures of different active sites. C, black; N, cyan; H, white. The binding sites of ORR intermediates are marked with red circles. (b) Predicted onset potentials for various active sites at pH = 1 and pH = 13. (c) Schematic of the roles of different sites. Adapted with permission from ref 90. Copyright 2020 American Chemical Society.

Chai et al.⁸⁹ considered the adsorption of O₂ onto different sites (Figure 13a). The simulation boxes are shown in Figure 13b. They performed distance-constrained Car–Parrinello molecular dynamics simulations to calculate the free energy profiles of the O₂ adsorption, with GGA–HCTH exchange–correlation functional (which is better than the conventional PBE functional for describing the O₂ molecule) and only the Γ point to sample the Brillouin zone. The O₂ changes from spin triplet to singlet during the adsorption. The free energy profiles for the O₂ adsorption to various sites are shown in Figure 13c, from which the adsorption and desorption barriers can be extracted. It shows that many sites are not able to bind O₂ (meta)stably. Also, for all the sites studied in this paper, the O₂ adsorption barriers are much higher than desorption barriers, which implies that the O₂ will be quickly desorbed if its transformation to *OOH is not fast enough. Nevertheless, the authors further studied the sites for ORR with (meta)stable O₂ adsorption and with the adsorption barriers ≤ 0.80 eV, which are C1(edge-1-N)-(zigzag), C5(MV-N), C1-(NNAB), C1(SW-N2), and C1'(SW-N3N3'). Using the CHEM, they found that the C1'(SW-N3N3') site (a particular structure of a nitrogen pair doped Stone–Wales defect) is a good ORR site.

The papers shown above do not consider the constant potential effect. Henkelman et al.⁹⁰ used constant potential method to calculate the thermodynamic free energy diagram of

ORR on different sites (Figure 14) of graphite, which consist of five graphene layers. They found that the zigzag edge of nondoped graphite exhibits high ORR activities in both acid and base, with the thermodynamical onset potential of 0.6 V vs RHE for pH = 1 and 0.7 V for pH = 13. The rate-limiting step, however, is different: in acidic media, it is the reduction of *OH to water, while in base, it is the *OOH formation. Moreover, it is found that the pyridinic nitrogen dopant can effectively activate the C site at the armchair edge. At pH = 13, the onset potential of ORR is 0.63 V vs RHE, which is a 0.4 V shift from the nondoped material. In acidic media, however, the onset potential is as low as 0.3 V vs RHE. The strong pH dependence is explained by the different binding energies of oxygenated species under different potentials vs SHE. They also found that graphitic N donates electrons to pyridinic N at the armchair edge and enhances the activity of the neighboring C (Figure 14c).

Recent studies suggest the (most) active site is the C atom bonded to the pyridinic N at the edge. Kondo and Nakamura et al.⁹¹ characterized the ORR active site by using newly designed graphite (highly oriented pyrolytic graphite, HOPG) model catalysts with well-defined π conjugation and well-controlled doping of N species. A linear relationship is found between the current density and the concentration of pyridinic N, and pyridinic N-dominated HOPG is found to have significantly higher activity than graphitic N-dominated HOPG and N-free

HOPG under acid conditions. Their CO₂ adsorption experiments indicate that pyridinic N creates Lewis basic sites at which O₂ adsorption can be facilitated as the initial step of ORR. Thus, they concluded that carbon atoms next to pyridinic N are the ORR active sites in N-doped carbon materials.

A similar active site structure is suggested by Yang and Zhou et al.⁹² After selective grafting pyridinic N with an acetyl group, the pyridinic N-doped graphene maintained most of its ORR activity, while the same grafting on ortho-C atoms led to complete loss of the ORR activity. Thus, they identified the ortho-C atom of the pyridinic ring to be the active site for ORR in N-doped graphene. To understand the mechanism, they performed DFT calculations with the CHEM. As shown in Figure 15a–g, in acidic medium, the pyridinic N can be

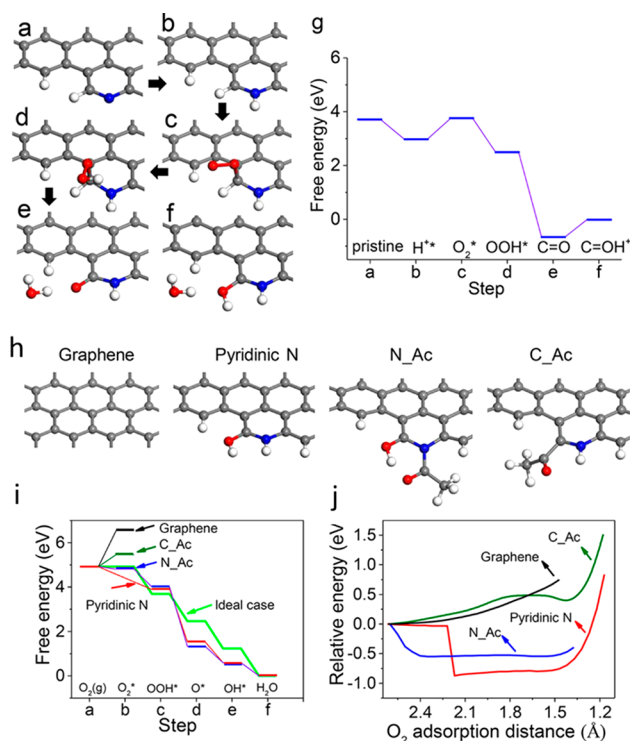


Figure 15. (a–f) Generation of the active C=O structure, from pristine pyridinic N (a), to hydrogenated pyridinic N (b), O₂ chemisorption (c), OOH adsorption (d), C=O formation (e), to hydrogenation of C=O (f). (g) Thermodynamic free energy profile during these processes. (h) Models with different active sites used for evaluating the activity. (i) Corresponding thermodynamic free energy diagram for the ORR on these sites. (j) Energy change when O₂ approaches the sites. Adapted with permission from ref 92. Copyright 2018 American Chemical Society.

protonated, and then O₂ can get chemisorbed on the ortho-C atom. The chemisorbed O₂ gets reduced into OOH and finally into C=O. The C=O could be further protonated to form C–OH at low pH. The protonation of pyridinic N is a critical step; otherwise, O₂ chemisorption cannot occur. Then the authors studied the ORR on this structure (Figure 15h–j). The adsorbed O₂ molecule is found to spontaneously convert into an adsorbed OOH by taking the H from the protonated carbonyl group. The subsequent ORR steps are also feasible, with thermodynamic onset potential of 0.6 V. When the pyridinic N is terminated by the acetyl (Ac) group, the O₂ adsorption is also exothermic and the subsequent ORR steps are also feasible with thermodynamic onset potential of 0.59 V.

However, when the ortho-C is terminated with the Ac group, the O₂ adsorption becomes endothermic, indicating a low ORR activity. These calculation results are consistent with their experiments, suggesting that the edge C atom (terminated with O/OH) bonded to pyridinic N is the active site. Note that the authors also showed that the OOH intermediate cannot be chemically adsorbed on this site (Figure S9-g in the original paper), while it is expected that an active site should bind the OOH intermediate stably.

Dai and Yao et al.⁹³ showed that a pentagon defect at the edge, created by removing pyridinic N atom from an N-doped six-carbon ring in highly oriented pyrolytic graphite (HOPG), has a higher activity than pyridinic N for acidic ORR. DFT calculations based on CHEM show that the thermodynamic onset potential for such pentagon defect at the edge is 0.74 V vs RHE, and the rate-limiting step is $*\text{OH} + \text{e}^- + \text{H}^+ \rightarrow \text{H}_2\text{O}$.

The $*\text{OOH}$ is a critical intermediate during ORR, and it is usually formed after the chemical adsorption of O₂. Considering the O₂ chemisorption is generally difficult on N doped graphene, Kim and Woo et al.⁹⁴ proposed a mechanism for $*\text{OOH}$ formation that does not involve the chemical adsorption of O₂. They showed that the first electron is transferred into O₂ molecules at the outer Helmholtz plane over a long-range. The ionized O₂ will further get one proton, forming an OOH radical that can be strongly adsorbed on N doped graphene. On the basis of this mechanism, the level of the electrode potential dominantly characterizes the ORR activity. Accordingly, with DFT calculations they demonstrated that the electrode potential can be increased by reducing the graphene size and/or including metal impurities, thereby enhancing the ORR activity.

In addition to N, other nonmetal dopants and codopants⁷⁷ also exhibit ORR activity. For instance, S-doped⁹⁵ graphene and P-doped⁹⁶ graphene are known to be active for ORR, while DFT CHEM calculations found B-doped⁹⁷ graphene has a small theoretical over potential of 0.29 and 0.28 V in acid and alkaline conditions, respectively. Qiao and co-workers⁹⁸ systematically studied various dopants for ORR, including B, N, P, O, and S. It is found that all these dopants promote the ORR activity, while the B-doping case, followed by N-doping, has the highest activity thanks to its strong adsorption of $*\text{OOH}$ and $*\text{OH}$.

5.1.2. M–X–C. Fe–N–C is the most well-known M–N–C for ORR, and thus we will focus on it in this review. Using Mössbauer spectroscopy aided with DFT calculations, Jaouen et al.⁹⁹ identified the two types of Fe–N₄ site: the low/intermediate-spin type I and high spin type II, as shown in Figure 16. During ORR, Fe in the type II site switches oxidation state between +3 and +2 in the region 0–1 V due to the ad/desorption of O species, while type I does not, remaining to be +2. They also found that both sites initially contribute to the ORR activity in acidic medium. However, type II is not durable in operating PEMFC, quickly transforming into ferric oxides. In contrast, type I is shown to be more durable, with no measurable decrease of the number of active sites after 50 h operation at 0.5 V. In this paper, the DFT was applied to calculate the quadrupole splitting value¹⁰⁰ of different model structures, which helps to identify the atomic structure of the active sites.

Wang et al.¹⁰¹ employed DFT to study the 4e ORR mechanism on three types of Fe–N₄ sites with different local carbon structures (Figure 16). Using NEB method, they found that direct dissociation of the adsorbed O₂ requires high barrier (1.19, 1.39, and 0.94 eV from type I to III). However, after protonation of the $*\text{OO}$, the formed $*\text{OOH}$ can dissociate to $*\text{O}$ and $*\text{OH}$ with relatively low barrier (0.56, 0.72, and 0.20 eV,

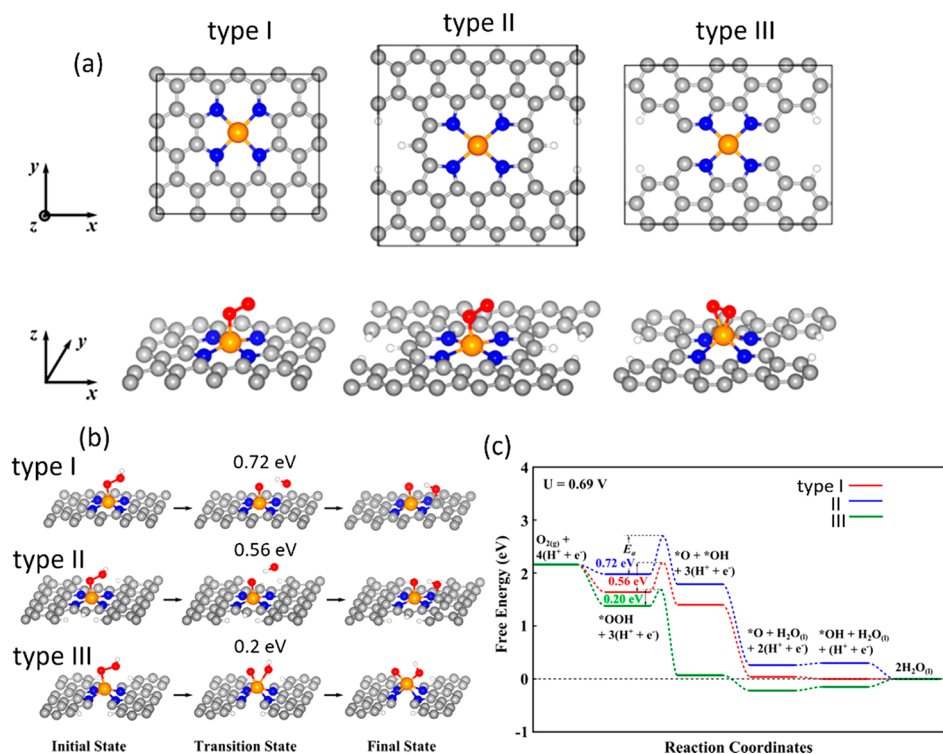


Figure 16. (a) Atomistic structures of possible active sites in Fe–N₄ for ORR, and corresponding configurations of O₂ adsorption. Gray, blue, orange, red, and white balls represent C, N, Fe, O, and H atoms, respectively. (b) *OOH dissociation. (c) Thermodynamic free energy diagram for the ORR through an OOH dissociation pathway. Adapted with permission from ref 101. Copyright 2017 American Chemical Society.

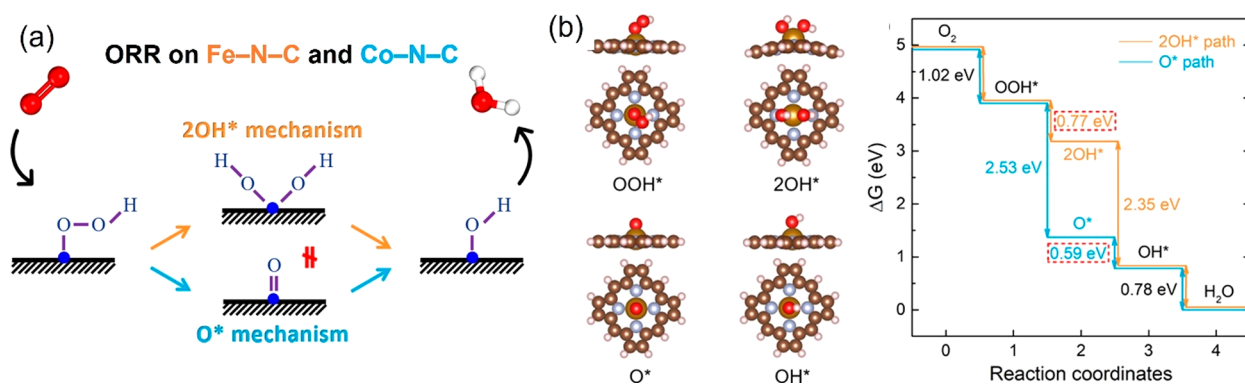


Figure 17. Schematic of the ORR through two mechanisms. (b) Structural models of ORR intermediates and comparison between O* and 2OH* pathways of ORR on Fe/N/C porphyrin. Adapted with permission from ref 102. Copyright 2020 American Chemical Society.

respectively). The lowest barrier of *OOH dissociation for type III site is because the products (*O and *OH) are both adsorbed on the Fe, while for type I and II, the *O is on Fe while the *OH is on C (see Figure 16b). The CHEM calculations further showed that the type III site has a thermodynamic limiting potential of 0.54 V. Therefore, they concluded the type III is the most active site for ORR.

Li et al.¹⁰² proposed a different ORR pathway on M–N–C (M = Fe, Co; Figure 17). Instead of direct dissociation of *OOH to form *O and *OH as proposed in Wang's work,¹⁰¹ the *OOH can dissociate to two *OH adsorbed on the metal site, aided by H. The authors used NEB method to calculate the activation energies of the oxygen species dissociations on Fe-porphyrin molecule. They found that direct *OOH dissociation requires an activation energy of 0.94 eV, thus ruling out this possibility (note the catalyst models and the final structures in Li's¹⁰² and Wang's¹⁰¹ works are different). In contrast, the H-

assisted *OOH dissociation paths have much smaller activation barriers: 0.001 eV for the *OOH + H* → *O + H₂O (*O mechanism); 0.056 eV for *OOH + *H → 2*OH (2*OH mechanism). Note that when calculating the activation energies, the authors assumed that the H is initially adsorbed on the N coordinated to the Fe and is then attached to the O in *OOH. Using CHEM, the authors showed that the conventional O* mechanism significantly underestimates the half-wave potential for ORR of Fe–N₄, due to the small free energy decrease from *O to *OH, while their proposed 2*OH mechanism circumvents this rate-determining step and predicts a higher and reasonable half-wave potential, which agrees better with experimental results. For Co–N₄, however, the conventional *O mechanism is still preferred because of the large formation free energy of the 2*OH.

The above two works do not consider the adsorbate that may exist on the other side of the catalyst and may affect the reaction.

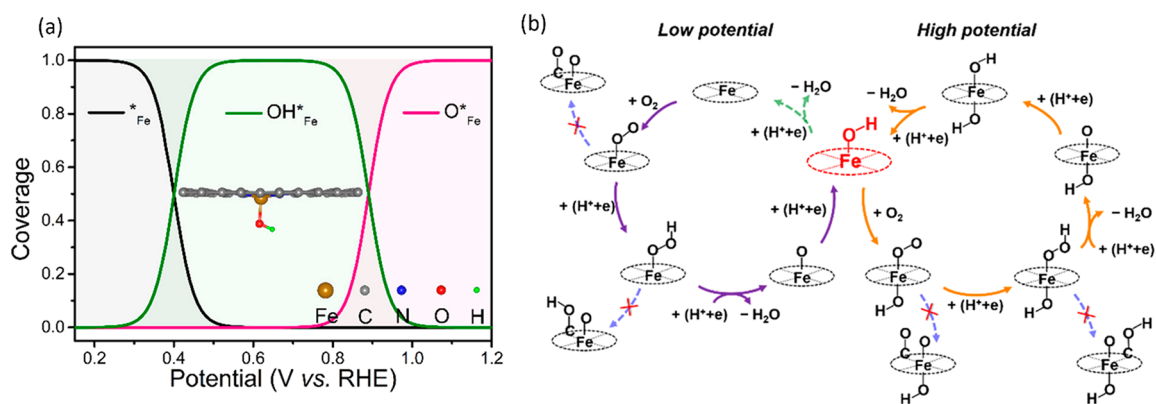


Figure 18. (a) Coverages of the most abundant ORR intermediates on the type I Fe–N₄ site as a function of potential with the inset being the geometry of OH*_{Fe}. (b) Mechanistic scheme for ORR. Adapted with permission from ref 103. Copyright 2019 American Chemical Society.

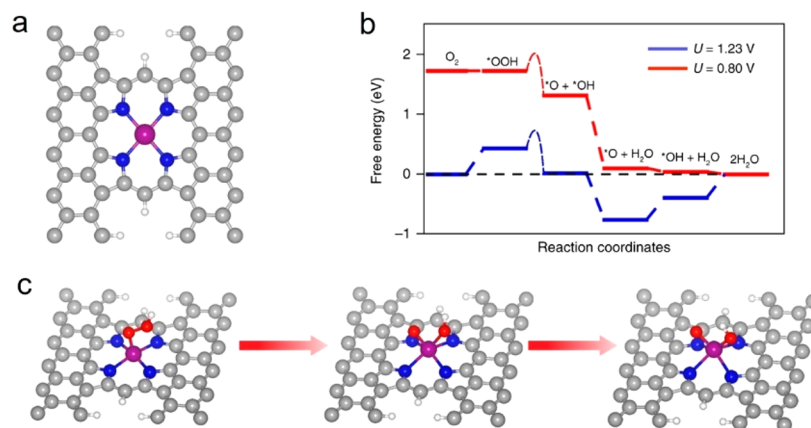


Figure 19. (a) Proposed active site structure of Mn–N₄ catalyst for ORR. (b) Corresponding thermodynamic free energy diagram under electrode potential of $U = 1.23$ V and $U = 0.80$ V. (c) Initial (left), transition (middle), and final (right) states of *OOH dissociation. Gray, blue, purple, red, and white balls represent C, N, Mn, O, and H atoms, respectively. Adapted from ref 108. Copyright 2018 Nature.

Zhou et al.¹⁰³ used DFT and microkinetic modeling to show that the O species (*OH) adsorbed on one side of the site can optimize the adsorption energetics on the other side (Figure 18). The authors considered the type I structure in Figure 16. They found that with decreasing electrode potential (U), the dominant adsorbate changes from *O ($U > 1$ V) to *OH (0.78 V $> U > 0.51$ V), and then is removed ($U < 0.28$ V), as shown in Figure 18. At relatively low potential, due to the OH adsorption on one side, the Fe atom is buckled from the N₄-plane (Figure 18a), consistent with the experimental observation.^{104,105} The authors then studied the ORR (Figure 18b) over the Fe–(OH)N₄ center. The NEB calculations show large barriers for *O₂ and *OOH dissociations, thus the ORR should follow the associate pathway. The interactions between Fe and intermediates become weaker after involving the OH* on the other side. The potential-limiting step is still OH* removal, while the thermodynamic onset potential (obtained from the thermodynamic free energy diagram based on CHEM) increases from 0.40 to 0.76 V, thanks to the weakened OH binding. The simulated ORR polarization curve of the Fe–(OH)N₄ center exhibits an onset potential of ~ 0.95 V and half-wave potential (at the current density of -3 mA cm⁻²) of ~ 0.88 V, much higher than the half-wave potential of the FeN₄ center (~ 0.51 V). The authors further analyzed the coverages of the intermediates on Fe–(OH)N₄. Different from Fe–N₄, OH* is the only abundant intermediate and is removed above 0.92 V. When the additional *OH is formed on Fe–(OH)N₄, the central Fe atom restores to

the N₄-plane (Figure 18b), which is consistent with the experimental observation that the Fe atom is located within the N₄-plane at high potential.^{104,105}

Xiao and Yu et al.¹⁰⁶ studied the interaction between Fe–N₄ sites and the correlation with the ORR performance. They found an increasing activity with decreasing intersite distance down to 0.7 nm. DFT calculations show that as the intersite distance decreases, the Fe magnetic moment decreases and the binding with OH weakens, which are attributed to the increased filling of the d orbitals. Myers, Jaouen, and Jia et al.¹⁰⁷ synthesized the Fe–N–C catalyst with a density (1.92×10^{20} sites per gram) of the active sites, which are fully gas-phase accessible and electrochemically accessible (100% site utilization), delivering a high ORR activity of 33 mA cm⁻² at 0.90 V (iR -corrected) in a H₂–O₂ PEMFC at 1.0 bar and 80 °C. The catalyst is synthesized by chemical vapor deposition, where the iron chloride vapor is flowed over a Zn–N–C substrate at 750 °C, leading to high-temperature trans-metalation of Zn–N₄ sites into Fe–N₄ sites. Fe Mössbauer spectra collected at 5 K, as well as the XANES and EXAFS, reveal that the type II site is dominant in the catalyst. Interestingly, the type I site is absent. Myers, Xie, Cullen, Litster, and Wu et al.² synthesized Fe–N₄ by depositing N–C species on the catalyst surface via chemical vapor deposition, which demonstrates competitive activity to that of Pt/C catalysts and dramatically enhanced stability and durability under practical operating conditions in PEMFCs. With DFT calculations, they identified a reconstruction of the carbon structure neighboring

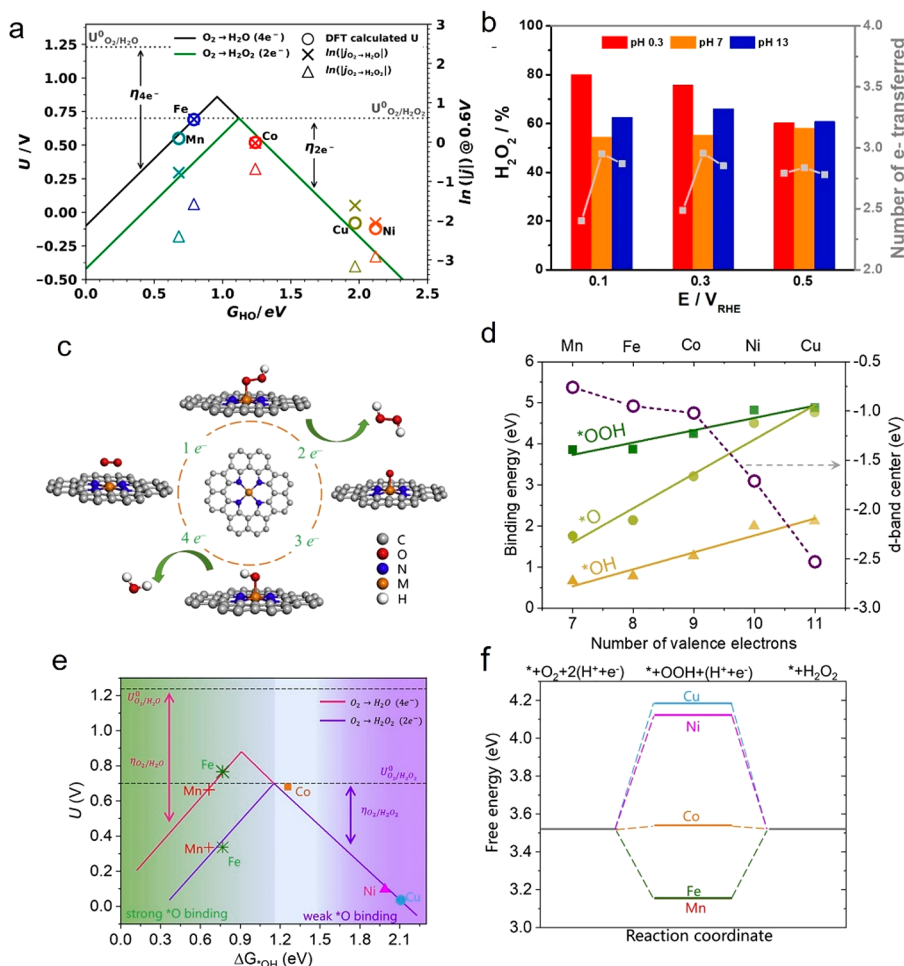


Figure 20. (a) Theoretical thermodynamic onset potentials of 4e and 2e pathways vs formation free energy of *OH, for M-N₄. The experimental current densities (crosses and triangles) are on the right y-axis. The right y-axis is adjusted to overlap the data points of onset potential and experimental current density for 4e pathway on Fe-N₄. (b) H₂O₂ selectivity and the number of electrons transferred at different applied electrode potentials. Adapted with permission from ref 110 Copyright 2019 American Chemical Society. (c) Schematic of ORR along the 2e or 4e pathway. (d) Binding energies of *OOH, *O, and *OH on M-N₄ and the d-band centers (open circle) of M-N₄. (e) Theoretical thermodynamic onset potentials of 4e and 2e pathways vs formation free energy of *OH, for M-N₄. (f) Thermodynamic free energy diagram of 2e ORR on M-N₄ at $U = 0.7$ V versus RHE. Adapted with permission from ref 112. Copyright 2020 Science Direct.

to the Fe-N₄ site being responsible for the enhanced resistance to demetalation and carbon oxidation.

Although the Fe-N-C catalysts have promising performance, they often suffer from insufficient durability, which limits their practical applications in PEMFCs. One of the main reasons for the instability is the occurrence of the Fenton reactions ($Fe^{2+} + H_2O_2$), where dissolved Fe ions combine with H₂O₂, a byproduct of the two-electron ORR. As a result, a significant amount of active oxygen-containing hydroxyl and hydroperoxyl radicals are generated that can degrade the catalyst, the ionomer within the electrode, and the polymer membrane in PEMFCs. Inspired by the weak reactivity between Mn and H₂O₂, Wang and Wu et al.¹⁰⁸ reported an efficient Mn-N₄ catalyst. The Mn-N-C catalyst showed significantly enhanced stability in acidic media. DFT calculations based on CHEM suggest that the type II site (see Figure 19a) is the most active site. Its free-energy evolution for the ORR and the transition state for an OOH dissociation on the active site are shown in Figure 19b. Next, the OOH will dissociate into O and OH (both on Mn, with a barrier of 0.49 eV). Lastly, both O and OH will be protonated to form the final product H₂O (Figure 19b,c). The thermodynamic free

energy diagram (Figure 19b) indicates an onset potential of 0.80 V and the rate limiting step is *OH → H₂O.

Compared with Fe, Co is also less reactive to H₂O₂, so from this consideration, the Co-N-C catalyst may be more stable than Fe-N-C. However, many Co-N-C catalysts suffer from substantial generation of H₂O₂ during the ORR in acidic media, which makes them even less stable in acids than Fe-N-C. Recently, Wu, Ramani, and Shao et al.¹⁰⁹ synthesized a Co-N-C catalyst, with an ORR activity higher than that of noniron platinum-group-metal-free catalysts reported in the literature. In addition, the Co-N-C catalyst has an enhanced durability compared with a similarly synthesized Fe-N-C. Notably, the H₂O₂ yield is minimized (<2%). The enhanced durability of Co-N-C relative to Fe-N-C is attributed to the lower activity of Co ions for Fenton reactions that produce radicals from the H₂O₂, and the significantly enhanced resistance to demetalation of Co-N-C. Type II site with Co-N₄ composition is believed as the active site in this catalyst. This structure may have stronger binding with *OOH intermediate than type I, thereby suppressing the formation of H₂O₂.

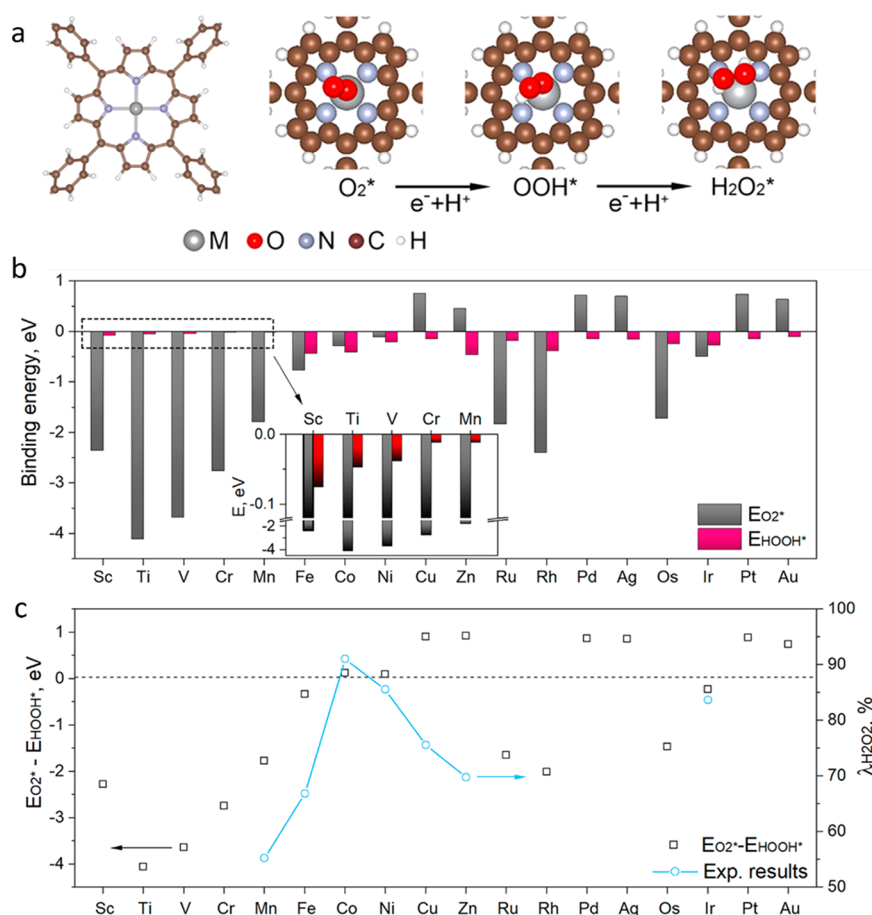


Figure 21. (a) Cluster model of Co-N₄-COF, and (geometries of adsorbed reaction intermediates. (b) Calculated binding energies O₂ and HOOH ($E_{O_2^*}$ and E_{HOOH^*}) on different metal centers in M-N₄-COF). (c) Comparison between $E_{O_2^*} - E_{HOOH^*}$ and experimentally measured H₂O₂ efficiency $\lambda_{H_2O_2}$ for various M-N-COF catalysts. Adapted with permission from ref 113. Copyright 2020 American Chemical Society.

5.2. 2e Reaction

5.2.1. M-X-C. Rossmeis, Jaouen, and Strasser et al.¹¹⁰ studied the electrochemical H₂O₂ synthesis over five M-N-C materials (M = Mn, Fe, Co, Ni, Cu). Co-N-C catalyst has outstanding H₂O₂ productivity with high ORR activity, highest H₂O₂ selectivity, and lowest H₂O₂ reduction activity. The activity and selectivity trends over these materials were further analyzed by DFT. Using the CHEM to study various M-N₄, they calculated the theoretical thermodynamic onset potentials for the 2e and 4e pathways and correlated with the formation energies of *OH (ΔG_{*OH}), as shown in Figure 20a. For the Ni, Cu, and Co that bind weakly with the adsorbate (and thus a high ΔG_{*OH}), the 2e and 4e pathways share the same thermodynamical onset potentials, as the rate limiting step is the *OOH formation. For Fe and Mn that bind strongly with the adsorbate (and thus a low ΔG_{*OH}), the rate-limiting step for 2e pathway is the *OOH → H₂O₂, while the rate-limiting step for 4e pathway is *OH → *. For those catalysts, the 4e pathway always has a higher thermodynamic onset potential than the 2e pathway, which means the 4e pathway is thermodynamically more favorable. Co has the highest onset potential, agreeing with its highest activity observed experimentally. Moreover, compared with Fe and Mn, which have higher thermodynamic onset potentials for 4e pathway than for 2e pathway, Co has the same thermodynamical onset potentials for both pathways, agreeing with its higher selectivity for H₂O₂ than Fe and Mn as observed experimentally. Note that for Cu and Ni, the calculated onset

potential is too low due to the weak binding with the intermediates which would result in virtually no activity. The authors then attributed the observed activity on Cu and Ni to the graphene edge defects and nonmetal nitrogen sites in the N-C substrate. They also find that in acid medium the H₂O₂ selectivity increases as the potential is decreased while a similar trend is not obvious under alkaline or neutral conditions (Figure 20b). The selectivity dependence on potential in acid condition is explained by Liu et al.,¹¹¹ as discussed later.

Huang and Liu et al.¹¹² also demonstrated that the Co-N-C performs excellently for ORR to H₂O₂ (Faraday efficiency >90%) in acid media. Using CHEM, they studied the M-N₄ type I structure (Figure 20c) in a cluster model (MN₄C₄₀H₁₆). Thermodynamic free energy diagram (Figure 20f) shows that Co-N₄ has a nearly zero overpotential, while the activities of Ni and Cu are limited by the step of O₂ → *OOH, and the activities of Fe and Mn are limited by the step of *OOH → H₂O₂. The calculated volcano plot (Figure 20e) is similar to that reported by Rossmeis, Jaouen, and Strasser et al.,¹¹⁰ where the Ni and Cu have too high ΔG_{*OH} while Fe and Mn have too low ΔG_{*OH} , but Co has the optimal value. The authors further explained the trend of binding energies of the intermediates (*OOH, *O, *OH) across different metal elements: as the number of valence electrons increases from Mn to Fe, Co, Ni, and Cu, the d-band center decreases (d orbitals become more occupied), and thus the binding weakens (ORR2e-1d).

Henkelman, Wei, and Chen et al.¹¹³ synthesized covalent organic framework with an identical metal coordination environment as model catalysts to elucidate the intrinsic catalytic activity of various M–N–COF. Using DFT, they found that the difference between the binding energies of O_2^* and HOH^* ($E_{O_2^*} - E_{HOH^*}$) is a good descriptor for experimental performance parameters, including the H_2O_2 efficiency (Figure 21c), the onset potential for ring electrode, the specific current density for H_2O_2 formation, and the specific current density for H_2O formation, obtained at 0.3 V versus RHE. Co and Ni are found to sit on the top of the curves of the catalytic performance parameters, while their $E_{O_2^*} - E_{HOH^*}$ approaches zero. This suggests that the optimal catalyst should have $E_{O_2^*} - E_{HOH^*} \approx 0$ eV. Using this as a descriptor to rapidly screen other M–N₄–COF candidates, as shown in Figure 21c, a new metal, Ir, is predicted to have high H_2O_2 activity as well, which is validated experimentally. We note that this paper shows that the H_2O_2 selectivity is generally higher in alkaline condition than in acid condition, which is different from the findings by Strasser et al.¹¹⁰ This is probably due to the fact that the diffusion of H_2O_2 is more limited in the ordered organic framework and H_2O_2 reduction can be accelerated by proton in the system.

Yoo, Sung, and Hyeon et al.¹¹⁴ showed that epoxy groups can promote the performance of Co–N₄. They performed DFT calculations to evaluate various M–N₄ catalysts, particularly Co–N₄ with different functional groups (Figure 22a). The CHEM calculations show that the formation free energy of *OOH ($\Delta G_{^*OOH}$) is negative under the equilibrium potential for H_2O_2 production (while Strasser et al.¹¹⁰ and Liu et al.¹¹² showed that it is positive, probably due to the use of different models (cluster vs periodic) and DFT functionals). The adsorption of OOH weakens if there are electron-rich species, such as O and OH (Figure 22a), adsorbed near the Co–N₄ moiety. This increases the $\Delta G_{^*OOH}$ to be closer to zero and thus increasing the theoretical thermodynamic onset potential (Figure 22b). However, when electron-poor species, such as H (Figure 22a), are adsorbed near the Co–N₄ moiety, the *OOH adsorption strengthens and the onset potential decreases. The authors explain these effects of the functional groups by the differences in the charge state of the cobalt atom (Figure 22c): the O adsorption near the site makes the Co more positive, while H adsorption makes it more negative. We note that this correlation is a bit counterintuitive, as one would expect a more positively charged Co should bind OOH more strongly (contradicting the weakened binding found by DFT) if their interaction is largely electrostatic. Instead, we suggest that the repulsion by the negatively charged *O may be the main reason for the increase of $\Delta G_{^*OOH}$, and the attraction by the positively charged *H may be the main reason for the decrease of $\Delta G_{^*OOH}$. The authors then synthesized the Co–N₄ moiety incorporated in nitrogen-doped and oxygen-adsorbed graphene by mildly reducing the metal-adsorbed graphene oxide at 500 °C in NH_3/Ar . The catalyst indeed shows high performance for electrochemical H_2O_2 production, with a kinetic current density of ~ 2.8 mA cm^{-2} , a mass activity of ~ 155 A g^{-1} (at 0.65 V vs RHE), and negligible activity loss over 110 h in basic conditions.

Amal and Lu et al.¹¹⁵ also showed that the O adsorbates can promote the performance of Co–N₄. This is also explained by the fact that the epoxy oxygen formed close to M–N₄ significantly weakens the binding strength of HOH^* on Co and thus increases the free energy of HOH^* to be closer to zero. Bader charge analysis reveals that epoxy oxygen, as an electron-withdrawing group, depletes the electrons on Co of Co–N₄

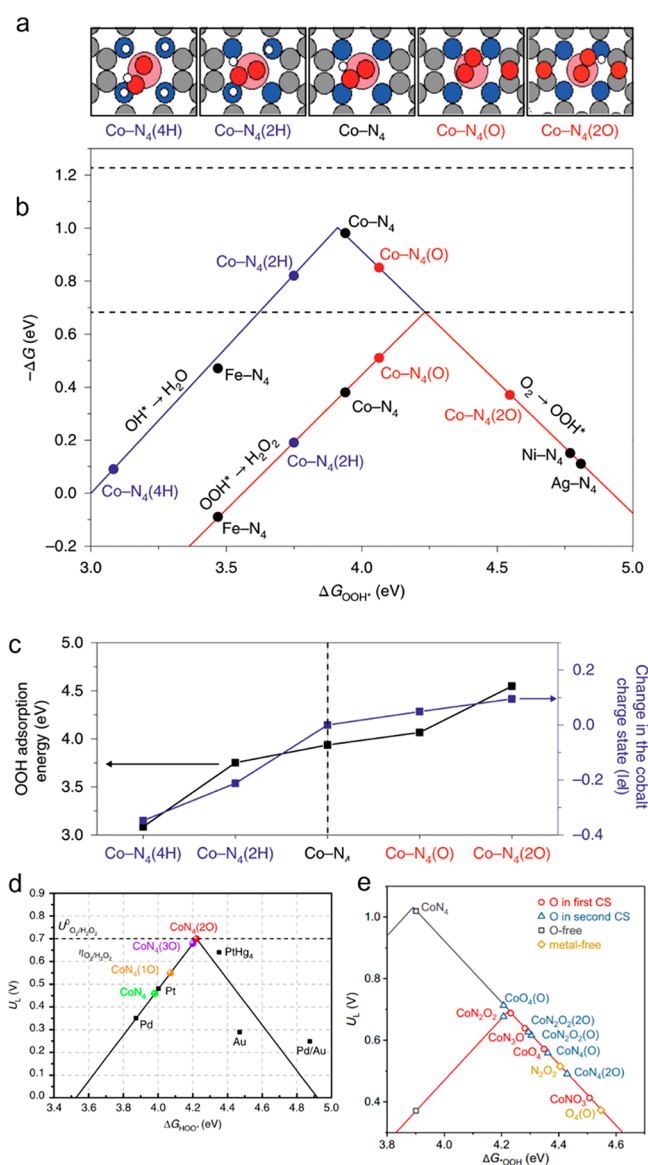


Figure 22. (a) M–N₄–graphene with *OOH and different functional groups. (b) Calculated catalytic activity volcanoes for the production of H_2O (blue) and H_2O_2 (red) via the ORR. Black data points represent M–N₄/graphenes (M = Co, Ni, Fe, Pt, Ag, and Ru) that are used to construct the activity volcanoes. Blue and red data points represent Co–N₄/graphene with 4H * /2H * and O * /2O * adsorbed near the cobalt atom, respectively. (c) Calculated OOH * adsorption energies and relative charge states of the cobalt metal center in Co–N₄/graphene with 4H * , 2H * , O * , or 2O * adsorbed near the cobalt atom. (d,e) Calculated ORR volcano plot for Co–N₄ and derivatives. (a–c) Adapted with permission from ref 114. Copyright 2020 Nature. (d) Adapted with permission from ref 115. Copyright 2020 Nature. (e) Adapted with permission from ref 116. Copyright 2021 American Chemical Society.

motif, which is confirmed in their NEXAFS measurements. As shown in Figure 22d, Co–N₄ site promoted by two *O groups is found to be an optimal configuration for H_2O_2 synthesis. Moreover, the barrier of HOH^* dissociation is evaluated, and it is found that the already high barrier (1.4 eV) can be further increased (by 0.1–0.2 eV) by epoxy modification, thus the H_2O_2 selectivity can be enhanced by introducing epoxy groups. We note that such barrier values may be exaggerated as the dissociation of HOH^* does not necessarily end with *OH and

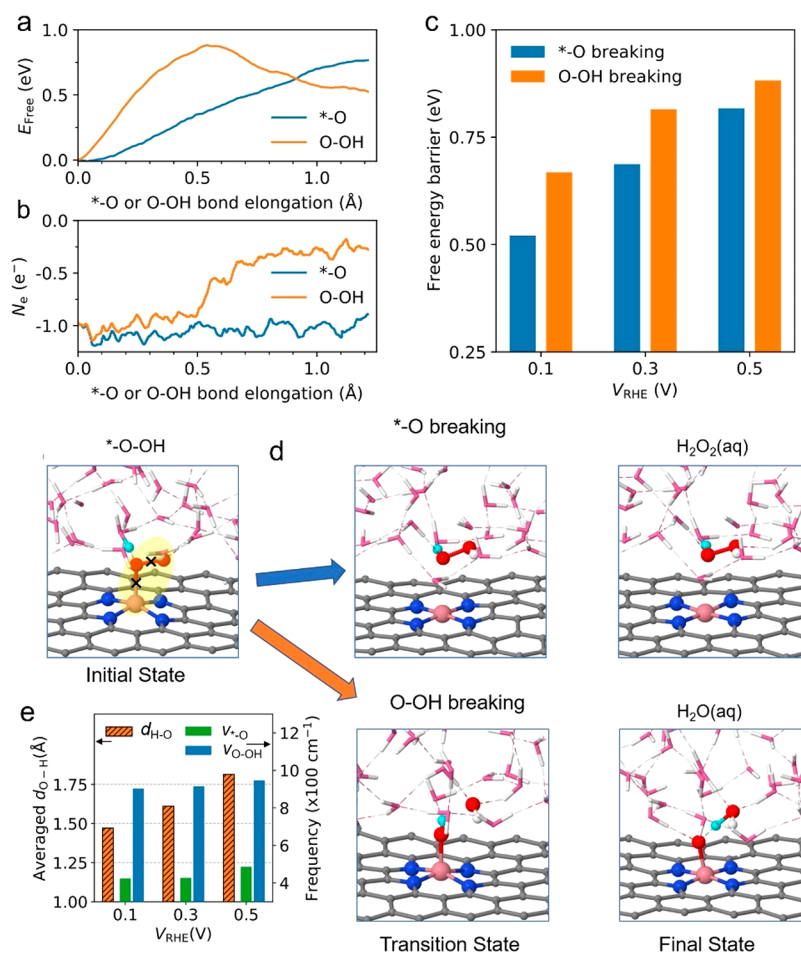


Figure 23. Free energy profile (a) and evolution of net electronic charges (b) during the breakings of $*\text{O}$ and $\text{O}-\text{OH}$ bonds in $*\text{O}-\text{OH}$ on $\text{Co}-\text{N}_4$ under 0.5 V vs RHE. (c) Activation energies under different potentials. (d) Structure evolutions under 0.3 V vs RHE: pink, Co; gray, C; red, O; white, H; cyan, proton. (e) Average length of the hydrogen bond to the former O in $*\text{O}-\text{OH}$, and the vibrational frequencies of $*\text{O}$ and $\text{O}-\text{OH}$ bonds, all for the initial state. Adapted with permission from ref 111. Copyright 2021 American Chemical Society.

$*\text{O}$ both on the metal site, instead, OH^- may form and become stabilized by H_2O molecules in the solution.

Qiao et al.¹¹⁶ showed that replacing the metal coordinated N by O also weakens the adsorption of OOH. More significantly, they found that the active site shifts from center Co atom to O-adjacent C atom, which is confirmed in experiments via poisoning the Co site with thiocyanide (SCN^-). The volcano plot of various sites is shown in Figure 22e. The structure with N and O in the first coordinate sphere (CS) of Co, and an adsorbed O in the outer sphere is proposed to be the most active site that gives the observed outstanding activity and selectivity of >95% for acidic H_2O_2 electrosynthesis. Similarly, Tian, Lu, and Chen et al.¹¹⁷ found that carbon site, instead of the M site, of the $\text{M}-\text{O}-\text{C}$ ($\text{M} = \text{Al}, \text{Ga}$) motif is active for H_2O_2 synthesis. Coordination engineering has been shown to be an effective method to tune the catalytic performance for ORR to H_2O_2 in other works as well.^{117–120}

Although $\text{Co}-\text{N}_4$ shows high selectivity for the 2e product H_2O_2 , the thermodynamics cannot explain it. The 4e and 2e pathways diverge from the $*\text{O}-\text{OH}$ (Figure 23d). Breaking the $*\text{O}$ bond will result in the 2e pathway, generating H_2O_2 , while breaking the $\text{O}-\text{OH}$ bond will lead to the 4e pathway and generate H_2O . DFT calculations, regardless of the models (e.g., CHEM, constant potential model) always show that breaking the $\text{O}-\text{O}$ bond is much more thermodynamically favorable than

the $*\text{O}$ bond (in other words, H_2O formation is much more thermodynamically favorable than H_2O_2), which does not explain the high selectivity of H_2O_2 . To understand the origin of the selectivity, Liu et al.¹¹¹ developed the CP-HS-DM and used it to study the kinetics of $*\text{O}-\text{OH}$ bond breakings during ORR on $\text{Co}-\text{N}_4$. The free energy profile calculated at 0.7 V vs RHE at pH = 0, as shown in Figure 23a, indicates that although the $*\text{O}$ breaking has a higher energy for the final state, it has a lower barrier than the $\text{O}-\text{O}$ breaking, suggesting that 2e path is kinetically favored and explaining the experimentally observed selectivity. Their results for acid conditions show that decreasing the potential results in a larger difference in the activation energy between $*\text{O}$ and $\text{O}-\text{OH}$ breakings, thereby increasing the selectivity for the H_2O_2 formation. This is also consistent with the experiments.¹²¹ The more preferred H_2O_2 formation under lower potential is due to the synergistical effects of surface charge and hydrogen bonding. Decreasing the potential gives more negative charges on the surface, some of which are transferred to the former O in $*\text{O}-\text{OH}$, leading to a stronger H bond with nearby H_2O molecule. This makes the structure of the reactant closer to H_2O_2 , thereby favoring its formation (Figure 23d).

5.2.2. X-C. Liu and Wang et al.¹²² found that carbon materials doping with nonmetal elements (B, N, P, S) can significantly enhance the ORR to H_2O_2 activity and selectivity.

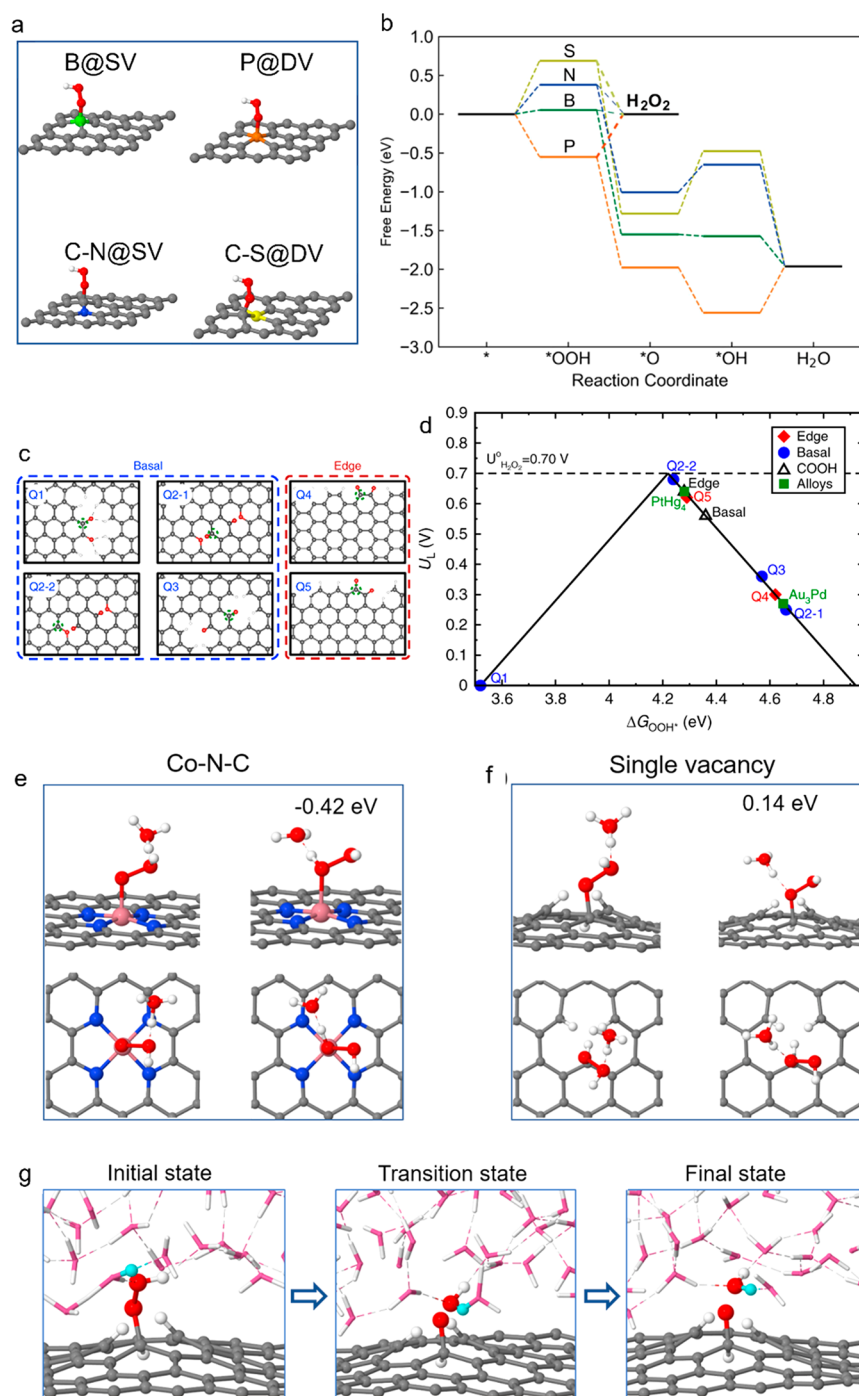


Figure 24. (a) Preferred OOH adsorption configuration and (b) the corresponding thermodynamic free energy profile of ORR, calculated using constant potential method at 0.7 V *vs* RHE. (c,d) Structures of oxidized graphene and theoretical thermodynamic onset potential as a function of the binding energy of OOH. (e,f) H_3O^+ bonded with different O in $^*\text{O}-\text{OH}$ on Co- N_4 (e) and single vacancy defect in graphene (f). The relative adsorption energies are also shown. (g) Structure evolution of the O-OH breaking on single vacancy defect. (a,b) Adapted with permission from ref 122. Copyright 2021 Nature. (c,d) Adapted with permission from ref 126. Copyright 2018 Nature. (e-g) Adapted with permission from ref 111. Copyright 2021 American Chemical Society.

Particularly, B-doped carbon catalyst shows 85–90% H_2O_2 selectivity at current densities up to 300 mA cm^{-2} , which is close to industry standards. To understand the mechanism, they considered three doping configurations (single vacancy, double vacancy, 5577 defect) and studied adsorption of the key intermediate $^*\text{OOH}$ on different doping sites (Figure 24a) at 0.7 V *vs* RHE. It is found that OOH prefers different sites for different doping elements, indicating the atomistic diversity of

the active sites resulted from similar doping process in experiments. Using constant-potential model, they calculated the free energy profiles (Figure 24b) of the ORR paths on the doped sites. Indeed, B is the best among all the four studied dopants and has nearly zero thermodynamic barrier for H_2O_2 formation. Furthermore, they evaluated the kinetic barriers of the breaking of $^*\text{-O}$ and $\text{O}-\text{OH}$ bonds in $^*\text{OOH}$ at 0.7 V *vs* RHE. Like the case of Co- N_4 , the $^*\text{-O}$ breaking on B-C is also

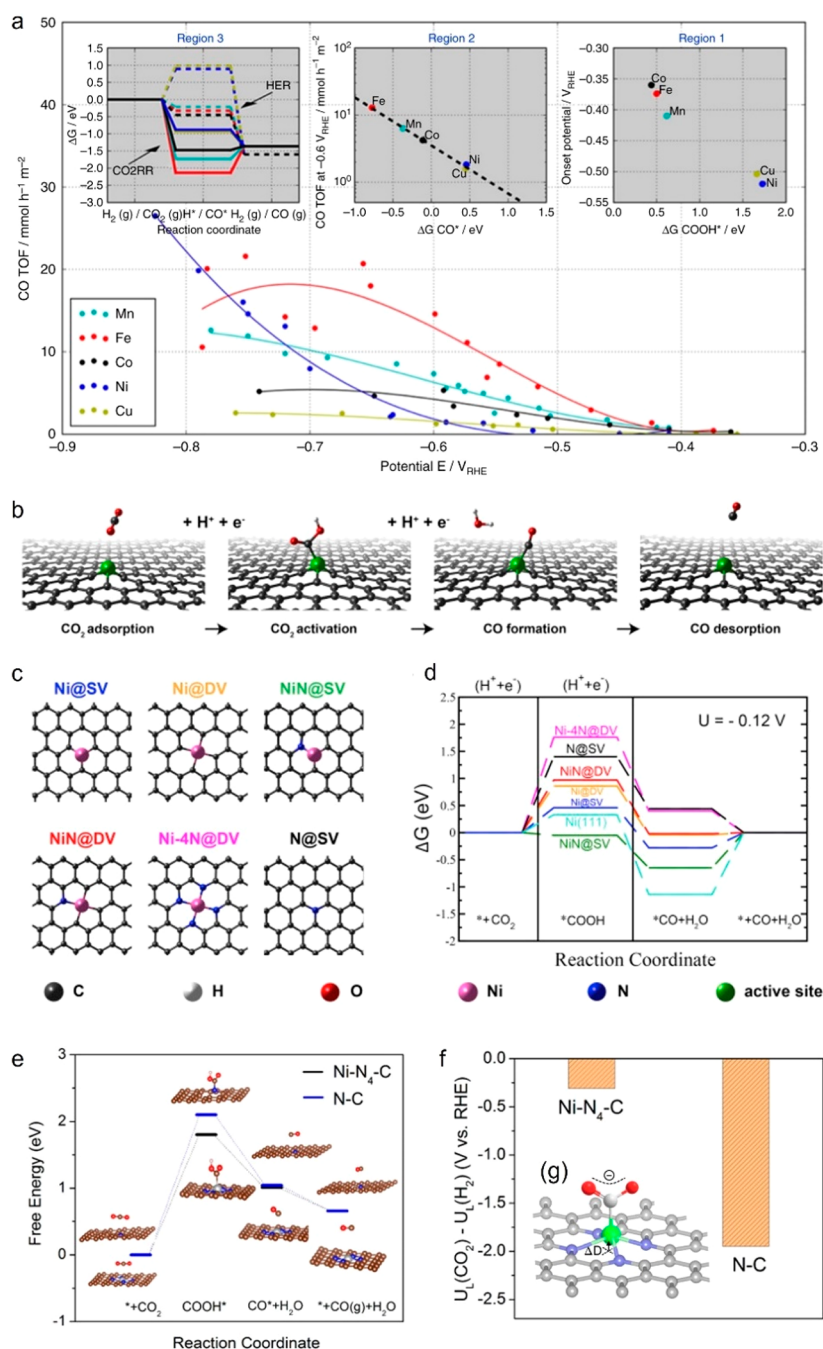


Figure 25. (a) Experimental CO production turnover frequency (TOF) of the M-N-C catalysts vs applied IR-corrected electrode potential. The regions in the insets are divided by the potential; region 1, ~ -0.45 V vs RHE; region 2, ~ -0.6 V; region 3, < -0.7 V. (b) Schematic of the reaction steps of electrocatalytic CO₂ to CO reduction. (c) Different atomic configurations in graphene for the DFT calculations. (d) CHEM calculated thermodynamic free energy diagram of CO₂ to CO conversion on different atomic sites under an equilibrium potential of -0.12 V vs RHE. (e) Thermodynamic free energy diagram for Ni-N₄ and N doped graphene. (f) Difference in onset potentials for CO₂ reduction and H₂ evolution. (g) experimentally measured intermediate during CO₂R. (a) Reproduced with permission from ref 128. Copyright 2017 Nature. (b-d) Reproduced with permission from ref 130. Copyright 2017 Science Direct. (e,f) Reproduced with permission from ref 131. Copyright 2017 American Chemical Society. (g) Reproduced with permission from ref 132. Copyright 2018 Nature.

found to have a 0.17 eV lower kinetic barrier than O-OH breaking, which is in agreement with the observed high H₂O₂ selectivity.

Oxidized carbon without metal also shows high activity and selectivity for ORR to H₂O₂ under alkaline conditions. Cui et al.¹²³ developed a surface oxidation treatment to enhance the activity and selectivity of carbon nanotubes (CNTs). The oxidation lowers the overpotential by ~ 130 mV at 0.2 mA while

simultaneously increasing the selectivity from ~ 60 to $\sim 90\%$. The ORR activity and selectivity demonstrate a nearly linear correlation as a function of oxygen content. This surface oxidation approach is also effective for enhancing the ORR performance of other types of carbon material. To identify the active site structure, the authors considered the structures of graphene decorated with different oxygen functional groups at edge or basal plane. The functional groups include carboxyl

($-\text{COOH}$, $M = \text{H}$ or Na), carbonyl ($\text{C}=\text{O}$), etheric ($\text{O}-\text{C}-\text{O}$), and hydroxyl ($-\text{OH}$). The DFT calculations with CHEM show that the most active sites are the $-\text{COOH}$ functional group in the armchair edge as well as the $\text{C}-\text{O}-\text{C}$ functional group in the basal plane of the graphene, and these active functional groups are supported by further controlled experiments.

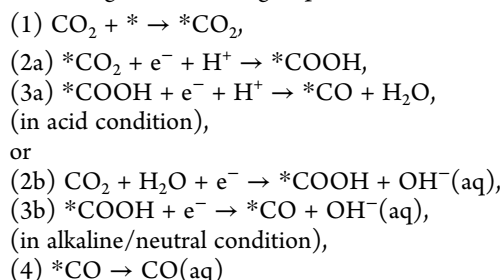
McCloskey et al.¹²⁴ demonstrated that the mildly reduced graphene oxide electrocatalyst exhibits highly selective and stable performance for ORR to H_2O_2 at low overpotentials (<10 mV) under basic conditions. Spectroscopic structural characterization and in situ Raman spectroelectrochemistry show that sp^2 -hybridized carbon of the ring ether ($-\text{C}-\text{O}-\text{C}-$) defects along sheet edges are the most active sites. Joo et al.¹²⁵ synthesized a carbon nanocatalyst with abundant oxygenated graphitic edge sites. It has a higher activity than the basal plane-rich catalyst and has a high H_2O_2 selectivity and stability. Importantly, it is found that the activity is closely related to the heterogeneous electron transfer kinetics of the carbon-based catalyst, suggesting that first outer-sphere electron transfer to O_2 is a critical step. Li, Siahrostami, and Baek et al.¹²⁶ further studied the nature of the active sites in carbon catalyst. They decorated the edge with various oxygen functional groups. It is found that quinone-enriched samples exhibit high activity and selectivity with a H_2O_2 yield ratio of up to 97.8% at 0.75 V vs RHE. They performed DFT calculations based on CHEM to study the activity trends of different possible quinone functional groups in the edge and basal plane (Figure 24c,d). The armchair edge with two edge atoms passivated by O shows a high thermodynamic onset potential.

(Oxidized) carbon catalysts generally have a lower activity and selectivity in acid conditions than in alkaline conditions for ORR to H_2O_2 . To understand the origin, Chorkendorff et al.¹²⁷ investigated seven commercially available carbon materials. They found that different carbon catalysts have very different faradaic efficiencies, spanning in a wide range of 18–82%. To determine the origin of these differences, they employed various experimental techniques. They found that the surface oxygen groups, nitrogen and sulfur content, and the metal content (when ~ 10 ppm) do not show clear effects. Instead, carbons with high selectivities for the 2e pathway have more aliphatic-like surface “defect” structures. Liu et al.¹¹¹ provided an explanation for the lower H_2O_2 selectivity in acidic conditions. They considered a single vacancy defect in graphene, where the three C atoms near the vacancy are passivated by H (the passivation is very stable according to formation energy at $V_{\text{RHE}} = 0.7$ V). The $^*\text{OOH}$ can form on one of these three C atoms during the ORR. It is found that the proton prefers the latter O of the $^*-\text{O}-\text{OH}$ (Figure 24e,f, also confirmed in the constant potential AIMD simulations; note this is different from the case of $\text{Co}-\text{N}_4$ where the proton prefers the former O), due to the steric effect of the passivating H. Because of the proximity, in the proton immediately stabilizes the OH anion once it is formed from the $\text{O}-\text{OH}$ breaking and thus facilitate this pathway (as shown by the CP-FS-DM simulations in Figure 24g). Thus, the 4e pathway ($\text{O}-\text{OH}$ breaking) is more favored in acid conditions than that in neutral/alkaline conditions, explaining the lower selectivity for H_2O_2 on carbon catalyst in acid conditions. It is anticipated that for the sites forming short bond with the $^*\text{OOH}$ (like C site), decreasing pH would generally lower the selectivity of H_2O_2 production, because for those sites, the proton is the difficult to access the former O of $^*-\text{O}-\text{OH}$ (the one directly bonded to the site), and the preference to

later O would help break the $\text{O}-\text{O}$ breaking and favor the H_2O formation.

6. CARBON DIOXIDE REDUCTION (CO_2R)

Electrochemical CO_2 reduction (CO_2R) converts CO_2 to value-added chemicals such as CO , HCOOH , CH_4 , CH_3OH , C_2H_6 , $\text{C}_2\text{H}_5\text{OH}$ etc. It is an attractive technique to reduce carbon emission. The CO_2R can have multiple pathways leading to multiple products. Most of the 2D catalysts yield CO , which is produced through the following steps:



If CO binds strongly with the catalyst, then it can be further protonated to generate other products. Because the standard electrode potentials for CO_2R are close to SHE (ca. -0.1 V vs SHE), the HER often competes, yielding H_2 as a side product.

6.1. $M-\text{X}-\text{C}$

Hao, Rossmeis, and Strasser et al.¹²⁸ studied the $M-\text{N}-\text{C}$ (where $M = \text{Mn}, \text{Fe}, \text{Co}, \text{Ni}, \text{Cu}$) for CO_2R . They categorize the potential into three regions: high potential region (~ -0.45 V vs RHE), intermediate (~ -0.6 V), and low potential regions (< -0.7 V). Fe shows the highest turnover frequency (TOF) for CO formation at high and intermediate potentials, while Ni is the best at low potential (Figure 25a). DFT calculations based on $M-\text{N}_4$ model and CHEM were performed to understand the rate-limiting steps in different regions. As shown in Figure 25a, the correlation between the experimental onset potential and the DFT calculated formation energy of $^*\text{COOH}$ at high potential region suggests that the rate limiting step is $^*\text{COOH}$ formation. Similarly, the correlation between the CO TOF and the formation energy of $^*\text{CO}$ at intermediate potential suggests that the rate limiting step is $^*\text{CO}$ formation. In the low potential region, the calculated free energy change for $^*\text{CO} \rightarrow \text{CO}(\text{g})$ and the thermodynamic free energy diagram for HER suggest that the HER is more favorable than CO_2R on Mn, Fe, and Co as they bind CO too strongly, while the opposite is true for Cu and Ni. Note that DFT gives similar formation energies of intermediates for Ni and Cu, suggesting that they should have similar performance. However, Cu is worse than Ni at low potentials, which is attributed to the instability of the $\text{Cu}-\text{N}-\text{C}$, where the N-coordinated Cu atoms are reduced to nanoparticles.¹²⁹

Wang et al.¹³⁰ showed that $\text{Ni}-\text{N}-\text{C}$ has high Faradaic efficiencies $>90\%$ at high currents up to ~ 60 mA/mg. They considered a variety of possible Ni sites on graphene with and without N codoping for CO_2R (Figure 25b,c). Using CHEM with empirical solvation correction for intermediates, they found Ni at single vacancy site and Ni at double vacancy site (both without N) are the two most active sites for CO_2R . Compared to Ni(111) metal surface, these single Ni sites show not only lower thermodynamic barriers for CO_2R but also higher HER thermodynamic barriers. These active site structures are consistent with the atom probe tomography (APT) characterizations, which indicate that the majority of the Ni atoms are not coordinated with N. Note that the CHEM also shows that the

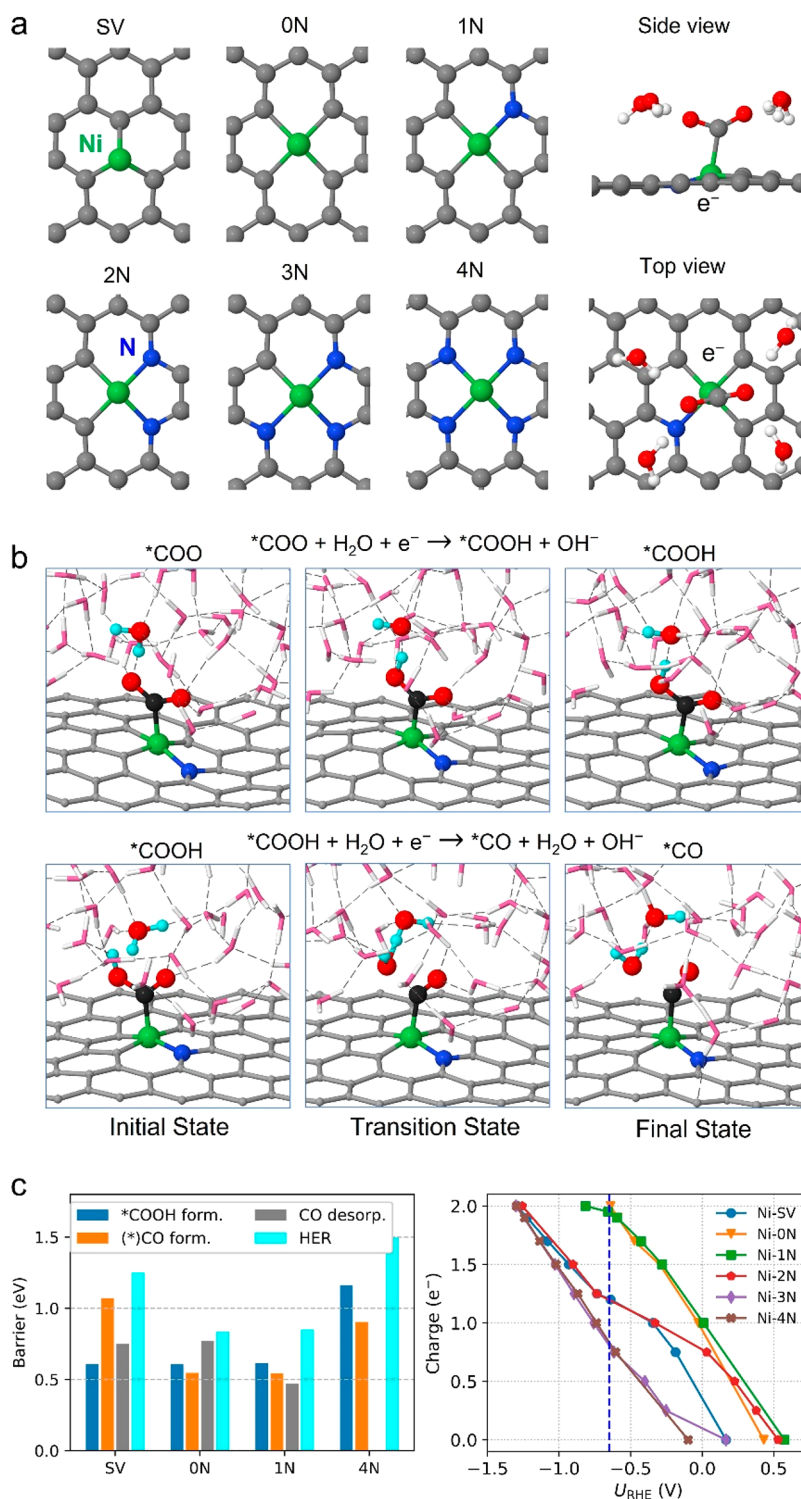


Figure 26. (a) Possible site structures in Ni–N–C catalyst for CO₂R. The top and bottom views at the right show the chemisorption of CO₂ on the Ni–N₁C₃ site, when both the hydrogen bonding and the net electronic charge on surface are present. (b) Atomic structure evolutions of *CO₂ → *COOH and *COOH → *CO, simulated using CP-HS-DM. (c) Energy barriers of different steps on different sites, and the number of net electronic charges as a function of the potential. Adapted with permission from ref 66. Copyright 2020 American Chemical Society.

onset potential of HER is always higher than that of CO₂R for all the sites, suggesting that they should have higher selectivity for HER instead of CO₂R, which contradicts the experimentally observed high CO₂R selectivity. Such a contradiction indicates that thermodynamics analysis may fail to predict selectivity, and kinetic barriers need to be considered.

Xie et al.¹³¹ synthesized the Ni–N–C catalyst with exclusively Ni–N₄ sites through a topochemical transformation approach. The catalyst achieves a Faradaic efficiency over 90% for CO from –0.5 to –0.9 V, with a maximum of 99% at –0.81 V (corresponding current density of 28.6 mA cm^{–2}). The thermodynamic free energy diagram calculated using CHEM indicates that the Ni–N₄ site has a higher activity and selectivity

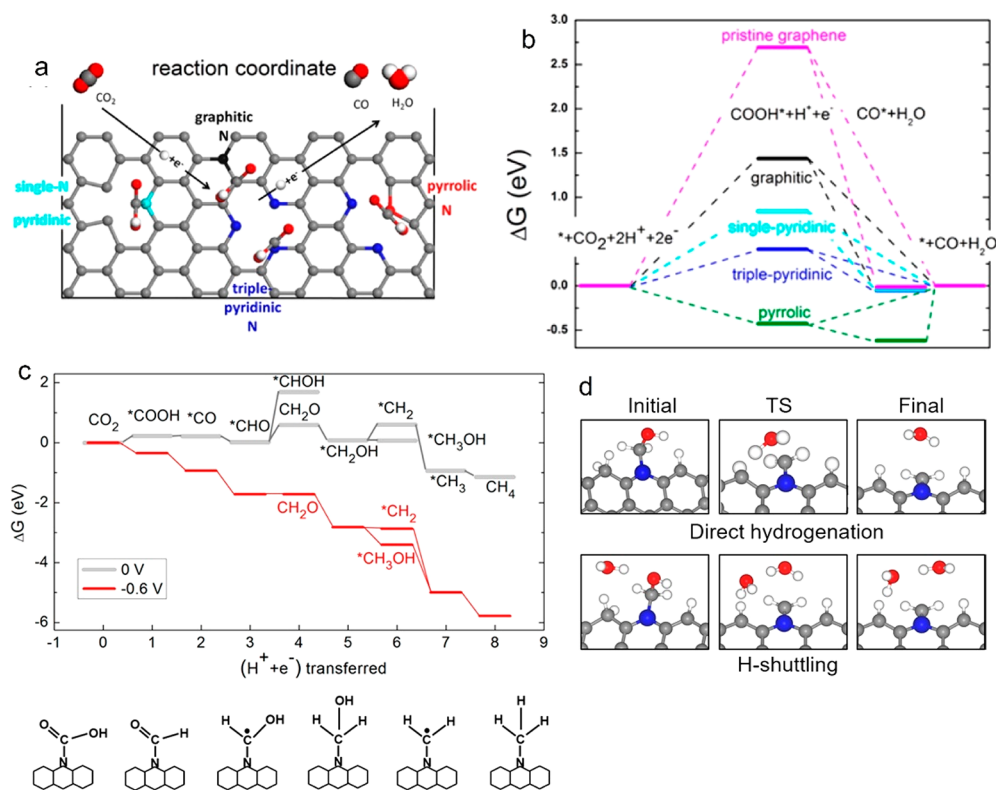


Figure 27. (a) Illustration of different possible sites in N doped graphene for CO₂R. (b) Corresponding thermodynamic free energy diagram. (c) (top) Thermodynamic free energy diagram for CO₂R to CH₃OH and CH₄ on pyridinic N at zigzag edge. (bottom) Schematic for selected intermediate states. (d) Reaction step of $*CH_2OH \rightarrow *CH_2$ through direct hydrogenation (1.9 eV barrier) or H-shuttling pathway (0.6 eV barrier). (a,b) Adapted with permission from ref 142. Copyright 2016 American Chemical Society. (c,d) Adapted with permission from ref 145. Copyright 2017 American Chemical Society.

than N doped graphene for CO₂R. Note that the onset potential is calculated to be <-1 V due to the high formation energy of $*COOH$, consistent with the DFT results in ref 130. Also, similar to ref 130, the calculated onset potential of HER is always higher than that of CO₂R for all the sites, suggesting that they should have higher selectivity for HER instead of CO₂R, which contradicts the experimentally observed high CO₂R selectivity.

Huang, Zhang, and Bin Liu et al.^{132,133} used operando X-ray absorption and photoelectron spectroscopy measurements and identified the monovalent Ni (Ni(I)) in Ni–N₄ as an active site for CO₂R. Particularly, their measurements indicate that CO₂ takes one electron from Ni(I) upon adsorption, resulting a charged CO₂[−] and Ni(II). These were confirmed in their later work.¹⁶ Further, through combination with a kinetics study, they found that the rate-determining step is $*CO_2^- + H^+ \rightarrow *COOH$. These two works suggest that CO₂ is chemically adsorbed during CO₂R.

Liu et al.⁶⁶ studied the atomistic kinetics of CO₂R on Ni–N_xC_y. They considered a variety of site structures as shown in Figure 26a. They found that the net electronic charges accumulated at the Ni site and the hydrogen bonding with the water are necessary to stabilize the chemisorption of CO₂ on most sites, otherwise the CO₂ will be physisorbed and keep the linear configuration. After determining the net electronic charge under the working potential, they used AIMD in conjunction with the “slow-growth” sampling approach to simulate the reaction kinetics (Figure 26b) and evaluate the energy barriers for different reaction steps on different sites (Figure 26c). It is found that the Ni–N₁C₃ structure has the lowest barriers for CO₂R and a high barrier for HER (-0.6 V vs RHE). Its activity is

attributed to the proper number of N, which has two roles: first, N substitution shifts up the Fermi level of the carbon catalyst at charge neutral state, thus, the catalyst carries less negative electronic charges under the working potential (Figure 26c). This impedes electrochemical reduction, which prefers more electrons accumulated at the site to facilitate the electron transfer. On the other hand, N doping weakens the binding between the M and the adsorbate by partially donating its p electrons to the d orbitals of M site. This benefits the desorption of the CO product. The competition of these effects results in Ni–N₁C₃ as the most active site. Its high selectivity for CO₂R over HER is attributed to hydrogen bonding, which promotes the reaction that produces polar intermediates by stabilizing the intermediates and facilitating the H transfer from water. This work suggests that the charge capacity is a critical factor to evaluate the catalytic site performance and highlights the role of hydrogen bonding. Note that at lower potential, the electrochemical steps will be facile, and the difference in catalytic activity between different sites will be determined by the chemical steps. Thus, Ni–N₄ may become the most active site due to its weakest binding with CO.

Using the hybrid model for solution, i.e., three H₂O molecules together with implicit solvation, Luo and Goddard et al.¹³⁴ used GCP-K model to study the kinetics of CO₂R on Ni–N₂C₂, Ni–N₃C₁, and Ni–N₄ sites. The reaction barriers are obtained through CI-NEB method at constant charge and then transformed to constant potential. Similar as in Liu’s work, they also found a hybrid site Ni–N₂C₂ (while the Ni–N₁C₃ site identified in Liu’s work is not considered in Luo’s work) to be

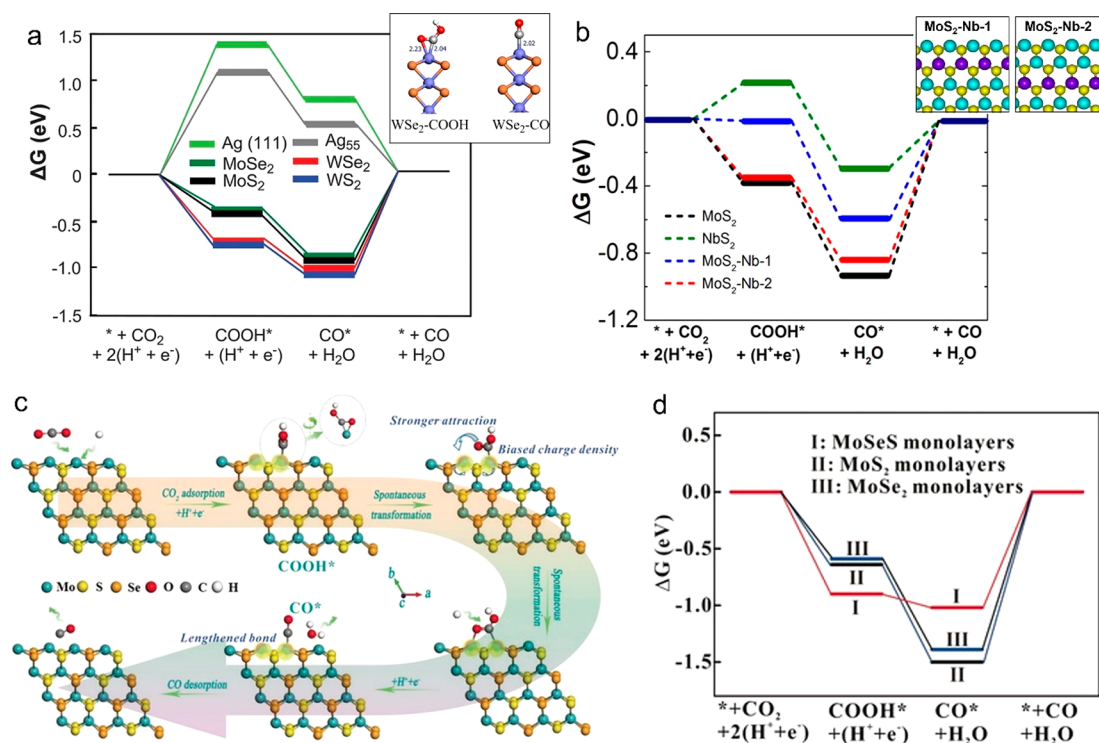


Figure 28. Thermodynamic free energy diagrams for CO₂R to CO on the M-terminated edges of different MX₂ (a) and of Nb-doped MoS₂ (b). Insets show the atomic structures. (c) Schematic of CO₂R on MoSSe alloy. (d) Corresponding free energy diagram. (a) Adapted with permission from ref 148. Copyright 2016 Science. (b) Adapted with permission from ref 149. Copyright 2017 American Chemical Society. (c,d) Reproduced with permission from ref 150. Copyright 2017 Wiley-VCH.

most active at moderate potential, while Ni–N₄ site delivers the highest current density under more reductive potential.

Beyond Ni–N–C catalysts, a variety of other metal and nonmetal elements doping in graphene has been explored. For example, Shao et al.¹³⁵ combined in situ infrared absorption spectroscopy and DFT calculations to show that the Fe–N₄ in the complete graphitic layer is inactive due to the poisoning by strongly adsorbed CO. Instead, the Fe–N₄ in a defective graphitic layer has balanced adsorption energies and thus a high activity and selectivity. Chen and Peng et al.¹³⁶ synthesized Fe–N₄ sites with axial O coordination which demonstrated nearly 100% CO selectivity under a wide range of potentials. Their DFT calculations show that the axial O from pyrrolic site in parallel layer of graphene is critical for the superior performance: O-coordination induced electronic localization not only promotes the CO desorption but also hinders the HER by weakening the M–CO and M–H bonds. Sun, Xie, et al.¹³⁷ reported Sn–N–C as a highly efficient formate production catalyst with an onset overpotential down to 0.06 V and a turnover frequency up to 11930 h⁻¹. He et al.¹³⁸ synthesized Cu–N–C that can generate methanol with 44% Faradaic efficiency in liquid phase. Min, Lin, and Zhu et al.¹³⁹ showed that Cu–N–O sites at the edge of carbon dot has high Faradaic efficiency (78%) and high CH₄ selectivity (99%) with current density of 40 mA·cm⁻² in aqueous electrolytes has been achieved. Using DFT-CHEM and a cluster model, they calculated CO₂R intermediates on Cu–N₂O₂ site at the edge of 2D carbon dot and found that the site binds COOH and CO significantly stronger than Cu–N₄ site at the basal plane, in agreement with the high activity and the further reduction of *CO.

Recently, Strasse, and Chan et al.¹⁴⁰ compared the activity of M–N–C catalysts with transition metal (TM) catalysts for CO₂R to CO. The DFT calculations show that the electron transfer to CO₂ is facile for both TM and M–N–C. However, the CO₂ adsorption is generally the rate limiting step on TM, whereas M–X–C can be limited by either CO₂ adsorption or by the subsequent proton-coupled electron-transfer step to form COOH*. These predictions are compared with the experimental measurement of the activity dependence on pH. The activities of TM and M–N–C catalysts are mapped by a single volcano plot that uses both the CO₂ and COOH binding strengths as descriptors. The authors further show that the discrete and narrow d states of M–N–C catalysts help stabilize the larger adsorbate dipoles, which results in a higher activity than TM catalysts.

6.2. X–C

N-doped graphene is also a promising catalyst for CO₂R.¹⁴¹ Yakobson, Lou, Ajayan, and co-workers¹⁴² reported that N-doped 3D graphene foam has a superior activity over Au and Ag with similar maximum Faradaic efficiency and better stability for CO production. DFT calculations based on CHEM found that graphitic N enhances the binding of the neighboring C atom with COOH but is still too weak to be active; pyrrolic N binds COOH directly but the binding is too strong; pyridinic N instead has moderate binding and thus the best catalytic activity (Figure 27a,b). Siahrostami et al.¹⁴³ employed DFT-CHEM calculations for various defect sites in N-doped and nondoped graphene. They found that adsorption energies of COOH* and CO* do not follow the linear scaling. Several sites are found to be active, and pyridinic-N is identified to be the most selective site for the CO₂R over HER. Ding, Kenis, and Ajayan et al.¹⁴⁴ reported that nanometer-sized N-doped graphene quantum dots

(NGQDs) can catalyze the CO₂R into multicarbon hydrocarbons and oxygenates with a selectivity for ethylene and ethanol conversions reaching 45%. To understand this, Zou and Jakobson et al.¹⁴⁵ performed DFT calculations based on CHEM (Figure 27c,d). They found that pyridinic N at zigzag edge binds COOH more strongly than that in the basal plane and is thus more active. Although thermodynamical free energy diagram shows that the formation of CH₃OH is more favorable over CH₄, the calculated energy barriers (with one water molecule in the model) for the *CH₂OH → *CH₂ and *CH₂OH → *CH₃OH steps indicate that the former step is more kinetically favorable via water molecule mediated proton shuttling, which will further lead to CH₄, explaining the experimentally observed preference for CH₄. Furthermore, the *CH₂ provides active sites for the coupling with CO to generate C₂ products, including both C₂H₄ and C₂H₅OH. It should be noted that these calculations assume that there is no H terminating the pyridinic N, while DFT calculations based on CHEM indicate the opposite under CO₂R conditions, which may eliminate/suppress the activity of pyridinic N.

6.3. MX₂

Although under aqueous conditions MX₂ have higher selectivity for the HER relative to CO₂R,¹⁴⁶ adding an ionic liquid can promote the CO₂R selectivity. The ionic liquid can help bind CO₂ and stabilize the CO₂R reaction intermediates. Salehi-Khojin et al.¹⁴⁷ demonstrated CO₂R to CO on MoS₂ edge in 96 mol % water and 4 mol % EMIM-BF₄ solution. The activity is attributed to the high d-electron density around Fermi level and low work function at the Mo-terminated edges of MoS₂. The edge activity is further confirmed by vertically aligned MoS₂, which possesses a higher performance than bulk. The authors also studied the effect of water mole fraction on the catalytic activity. The CO₂R current density increases as the water fraction increases, reaching a maximum in the 96 mol % water solution and then rapidly decreases. The best performance at 96 mol % water is attributed to the high concentration of H⁺ (pH~4) in the reaction media and the low viscosity of the solution, which helps the transport of the reactants toward the catalytic sites.

Curtiss and Salehi-Khojin et al.¹⁴⁸ reported a MX₂ nano-architecture for CO₂R to CO. The electrolyte is composed of 50 volume percent (vol %) EMIM-BF₄ and 50 vol % deionized water, which gives the highest proton concentration (lowest pH: 3.2) among different concentrations of water–ionic liquid and thus maximizes CO₂R activity. WSe₂ nanoflakes show a current density of 18.95 mA cm⁻², CO Faradaic efficiency of 24%, and CO formation turnover frequency of 0.28 s⁻¹ at a low overpotential of 0.054 V. Thermodynamic free energy diagrams calculated using DFT with CHEM for the M-terminated edges (Figure 28a) show that the COOH* formation is exothermic, and the reaction is limited by the CO desorption, which requires ~1 eV energy. The diagram also shows that the MoSe₂ is better than the other MX₂, as it has the weakest CO binding; however, experimentally WSe₂ is measured to be the best. Interestingly, the activity trend is in line with both the measured and calculated work function trend, MoS₂ > WS₂ > MoSe₂ > WSe₂, indicating the critical role of the electron transfer properties of the catalysts in this reaction.

Salehi-Khojin et al.¹⁴⁹ demonstrated that 5% niobium (Nb)-doped vertically aligned MoS₂ can have 1 order of magnitude higher CO formation TOF than pristine MoS₂ at an overpotential range of 0.05–0.15 V in electrolyte composed of 50 vol

% EMIM-BF₄ and 50 vol % deionized water. Their DFT calculations show that doping Nb atoms near the Mo edge of MoS₂ decreases the binding strength of CO on Mo edge while keeping the formation of *COOH and *CO exothermic (Figure 28b), thereby giving a faster turnover for CO desorption than pure MoS₂. Xie et al.¹⁵⁰ showed that in 96 mol % water and 4 mol % EMIM-BF₄ solution, MoSeS alloy monolayers have a 45.2% Faradaic efficiency for CO production in ionic liquid aqueous solution, larger than that of MoS₂ monolayers (16.6%) and MoSe₂ monolayers (30.5%) at -1.15 V vs RHE. More importantly, the yields of CO and H₂ followed an approximate 1:1 ratio as in syngas, a key feedstock to produce olefins by Fischer–Tropsch synthesis. DFT calculations with CHEM for the M terminated edges (Figure 28c,d) show that the alloy not only has a stronger binding with the COOH but also has a weaker binding with the CO (which is confirmed by CO temperature-programmed desorption and electrostripping experiments), thereby facilitating the CO₂R to CO. Stadler et al.¹⁵¹ reported that semimetallic TiS₂ can reduce CO₂ to CO and formate, with a combined Faradaic yield beyond 95% and overpotential below 0.4 V at CO current density of 5 mA cm⁻². In situ Fourier transform infrared studies show that CO₂ binds to the S instead of Ti, forming a monothiocarbonate intermediate.

To better understand the mechanism, it would be desired to comprehensively model the CO₂R and HER with and without ionic liquid on various possible sites beyond the simple metal-terminated edges. Experimentally, Jaramillo et al.¹⁵² offered some insights into the effect of 0.1 M [EMIM]Cl on HER on Cu, Ag, and Fe electrodes. It was found that [EMIM]Cl suppresses HER under acidic conditions especially for Fe, while does not cause suppression in basic electrolytes. This is because the [EMIM]⁺ cations strongly interact with the electrode, which limits the diffusion of protons (the H source in acid conditions) to the catalyst surface in acidic conditions without influencing the diffusion of neutral water molecules (the H source in alkaline conditions). It was also shown that the [EMIM]Cl is susceptible to electrochemical breakdown with formate and methanol among the products, leading to difficulties in quantifying the CO₂R products.

7. CONCLUSION AND PERSPECTIVE

As shown in the previous sections, there is still much debate on the atomistic mechanisms of the common 2D electrocatalysts. Although first-principles methods in principle can give accurate reaction information for a given catalytic site and thus resolve the catalytic mechanism, in practice they are limited by the high computational cost and the complexity of the system, and thus certain compromises to the accuracy must be made. Depending on how this compromise is made, different models are developed. However, as we have seen through the above examples, the current models can give very different or even contradicting results and understandings. Also, many studies focus on thermodynamics, while it is the kinetics that directly determines the reaction rate; accurate calculation of the reaction kinetics, especially electrochemical kinetics, on a given structure will play a decisive role in resolving the catalytic site structure and mechanism. Therefore, it is important to develop advanced first-principles models, particularly kinetic models, with higher accuracy but affordable computational cost.

The effect of electrode potential is getting more and more attention in literature, while the explicit solvation effect remains to be a challenge, as it requires extensive sampling of numerous

configurations of water molecules, their interactions with reaction species, and the structure-dependent charge states in the presence of electrode potential. This consequently impedes the simulation of kinetics especially for the steps directly involving water. The CP-HS-DM makes an initial attempt to sample both the atomic structures and charge states along the reaction pathway, thereby giving kinetic information. Yet due to the high computational cost of first-principles calculations, this model is limited to a small size and the sampling may still not be enough. A promising solution to this problem is to replace the quantum mechanical description of the interatom interactions with a force field, which is computationally much cheaper and thus can afford a larger system and extensive sampling. The force field may be generated by machine learning (ML) from the first-principles data, and hence can have an accuracy comparable with quantum mechanics.¹⁵³ However, care must be taken when applying these ML models to or developing new models for electrochemical system, which involves nonlocal and long-range charge transfer and electrostatics, as well as the effects of electrode potential. Efforts have been made to tackle the long-range electrostatics, despite the fact that they are demonstrated on simple systems.^{154,155} Also, as the structures and charge states dynamically evolve during the reaction, using a fixed ML model may not be optimal because the structures/charge states encountered during the simulation may be significantly different from those in the predefined training set. Thus, it is better to adopt the active (on-the-fly) learning strategy, which optimizes the model during the simulation using the encountered dissimilar data. Developing the proper ML force field and making the learning on-the-fly would provide a powerful tool to simulate the electrochemical interface.

It should be noted that there are different first-principles methods with different levels of accuracy. Some are not accurate enough to reproduce the experimental results of certain systems. For example, it is common to use DFT with semilocal approximations to the exchange correlation functional (e.g., PBE, rPBE, BEEF-vdW), while they incorrectly predict that the CO molecule prefers the hollow site on Cu(111) surface, contradicting the experimental finding that it prefers the atop site. Considering this inconsistency, Carter et al.¹⁵⁶ applied a more accurate first-principle method-embedded correlated wave function (ECW) theory, which reproduces the adsorption preference for CO to study the CO reduction to hydroxymethylidyne (*COH) and formyl (*CHO) on Cu(111). They found that the *CHO and *COH formation compete at -0.9 V vs the RHE, with very similar barriers (0.56 vs 0.58 eV). In contrast, semilocal DFT approximation predicts that *COH formation is a barrierless exothermic process and more favorable than *CHO formation (which has a barrier of 0.35 eV). On the other hand, the more accurate method is usually more computationally expensive and thus is limited to a small system, which can introduce other problems. Nevertheless, it is recommended to double check the results with different methods to make sure the conclusions are at least qualitatively robust.

Besides the common 2D electrocatalysts reviewed in this paper, some other 2D materials are occasionally reported as catalysts. For example, Mavrikakis and Xu et al.¹⁵⁷ synthesized free-standing monolayer and few-layer Bi and demonstrated its high electrocatalytic efficiency for CO₂R to formate. Sun and Xie et al.¹⁵⁸ showed that partially oxidized 4-layer Co has a high activity and selectivity toward formate production. For another example, dual-atoms embedded in (doped) graphene have

shown promising catalytic performance for various reactions.^{159–163} It is valuable to further explore the potential of these materials and discover new 2D electrocatalysts. Moreover, beyond the reactions discussed above where some 2D materials have been well established as electrocatalysts, other reactions can also be catalyzed by 2D materials. For example, the M–N–C is occasionally reported as catalyst for electrochemical ammonia synthesis: Ru,¹⁶⁴ Mo,¹⁶⁵ and Cu–N–C¹⁶⁶ can catalyze N₂ reduction to NH₃, and Fe–N–C can convert NO₃[−] to NH₃.¹⁶⁷ It is valuable to further explore the application of 2D materials for these reactions. First-principles studies will continue to play an important role in mechanistic understanding and catalyst design/discovery.

A good catalyst often desires strong bindings with certain intermediates but weak bindings with the others. Such optimization is difficult on catalyst with only one type of site due to the “scaling relation”. Thus, it is attractive to design more than one type of catalytic sites that can work synergistically. Besides the site engineering, modulating the local environment for reactions is another effective approach. For example, the cations in solution are known to significantly impact the CO₂R,^{168–170} and tuning them can suppress the HER and thus enable efficient CO₂R in acidic medium.¹⁷¹ For another example, OER of magnetic electrocatalysts (e.g., NiZnFe₄O_x, CoFe₂O₄) can be enhanced by external magnetic field.^{172,173} Considering that some 2D electrocatalysts also have intrinsic electron spin polarization,^{174,175} manipulating it by magnetic field may promote their catalytic performance as well.

Heterogeneous catalyst often has multiple possible site structures. To resolve the site-specific information, it is valuable to use model catalyst with well-defined structure to probe the structure–property relation. In addition to understanding the catalytic mechanism, it is also important to study the degradation mechanism as many of the nanoelectrocatalysts suffer from instability under working conditions. To make effective advances, it is critical to develop and apply computational methods with higher accuracy and efficiency, as well as experimental methods with higher spatial and temporal resolution/control, and to have closer collaboration between theory and experiment.

AUTHOR INFORMATION

Corresponding Author

Yuanyue Liu – Texas Materials Institute and Department of Mechanical Engineering, The University of Texas at Austin, Austin, Texas 78712, United States; orcid.org/0000-0002-5880-8649; Email: yuanyue.liu@austin.utexas.edu

Authors

Xunhua Zhao – Texas Materials Institute and Department of Mechanical Engineering, The University of Texas at Austin, Austin, Texas 78712, United States

Zachary H Levell – Texas Materials Institute and Department of Mechanical Engineering, The University of Texas at Austin, Austin, Texas 78712, United States

Saerom Yu – Texas Materials Institute and Department of Mechanical Engineering, The University of Texas at Austin, Austin, Texas 78712, United States

Complete contact information is available at:
<https://pubs.acs.org/10.1021/acs.chemrev.1c00981>

Notes

The authors declare no competing financial interest.

Biographies

Xunhua Zhao obtained his B.S. in Chemical Engineering from Zhejiang University in 2007, after which he worked in BASF-YPC Co., Ltd., for one year. He obtained his M.S. from the Graduate University of the Chinese Academy of Sciences in 2011, then he conducted Ph.D. studies at the Fritz-Haber Institute of Max Planck Society. After obtaining his Ph.D. degree in early 2016, he started his postdoctoral study at Princeton University and later the University of Texas at Austin.

Zachary H. Levell graduated from the University of Illinois at Urbana–Champaign with a B.S. in Materials Science and Engineering in 2020. He is currently a Ph.D. candidate in the Material Science and Engineering program at UT Austin.

Saerom Yu received her Bachelor's degree in Chemical Engineering from Soongsil University, South Korea. She then obtained a Master's degree in Energy at Texas A&M University. After her Master's study, she worked as a Research Intern at the Center for Hydrogen and Fuel Cell Research, Korea Institute of Science and Technology. Currently, she is pursuing a Ph.D. at UT Austin.

Yuanyue Liu is currently an assistant professor at the Department of Mechanical Engineering and Texas Materials Institute at the University of Texas at Austin. He received his B.S. degree from the University of Science and Technology of China (USTC) in 2008 and his Ph.D. from Rice University in 2014. He did postdoc studies at National Renewable Energy Laboratory (NREL) and the California Institute of Technology and then joined UT Austin in Fall, 2017.

ACKNOWLEDGMENTS

Y.L. acknowledges the support by The National Science Foundation (grant no. 1900039, 2029442), ACS PRF (60934-DNI6), and the Welch Foundation (grant no. F-1959-20210327).

REFERENCES

- (1) Li, G.; Chen, Z.; Li, Y.; Zhang, D.; Yang, W.; Liu, Y.; Cao, L. Engineering Substrate Interaction To Improve Hydrogen Evolution Catalysis of Monolayer MoS₂ Films beyond Pt. *ACS Nano* **2020**, *14* (2), 1707.
- (2) Liu, S.; Li, C.; Zachman, M. J.; Zeng, Y.; Yu, H.; Li, B.; Wang, M.; Braaten, J.; Liu, J.; Meyer, H. M., III; Lucero, M.; Kropf, A. J.; Gong, Q.; Shi, Q.; Feng, Z.; Wang, G.; Myers, D. J.; Xie, J.; Cullen, D. A.; Shawn, L.; Wu, G. Durable and High-Power Iron-Based Cathodes in Competition with Platinum for Proton-Exchange Membrane Fuel Cells. *ChemRxiv* **2021**, 2021-2qmbz, DOI: .
- (3) Kaiser, S. K.; Chen, Z.; Faust Akl, D.; Mitchell, S.; Perez-Ramirez, J. Single-Atom Catalysts across the Periodic Table. *Chem. Rev.* **2020**, *120*, 11703–11809.
- (4) Jin, H.; Guo, C.; Liu, X.; Liu, J.; Vasileff, A.; Jiao, Y.; Zheng, Y.; Qiao, S. Z. Emerging Two-Dimensional Nanomaterials for Electro-catalysis. *Chem. Rev.* **2018**, *118*, 6337–6408.
- (5) Zhao, C. X.; Li, B. Q.; Liu, J. N.; Zhang, Q. Intrinsic Electrocatalytic Activity Regulation of M-N-C Single-Atom Catalysts for the Oxygen Reduction Reaction. *Angew. Chem., Int. Ed.* **2021**, *60*, 4448–4463.
- (6) Voiry, D.; Shin, H. S.; Loh, K. P.; Chhowalla, M. Low-dimensional Catalysts for Hydrogen Evolution and CO₂ Reduction. *Nat. Rev. Chem.* **2018**, *2*, 0105.
- (7) Qu, Q.; Ji, S.; Chen, Y.; Wang, D.; Li, Y. The Atomic-level Regulation of Single-atom Site Catalysts for the Electrochemical CO₂ Reduction Reaction. *Chem. Sci.* **2021**, *12*, 4201–4215.
- (8) Andreoni, W.; Yip, S. *Handbook of Materials Modeling: Methods: Theory and Modeling*; Springer, 2019.

- (9) Nørskov, J. K.; Abild-Pedersen, F.; Studt, F.; Bligaard, T. Density Functional Theory in Surface Chemistry and Catalysis. *Proc. Natl. Acad. Sci. U. S. A.* **2011**, *108*, 937–943.

- (10) Zhao, X.; Shi, J.; Ji, Y.; Liu, Y. The Electronic Structure Underlying Electrocatalysis of Two-dimensional Materials. *Wiley Interdiscip. Rev. Comp. Mol. Sci.* **2019**, *9*, e1418.

- (11) Zhuo, H. Y.; Zhang, X.; Liang, J. X.; Yu, Q.; Xiao, H.; Li, J. Theoretical Understandings of Graphene-based Metal Single-Atom Catalysts: Stability and Catalytic Performance. *Chem. Rev.* **2020**, *120*, 12315–12341.

- (12) Nørskov, J. K.; Bligaard, T.; Logadottir, A.; Kitchin, J. R.; Chen, J. G.; Pandelov, S.; Stimming, U. Trends in the Exchange Current for Hydrogen Evolution. *J. Electrochem. Soc.* **2005**, *152*, J23–J26.

- (13) Trasatti, S. The Absolute Electrode Potential: an Explanatory Note (Recommendations 1986). *Pure Appl. Chem.* **1986**, *58*, 955–966.

- (14) Shi, J.; Zhao, X.; Wang, Z.; Liu, Y. Eliminating Trap-States and Functionalizing Vacancies in 2D Semiconductors by Electrochemistry. *Small* **2019**, *15* (47), 1901899.

- (15) Goodpaster, J. D.; Bell, A. T.; Head-Gordon, M. Identification of Possible Pathways for C–C Bond Formation during Electrochemical Reduction of CO₂: New Theoretical Insights from an Improved Electrochemical Model. *J. Phys. Chem. Lett.* **2016**, *7*, 1471–1477.

- (16) Sundararaman, R.; Goddard, W. A., III; Arias, T. A. Grand Canonical Electronic Density-functional theory: Algorithms and Applications to Electrochemistry. *J. Chem. Phys.* **2017**, *146*, 114104.

- (17) Yang, X.-H.; Zhuang, Y.-B.; Zhu, J.-X.; Le, J.-B.; Cheng, J. Recent Progress on Multiscale Modeling of Electrochemistry. *Wiley Interdiscip. Rev. Comp. Mol. Sci.* **2022**, *12*, e1559.

- (18) Otani, M.; Sugino, O. First-principles Calculations of Charged Surfaces and Interfaces: A Plane-wave Nonrepeated Slab Approach. *Phys. Rev. B* **2006**, *73*, 115407.

- (19) Ikeshoji, T.; Otani, M. Toward Full Simulation of the Electrochemical Oxygen Reduction Reaction on Pt using First-principles and Kinetic Calculations. *Phys. Chem. Chem. Phys.* **2017**, *19*, 4447–4453.

- (20) Nishihara, S.; Otani, M. Hybrid Solvation Models for Bulk, Interface, and Membrane: Reference Interaction Site Methods Coupled with Density Functional Theory. *Phys. Rev. B* **2017**, *96* (11), 115429.

- (21) Kastlunger, G.; Lindgren, P.; Peterson, A. A. Controlled-Potential Simulation of Elementary Electrochemical Reactions: Proton Discharge on Metal Surfaces. *J. Phys. Chem. C* **2018**, *122*, 12771–12781.

- (22) Surendralal, S.; Todorova, M.; Finnis, M. W.; Neugebauer, J. First-Principles Approach to Model Electrochemical Reactions: Understanding the Fundamental Mechanisms behind Mg Corrosion. *Phys. Rev. Lett.* **2018**, *120* (24), 246801.

- (23) Mathew, K.; Sundararaman, R.; Letchworth-Weaver, K.; Arias, T. A.; Hennig, R. G. Implicit Solvation Model for Density-functional Study of Nanocrystal Surfaces and Reaction Pathways. *J. Chem. Phys.* **2014**, *140*, No. 084106.

- (24) Mathew, K.; Kolluru, V. S. C.; Mula, S.; Steinmann, S. N.; Hennig, R. G. Implicit Self-consistent Electrolyte Model in Plane-wave Density-functional Theory. *J. Chem. Phys.* **2019**, *151* (23), 234101.

- (25) Mathew, K.; Kolluru, V. S. C.; Mula, S.; Steinmann, S. N.; Hennig, R. G. Implicit Self-consistent Electrolyte Model in Plane-wave Density-functional Theory. *J. Chem. Phys.* **2019**, *151*, No. 234101.

- (26) Sundararaman, R.; Letchworth-Weaver, K.; Schwarz, K. A.; Gunceler, D.; Ozhables, Y.; Arias, T. A. JDFTx: Software for Joint Density-functional Theory. *SoftwareX* **2017**, *6*, 278–284.

- (27) Hörmann, N. G.; Andreussi, O.; Marzari, N. Grand Canonical Simulations of Electrochemical Interfaces in Implicit Solvation Models. *J. Chem. Phys.* **2019**, *150*, No. 041730.

- (28) Taylor, C. D.; Wasileski, S. A.; Filhol, J.-S.; Neurock, M. First Principles Reaction Modeling of the Electrochemical Interface: Consideration and Calculation of a Tunable Surface Potential from Atomic and Electronic Structure. *Phys. Rev. B* **2006**, *73*, 165402.

- (29) Rossmeisl, J.; Skúlason, E.; Björketun, M. E.; Tripkovic, V.; Nørskov, J. K. Modeling the Electrified Solid–liquid Interface. *Chem. Phys. Lett.* **2008**, *466* (1), 68–71.

- (30) Chan, K.; Nørskov, J. K. Potential Dependence of Electrochemical Barriers from ab Initio Calculations. *Chem. Lett.* **2016**, *7*, 1686–1690.
- (31) Huang, Y.; Nielsen, R. J.; Goddard, W. A. Reaction Mechanism for the Hydrogen Evolution Reaction on the Basal Plane Sulfur Vacancy Site of MoS₂ Using Grand Canonical Potential Kinetics. *J. Am. Chem. Soc.* **2018**, *140* (48), 16773–16782.
- (32) Kim, D.; Shi, J.; Liu, Y. Substantial Impact of Charge on Electrochemical Reactions of Two-Dimensional Materials. *J. Am. Chem. Soc.* **2018**, *140*, 9127–9131.
- (33) Zhao, X.; Liu, Y. Unveiling the Active Structure of Single Nickel Atom Catalysis: Critical Roles of Charge Capacity and Hydrogen Bonding. *J. Am. Chem. Soc.* **2020**, *142* (12), 5773–5777.
- (34) Zhao, X.; Liu, Y. Origin of Selective Production of Hydrogen Peroxide by Electrochemical Oxygen Reduction. *J. Am. Chem. Soc.* **2021**, *143* (25), 9423–9428.
- (35) Heenen, H. H.; Gauthier, J. A.; Kristoffersen, H. H.; Ludwig, T.; Chan, K. Solvation at metal/water interfaces: An Ab Initio Molecular Dynamics Benchmark of Common Computational Approaches. *J. Chem. Phys.* **2020**, *152*, 144703.
- (36) Cao, H.; Xia, G.-J.; Chen, J.-W.; Yan, H.-M.; Huang, Z.; Wang, Y.-G. Mechanistic Insight into the Oxygen Reduction Reaction on the Mn–N₄/C Single-Atom Catalyst: The Role of the Solvent Environment. *J. Phys. Chem. C* **2020**, *124*, 7287–7294.
- (37) Ciccotti, G.; Ferrario, M. Blue Moon Approach to Rare Events. *Mol. Simul.* **2004**, *30* (11–12), 787–793.
- (38) Kästner, J. Umbrella Sampling. *Wiley Interd. Rev. Comp. Mol. Sci.* **2011**, *1*, 932–942.
- (39) Bussi, G.; Laio, A. Using Metadynamics to Explore Complex Free-energy Landscapes. *Nat. Rev. Phys.* **2020**, *2*, 200–212.
- (40) Sprik, M.; Ciccotti, G. Free Energy from Constrained Molecular Dynamics. *J. Chem. Phys.* **1998**, *109*, 7737–7744.
- (41) Jarzynski, C. Nonequilibrium equality for free energy differences. *Phys. Rev. Lett.* **1997**, *78*, 2690.
- (42) Bonnet, N.; Morishita, T.; Sugino, O.; Otani, M. First-Principles Molecular Dynamics at a Constant Electrode Potential. *Phys. Rev. Lett.* **2012**, *109*, 266101.
- (43) Hinnemann, B.; Moses, P. G.; Bonde, J.; Jørgensen, K. P.; Nielsen, J. H.; Horch, S.; Chorkendorff, I.; Nørskov, J. K. Biomimetic Hydrogen Evolution: MoS₂ Nanoparticles as Catalyst for Hydrogen Evolution. *J. Am. Chem. Soc.* **2005**, *127*, 5308–5309.
- (44) Jaramillo, T. F.; Jørgensen, K. P.; Bonde, J.; Nielsen, J. H.; Horch, S.; Chorkendorff, I. Identification of Active Edge Sites for Electrochemical H₂ Evolution from MoS₂ Nanocatalysts. *Science* **2007**, *317*, 100–102.
- (45) Huang, Y.; Nielsen, R. J.; Goddard, W. A.; Soriaga, M. P. The Reaction Mechanism with Free Energy Barriers for Electrochemical Dihydrogen Evolution on MoS₂. *J. Am. Chem. Soc.* **2015**, *137*, 6692–6698.
- (46) Tsai, C.; Chan, K.; Nørskov, J. K.; Abild-Pedersen, F. Understanding the Reactivity of Layered Transition-Metal Sulfides: A Single Electronic Descriptor for Structure and Adsorption. *J. Phys. Chem. Lett.* **2014**, *5*, 3884–3889.
- (47) Zhenbin, W.; Michael, T.; Ang, C.; Karen, C.; Jens Kehlet, N. Insights into Hydrogen Evolution Reaction on 2D Transition Metal Dichalcogenides. *ChemRxiv* **2021**, DOI: DOI: 10.26434/chemrxiv.14679084.v1.
- (48) Li, H.; Tsai, C.; Koh, A. L.; Cai, L.; Contryman, A. W.; Frapapan, A. H.; Zhao, J.; Han, H. S.; Manoharan, H. C.; Abild-Pedersen, F.; et al. Activating and Optimizing MoS₂ Basal Planes for Hydrogen Evolution through the Formation of Strained Sulphur Vacancies. *Nat. Mater.* **2016**, *15*, 48–53.
- (49) Li, H.; Du, M.; Mleczko, M. J.; Koh, A. L.; Nishi, Y.; Pop, E.; Bard, A. J.; Zheng, X. Kinetic Study of Hydrogen Evolution Reaction over Strained MoS₂ with Sulfur Vacancies Using Scanning Electrochemical Microscopy. *J. Am. Chem. Soc.* **2016**, *138*, 5123–5129.
- (50) Li, G.; Zhang, D.; Qiao, Q.; Yu, Y.; Peterson, D.; Zafar, A.; Kumar, R.; Curtarolo, S.; Hunte, F.; Shannon, S.; et al. All The Catalytic Active Sites of MoS₂ for Hydrogen Evolution. *J. Am. Chem. Soc.* **2016**, *138*, 16632–16638.
- (51) Zhu, J.; Wang, Z.-C.; Dai, H.; Wang, Q.; Yang, R.; Yu, H.; Liao, M.; Zhang, J.; Chen, W.; Wei, Z.; et al. Boundary Activated Hydrogen Evolution Reaction on Monolayer MoS₂. *Nat. Commun.* **2019**, *10*, 1348.
- (52) He, Y.; Tang, P.; Hu, Z.; He, Q.; Zhu, C.; Wang, L.; Zeng, Q.; Golani, P.; Gao, G.; Fu, W.; et al. Engineering Grain boundaries at the 2D Limit for the Hydrogen Evolution Reaction. *Nat. Commun.* **2020**, *11*, 57.
- (53) Ouyang, Y.; Ling, C.; Chen, Q.; Wang, Z.; Shi, L.; Wang, J. Activating Inert Basal Planes of MoS₂ for Hydrogen Evolution Reaction through the Formation of Different Intrinsic Defects. *Chem. Mater.* **2016**, *28*, 4390–4396.
- (54) Deng, J.; Li, H.; Xiao, J.; Tu, Y.; Deng, D.; Yang, H.; Tian, H.; Li, J.; Ren, P.; Bao, X. Triggering the Electrocatalytic Hydrogen Evolution Activity of the Inert Two-dimensional MoS₂ Surface via Single-atom Metal Doping. *Energy Environ. Sci.* **2015**, *8*, 1594–1601.
- (55) Voiry, D.; Salehi, M.; Silva, R.; Fujita, T.; Chen, M.; Asefa, T.; Shenoy, V. B.; Eda, G.; Chhowalla, M. Conducting MoS₂ Nanosheets as Catalysts for Hydrogen Evolution Reaction. *Nano Lett.* **2013**, *13* (12), 6222–6227.
- (56) Yin, Y.; Han, J.; Zhang, Y.; Zhang, X.; Xu, P.; Yuan, Q.; Samad, L.; Wang, X.; Wang, Y.; Zhang, Z.; et al. Contributions of Phase, Sulfur Vacancies, and Edges to the Hydrogen Evolution Reaction Catalytic Activity of Porous Molybdenum Disulfide Nanosheets. *J. Am. Chem. Soc.* **2016**, *138*, 7965–7972.
- (57) Geng, X.; Sun, W.; Wu, W.; Chen, B.; Al-Hilo, A.; Benamara, M.; Zhu, H.; Watanabe, F.; Cui, J.; Chen, T.-p. Pure and Stable Metallic Phase Molybdenum Disulfide Nanosheets for Hydrogen Evolution Reaction. *Nat. Commun.* **2016**, *7*, 10672.
- (58) Tang, Q.; Jiang, D.-e. Mechanism of Hydrogen Evolution Reaction on 1T-MoS₂ from First Principles. *ACS Catal.* **2016**, *6* (8), 4953–4961.
- (59) Voiry, D.; Yamaguchi, H.; Li, J.; Silva, R.; Alves, D. C. B.; Fujita, T.; Chen, M.; Asefa, T.; Shenoy, V. B.; Eda, G.; et al. Enhanced Catalytic Activity in Strained Chemically Exfoliated WS₂ Nanosheets for Hydrogen Evolution. *Nat. Mater.* **2013**, *12* (9), 850–855.
- (60) Ping, X.; Liang, D.; Wu, Y.; Yan, X.; Zhou, S.; Hu, D.; Pan, X.; Lu, P.; Jiao, L. Activating a Two-Dimensional PtSe₂ Basal Plane for the Hydrogen Evolution Reaction through the Simultaneous Generation of Atomic Vacancies and Pt Clusters. *Nano Lett.* **2021**, *21*, 3857–3863.
- (61) Liu, Y.; Wu, J.; Hackenberg, K. P.; Zhang, J.; Wang, Y. M.; Yang, Y.; Keyshar, K.; Gu, J.; Ogitsu, T.; Vajtai, R. et al. Self-optimizing Layered Hydrogen Evolution Catalyst with High Basal-plane Activity. *arXiv* **2016**, 1608.05755
- (62) Liu, Y.; Wu, J.; Hackenberg, K. P.; Zhang, J.; Wang, Y. M.; Yang, Y.; Keyshar, K.; Gu, J.; Ogitsu, T.; Vajtai, R.; et al. Self-optimizing, Highly Surface-active Layered Metal Dichalcogenide Catalysts for hydrogen evolution. *Nat. Energy* **2017**, *2*, 17127.
- (63) McGlynn, J. C.; Dankwort, T.; Kienle, L.; Bandeira, N. A. G.; Fraser, J. P.; Gibson, E. K.; Cascallana-Matias, I.; Kamarás, K.; Symes, M. D.; Miras, H. N.; et al. The Rapid Electrochemical Activation of MoTe₂ for the Hydrogen Evolution Reaction. *Nat. Commun.* **2019**, *10*, 4916.
- (64) Li, X.; Fang, Y.; Wang, J.; Fang, H.; Xi, S.; Zhao, X.; Xu, D.; Xu, H.; Yu, W.; Hai, X.; et al. Ordered Clustering of Single Atomic Te Vacancies in Atomically Thin PtTe₂ Promotes Hydrogen Evolution Catalysis. *Nat. Commun.* **2021**, *12*, 2351.
- (65) Lindgren, P.; Kastlunger, G.; Peterson, A. A. A Challenge to the G ~ 0 Interpretation of Hydrogen Evolution. *ACS Catal.* **2020**, *10* (1), 121–128.
- (66) Zhao, X.; Liu, Y. Unveiling the Active Structure of Single Nickel Atom Catalysis: Critical Roles of Charge Capacity and Hydrogen Bonding. *J. Am. Chem. Soc.* **2020**, *142* (12), 5773–5777.
- (67) Jiao, Y.; Zheng, Y.; Davey, K.; Qiao, S.-Z. Activity Origin and Catalyst Design Principles for Electrocatalytic Hydrogen Evolution on Heteroatom-doped Graphene. *Nat. Energy* **2016**, *1*, 16130.

- (68) Cheng, N.; Stambula, S.; Wang, D.; Banis, M. N.; Liu, J.; Riese, A.; Xiao, B.; Li, R.; Sham, T.-K.; Liu, L.-M.; et al. Platinum Single-atom and Cluster Catalysis of the Hydrogen Evolution Reaction. *Nat. Commun.* **2016**, *7*, 13638.
- (69) Fei, H.; Dong, J.; Arellano-Jiménez, M. J.; Ye, G.; Dong Kim, N.; Samuel, E. L. G.; Peng, Z.; Zhu, Z.; Qin, F.; Bao, J.; et al. Atomic Cobalt on Nitrogen-doped Graphene for Hydrogen Generation. *Nat. Commun.* **2015**, *6* (1), 8668.
- (70) Chen, W.; Pei, J.; He, C.-T.; Wan, J.; Ren, H.; Zhu, Y.; Wang, Y.; Dong, J.; Tian, S.; Cheong, W.-C.; et al. Rational Design of Single Molybdenum Atoms Anchored on N-Doped Carbon for Effective Hydrogen Evolution Reaction. *Angew. Chem., Int. Ed.* **2017**, *56*, 16086–16090.
- (71) Chen, W.; Pei, J.; He, C.-T.; Wan, J.; Ren, H.; Wang, Y.; Dong, J.; Wu, K.; Cheong, W.-C.; Mao, J.; et al. Single Tungsten Atoms Supported on MOF-Derived N-Doped Carbon for Robust Electrochemical Hydrogen Evolution. *Adv. Mater.* **2018**, *30*, 1800396.
- (72) Fan, L.; Liu, P. F.; Yan, X.; Gu, L.; Yang, Z. Z.; Yang, H. G.; Qiu, S.; Yao, X. Atomically Isolated Nickel Species Anchored on Graphitized Carbon for Efficient Hydrogen Evolution Electrocatalysis. *Nat. Commun.* **2016**, *7*, 10667.
- (73) Zhang, L.; Jia, Y.; Gao, G.; Yan, X.; Chen, N.; Chen, J.; Soo, M. T.; Wood, B.; Yang, D.; Du, A.; et al. Graphene Defects Trap Atomic Ni Species for Hydrogen and Oxygen Evolution Reactions. *Chem.* **2018**, *4* (2), 285–297.
- (74) Xu, H.; Cheng, D.; Cao, D.; Zeng, X. C. A Universal Principle for a Rational Design of Single-atom Electrocatalysts. *Nat. Catal.* **2018**, *1* (5), 339–348.
- (75) Fei, H.; Dong, J.; Feng, Y.; Allen, C. S.; Wan, C.; Voloskiy, B.; Li, M.; Zhao, Z.; Wang, Y.; Sun, H.; et al. General Synthesis and Definitive Structural Identification of MN₄C₄ Single-atom Catalysts with Tunable Electrocatalytic Activities. *Nat. Catal.* **2018**, *1* (1), 63–72.
- (76) Li, Y.; Wu, Z.-S.; Lu, P.; Wang, X.; Liu, W.; Liu, Z.; Ma, J.; Ren, W.; Jiang, Z.; Bao, X. High-Valence Nickel Single-Atom Catalysts Coordinated to Oxygen Sites for Extraordinarily Activating Oxygen Evolution Reaction. *Adv. Sci.* **2020**, *7* (5), 1903089.
- (77) Liu, X.; Dai, L. Carbon-based Metal-free Catalysts. *Nat. Rev. Mater.* **2016**, *1*, 16064.
- (78) Zhao, Y.; Nakamura, R.; Kamiya, K.; Nakanishi, S.; Hashimoto, K. Nitrogen-doped Carbon Nanomaterials as Non-metal Electrocatalysts for Water Oxidation. *Nat. Commun.* **2013**, *4* (1), 2390.
- (79) Li, M.; Zhang, L.; Xu, Q.; Niu, J.; Xia, Z. N-doped Graphene as Catalysts for Oxygen Reduction and Oxygen Evolution Reactions: Theoretical Considerations. *J. Catal.* **2014**, *314*, 66–72.
- (80) Yang, H. B.; Miao, J.; Hung, S.-F.; Chen, J.; Tao, H. B.; Wang, X.; Zhang, L.; Chen, R.; Gao, J.; Chen, H. M.; et al. Identification of Catalytic Sites for Oxygen Reduction and Oxygen Evolution in N-doped Graphene Materials: Development of Highly Efficient Metal-free Bifunctional Electrocatalyst. *Sci. Adv.* **2016**, *2*, e1501122.
- (81) Dionigi, F.; Zeng, Z.; Sinev, I.; Merzdorf, T.; Deshpande, S.; Lopez, M. B.; Kunze, S.; Zegkinoglou, I.; Sarodnik, H.; Fan, D.; et al. In-situ Structure and Catalytic Mechanism of NiFe and CoFe Layered Double Hydroxides during Oxygen Evolution. *Nat. Commun.* **2020**, *11*, 2522.
- (82) Song, F.; Hu, X. Exfoliation of Layered Double Hydroxides for Enhanced Oxygen Evolution Catalysis. *Nat. Commun.* **2014**, *5* (1), 4477.
- (83) Chen, R.; Hung, S.-F.; Zhou, D.; Gao, J.; Yang, C.; Tao, H.; Yang, H. B.; Zhang, L.; Zhang, L.; Xiong, Q.; et al. Layered Structure Causes Bulk NiFe Layered Double Hydroxide Unstable in Alkaline Oxygen Evolution Reaction. *Adv. Mater.* **2019**, *31* (41), 1903909.
- (84) Kang, J.; Qiu, X.; Hu, Q.; Zhong, J.; Gao, X.; Huang, R.; Wan, C.; Liu, L.-M.; Duan, X.; Guo, L. Valence Oscillation and Dynamic Active Sites in Monolayer NiCo Hydroxides for Water Oxidation. *Nat. Catal.* **2021**, *4* (12), 1050–1058.
- (85) Mefford, J. T.; Akbashev, A. R.; Kang, M.; Bentley, C. L.; Gent, W. E.; Deng, H. D.; Alsem, D. H.; Yu, Y.-S.; Salmon, N. J.; Shapiro, D. A.; et al. Correlative Operando Microscopy of Oxygen Evolution Electrocatalysts. *Nature* **2021**, *593* (7857), 67–73.
- (86) Xiao, H.; Shin, H.; Goddard, W. A. Synergy between Fe and Ni in the Optimal Performance of (Ni,Fe)OOH Catalysts for the Oxygen Evolution Reaction. *Proc. Nat. Acad. Sci. U. S. A.* **2018**, *115*, 5872–5877.
- (87) Ling, C.; Shi, L.; Ouyang, Y.; Zeng, X. C.; Wang, J. Nanosheet Supported Single-Metal Atom Bifunctional Catalyst for Overall Water Splitting. *Nano Lett.* **2017**, *17* (8), 5133–5139.
- (88) Zheng, Y.; Jiao, Y.; Zhu, Y.; Cai, Q.; Vasileff, A.; Li, L. H.; Han, Y.; Chen, Y.; Qiao, S.-Z. Molecule-Level g-C₃N₄ Coordinated Transition Metals as a New Class of Electrocatalysts for Oxygen Electrode Reactions. *J. Am. Chem. Soc.* **2017**, *139*, 3336–3339.
- (89) Chai, G.-L.; Hou, Z.; Shu, D.-J.; Ikeda, T.; Terakura, K. Active Sites and Mechanisms for Oxygen Reduction Reaction on Nitrogen-Doped Carbon Alloy Catalysts: Stone–Wales Defect and Curvature Effect. *J. Am. Chem. Soc.* **2014**, *136*, 13629–13640.
- (90) Duan, Z.; Henkelman, G. Identification of Active Sites of Pure and Nitrogen-Doped Carbon Materials for Oxygen Reduction Reaction Using Constant-Potential Calculations. *J. Phys. Chem. C* **2020**, *124* (22), 12016–12023.
- (91) Guo, D.; Shibuya, R.; Akiba, C.; Saji, S.; Kondo, T.; Nakamura, J. Active Sites of Nitrogen-doped Carbon Materials for Oxygen Reduction Reaction Clarified using Model Catalysts. *Science* **2016**, *351* (6271), 361–365.
- (92) Wang, T.; Chen, Z.-X.; Chen, Y.-G.; Yang, L.-J.; Yang, X.-D.; Ye, J.-Y.; Xia, H.-P.; Zhou, Z.-Y.; Sun, S.-G. Identifying the Active Site of N-Doped Graphene for Oxygen Reduction by Selective Chemical Modification. *ACS Energy Lett.* **2018**, *3*, 986–991.
- (93) Jia, Y.; Zhang, L.; Zhuang, L.; Liu, H.; Yan, X.; Wang, X.; Liu, J.; Wang, J.; Zheng, Y.; Xiao, Z.; et al. Identification of Active Sites for Acidic Oxygen Reduction on Carbon Catalysts with and without Nitrogen Doping. *Nat. Catal.* **2019**, *2*, 688–695.
- (94) Choi, C. H.; Lim, H.-K.; Chung, M. W.; Park, J. C.; Shin, H.; Kim, H.; Woo, S. I. Long-Range Electron Transfer over Graphene-Based Catalyst for High-Performing Oxygen Reduction Reactions: Importance of Size, N-doping, and Metallic Impurities. *J. Am. Chem. Soc.* **2014**, *136*, 9070–9077.
- (95) Yang, Z.; Yao, Z.; Li, G.; Fang, G.; Nie, H.; Liu, Z.; Zhou, X.; Chen, X. a.; Huang, S. Sulfur-doped Graphene as an Efficient Metal-free Cathode Catalyst for Oxygen Reduction. *ACS Nano* **2012**, *6* (1), 205–211.
- (96) Zhang, C.; Mahmood, N.; Yin, H.; Liu, F.; Hou, Y. Synthesis of Phosphorus-doped Graphene and Its Multifunctional Applications for Oxygen Reduction Reaction and Lithium Ion Batteries. *Adv. Mater.* **2013**, *25* (35), 4932–4937.
- (97) Fazio, G.; Ferrighi, L.; Di Valentin, C. Boron-doped Graphene as Active Electrocatalyst for Oxygen Reduction Reaction at a Fuel-cell Cathode. *J. Catal.* **2014**, *318*, 203–210.
- (98) Jiao, Y.; Zheng, Y.; Jaroniec, M.; Qiao, S. Z. Origin of the Electrocatalytic Oxygen Reduction Activity of Graphene-Based Catalysts: A Roadmap to Achieve the Best Performance. *J. Am. Chem. Soc.* **2014**, *136*, 4394–4403.
- (99) Li, J.; Sougrati, M. T.; Zitolo, A.; Ablett, J. M.; Oğuz, I. C.; Mineva, T.; Matanovic, I.; Atanassov, P.; Huang, Y.; Zhenyuk, I.; et al. Identification of Durable and Non-durable FeN_x sites in Fe–N–C Materials for Proton Exchange Membrane Fuel Cells. *Nat. Catal.* **2021**, *4* (1), 10.
- (100) Mineva, T.; Matanovic, I.; Atanassov, P.; Sougrati, M.-T.; Stievano, L.; Clémancey, M.; Kochem, A.; Latour, J.-M.; Jaouen, F. Understanding Active Sites in Pyrolyzed Fe–N–C Catalysts for Fuel Cell Cathodes by Bridging Density Functional Theory Calculations and 57Fe Mössbauer Spectroscopy. *ACS Catal.* **2019**, *9*, 9359–9371.
- (101) Liu, K.; Wu, G.; Wang, G. Role of Local Carbon Structure Surrounding FeN₄ Sites in Boosting the Catalytic Activity for Oxygen Reduction. *J. Phys. Chem. C* **2017**, *121*, 11319–11324.
- (102) Zhong, L.; Li, S. Unconventional Oxygen Reduction Reaction Mechanism and Scaling Relation on Single-Atom Catalysts. *ACS Catal.* **2020**, *10*, 4313–4318.
- (103) Wang, Y.; Tang, Y.-J.; Zhou, K. Self-Adjusting Activity Induced by Intrinsic Reaction Intermediate in Fe–N–C Single-Atom Catalysts. *J. Am. Chem. Soc.* **2019**, *141*, 14115–14119.

- (104) Li, J.; Ghoshal, S.; Liang, W.; Sougrati, M.-T.; Jaouen, F.; Halevi, B.; McKinney, S.; McCool, G.; Ma, C.; Yuan, X.; et al. Structural and Mechanistic Basis for the High Activity of Fe–N–C Catalysts toward Oxygen Reduction. *Energy Environ. Sci.* **2016**, *9*, 2418–2432.
- (105) Jia, Q.; Ramaswamy, N.; Hafiz, H.; Tylus, U.; Strickland, K.; Wu, G.; Barbiellini, B.; Bansil, A.; Holby, E. F.; Zelenay, P.; et al. Experimental Observation of Redox-Induced Fe–N Switching Behavior as a Determinant Role for Oxygen Reduction Activity. *ACS Nano* **2015**, *9* (12), 12496–12505.
- (106) Jin, Z.; Li, P.; Meng, Y.; Fang, Z.; Xiao, D.; Yu, G. Understanding the Inter-site Distance Effect in Single-atom Catalysts for Oxygen Electroreduction. *Nat. Catal.* **2021**, *4*, 615–622.
- (107) Jiao, L.; Li, J.; Richard, L. L.; Sun, Q.; Stracensky, T.; Liu, E.; Sougrati, M. T.; Zhao, Z.; Yang, F.; Zhong, S.; et al. Chemical Vapour Deposition of Fe–N–C Oxygen Reduction Catalysts with Full Utilization of Dense Fe–N4 Sites. *Nat. Mater.* **2021**, *20*, 1385–1391.
- (108) Li, J.; Chen, M.; Cullen, D. A.; Hwang, S.; Wang, M.; Li, B.; Liu, K.; Karakalos, S.; Lucero, M.; Zhang, H.; et al. Atomically Dispersed Manganese Catalysts for Oxygen Reduction in Proton-exchange Membrane Fuel Cells. *Nat. Catal.* **2018**, *1*, 935–945.
- (109) Xie, X.; He, C.; Li, B.; He, Y.; Cullen, D. A.; Wegener, E. C.; Kropf, A. J.; Martinez, U.; Cheng, Y.; Engelhard, M. H.; et al. Performance Enhancement and Degradation Mechanism Identification of a Single-atom Co–N–C Catalyst for Proton Exchange Membrane Fuel Cells. *Nat. Catal.* **2020**, *3*, 1044–1054.
- (110) Sun, Y.; Silvioli, L.; Sahraie, N. R.; Ju, W.; Li, J.; Zitolo, A.; Li, S.; Bagger, A.; Arnarson, L.; Wang, X.; et al. Activity–Selectivity Trends in the Electrochemical Production of Hydrogen Peroxide over Single-Site Metal–Nitrogen–Carbon Catalysts. *J. Am. Chem. Soc.* **2019**, *141*, 12372–12381.
- (111) Zhao, X.; Liu, Y. Origin of Selective Production of Hydrogen Peroxide by Electrochemical Oxygen Reduction. *J. Am. Chem. Soc.* **2021**, *143*, 9423–9428.
- (112) Gao, J.; Yang, H. b.; Huang, X.; Hung, S.-F.; Cai, W.; Jia, C.; Miao, S.; Chen, H. M.; Yang, X.; Huang, Y.; et al. Enabling Direct H₂O₂ Production in Acidic Media through Rational Design of Transition Metal Single Atom Catalyst. *Chem.* **2020**, *6* (3), 658–674.
- (113) Liu, C.; Li, H.; Liu, F.; Chen, J.; Yu, Z.; Yuan, Z.; Wang, C.; Zheng, H.; Henkelman, G.; Wei, L.; et al. Intrinsic Activity of Metal Centers in Metal-Nitrogen-Carbon Single-Atom Catalysts for Hydrogen Peroxide Synthesis. *J. Am. Chem. Soc.* **2020**, *142* (52), 21861–21871.
- (114) Jung, E.; Shin, H.; Lee, B.-H.; Efremov, V.; Lee, S.; Lee, H. S.; Kim, J.; Hooch Antink, W.; Park, S.; Lee, K.-S.; et al. Atomic-level Tuning of Co–N–C Catalyst for High-performance Electrochemical H₂O₂ Production. *Nat. Mater.* **2020**, *19* (4), 436–442.
- (115) Zhang, Q.; Tan, X.; Bedford, N. M.; Han, Z.; Thomsen, L.; Smith, S.; Amal, R.; Lu, X. Direct Insights into the Role of Epoxy Groups on Cobalt Sites for Acidic H₂O₂ Production. *Nat. Commun.* **2020**, *11*, 4181.
- (116) Tang, C.; Chen, L.; Li, H.; Li, L.; Jiao, Y.; Zheng, Y.; Xu, H.; Davey, K.; Qiao, S. Z. Tailoring Acidic Oxygen Reduction Selectivity on Single-Atom Catalysts via Modification of First and Second Coordination Spheres. *J. Am. Chem. Soc.* **2021**, *143*, 7819–7827.
- (117) Yang, Q.; Xu, W.; Gong, S.; Zheng, G.; Tian, Z.; Wen, Y.; Peng, L.; Zhang, L.; Lu, Z.; Chen, L. Atomically Dispersed Lewis Acid Sites Boost 2-electron Oxygen Reduction Activity of Carbon-based Catalysts. *Nat. Commun.* **2020**, *11*, 5478.
- (118) Jiang, K.; Back, S.; Akey, A. J.; Xia, C.; Hu, Y.; Liang, W.; Schaak, D.; Stavitski, E.; Norskov, J. K.; Siahrostami, S.; et al. Highly Selective Oxygen Reduction to Hydrogen Peroxide on Transition Metal Single Atom Coordination. *Nat. Commun.* **2019**, *10*, 3997.
- (119) Wang, Y.; Shi, R.; Shang, L.; Waterhouse, G. I. N.; Zhao, J.; Zhang, Q.; Gu, L.; Zhang, T. High-Efficiency Oxygen Reduction to Hydrogen Peroxide Catalyzed by Nickel Single-Atom Catalysts with Tetradentate N₂O₂ Coordination in a Three-Phase Flow Cell. *Angew. Chem., Int. Ed.* **2020**, *59*, 13057–13062.
- (120) Tang, C.; Jiao, Y.; Shi, B.; Liu, J.-N.; Xie, Z.; Chen, X.; Zhang, Q.; Qiao, S.-Z. Coordination Tunes Selectivity: Two-Electron Oxygen Reduction on High-Loading Molybdenum Single-Atom Catalysts. *Angew. Chem., Int. Ed.* **2020**, *59*, 9171–9176.
- (121) Sun, Y.; Silvioli, L.; Sahraie, N. R.; Ju, W.; Li, J.; Zitolo, A.; Li, S.; Bagger, A.; Arnarson, L.; Wang, X.; et al. Activity–Selectivity Trends in the Electrochemical Production of Hydrogen Peroxide over Single-Site Metal–Nitrogen–Carbon Catalysts. *J. Am. Chem. Soc.* **2019**, *141*, 12372–12381.
- (122) Xia, Y.; Zhao, X.; Xia, C.; Wu, Z. Y.; Zhu, P.; Kim, J. Y. T.; Bai, X.; Gao, G.; Hu, Y.; Zhong, J.; et al. Highly Active and Selective Oxygen Reduction to H₂O₂ on Boron-doped Carbon for High Production Rates. *Nat. Commun.* **2021**, *12*, 4225.
- (123) Lu, Z.; Chen, G.; Siahrostami, S.; Chen, Z.; Liu, K.; Xie, J.; Liao, L.; Wu, T.; Lin, D.; Liu, Y.; et al. High-efficiency Oxygen Reduction to Hydrogen Peroxide Catalysed by Oxidized Carbon Materials. *Nat. Catal.* **2018**, *1* (2), 156.
- (124) Kim, H. W.; Ross, M. B.; Kornienko, N.; Zhang, L.; Guo, J.; Yang, P.; McCloskey, B. D. Efficient Hydrogen Peroxide Generation using Reduced Graphene Oxide-based Oxygen Reduction Electrocatalysts. *Nat. Catal.* **2018**, *1* (4), 282.
- (125) Sa, Y. J.; Kim, J. H.; Joo, S. H. Active Edge-Site-Rich Carbon Nanocatalysts with Enhanced Electron Transfer for Efficient Electrochemical Hydrogen Peroxide Production. *Angew. Chem., Int. Ed.* **2019**, *58*, 1100–1105.
- (126) Han, G. F.; Li, F.; Zou, W.; Karamad, M.; Jeon, J. P.; Kim, S. W.; Kim, S. J.; Bu, Y.; Fu, Z.; Lu, Y.; et al. Building and Identifying Highly Active Oxygenated Groups in Carbon Materials for Oxygen Reduction to H₂O₂. *Nat. Commun.* **2020**, *11*, 2209.
- (127) Čolić, V.; Yang, S.; Révay, Z.; Stephens, I. E. L.; Chorkendorff, I. Carbon Catalysts for Electrochemical Hydrogen Peroxide Production in Acidic Media. *Electrochim. Acta* **2018**, *272*, 192–202.
- (128) Ju, W.; Bagger, A.; Hao, G. P.; Varela, A. S.; Sinev, I.; Bon, V.; Roldan Cuenya, B.; Kaskel, S.; Rossmel, J.; Strasser, P. Understanding Activity and Selectivity of Metal-nitrogen-doped Carbon Catalysts for Electrochemical Reduction of CO₂. *Nat. Commun.* **2017**, *8*, 944.
- (129) Karapinar, D.; Huan, N. T.; Ranjbar Sahraie, N.; Li, J.; Wakerley, D.; Touati, N.; Zanna, S.; Taverna, D.; Galvao Tizei, L. H.; Zitolo, A.; et al. Electroreduction of CO₂ on Single-Site Copper-Nitrogen-Doped Carbon Material: Selective Formation of Ethanol and Reversible Restructuration of the Metal Sites. *Angew. Chem., Int. Ed.* **2019**, *58*, 15098–15103.
- (130) Jiang, K.; Siahrostami, S.; Akey, A. J.; Li, Y.; Lu, Z.; Lattimer, J.; Hu, Y.; Stokes, C.; Gangishetty, M.; Chen, G.; et al. Transition-Metal Single Atoms in a Graphene Shell as Active Centers for Highly Efficient Artificial Photosynthesis. *Chem.* **2017**, *3* (6), 950–960.
- (131) Li, X.; Bi, W.; Chen, M.; Sun, Y.; Ju, H.; Yan, W.; Zhu, J.; Wu, X.; Chu, W.; Wu, C.; et al. Exclusive Ni–N₄ Sites Realize Near-Unity CO Selectivity for Electrochemical CO₂ Reduction. *J. Am. Chem. Soc.* **2017**, *139*, 14889–14892.
- (132) Yang, H. B.; Hung, S.-F.; Liu, S.; Yuan, K.; Miao, S.; Zhang, L.; Huang, X.; Wang, H.-Y.; Cai, W.; Chen, R.; et al. Atomically Dispersed Ni(i) as the Active Site for Electrochemical CO₂ Reduction. *Nat. Energy* **2018**, *3* (2), 140–147.
- (133) Liu, S.; Yang, H. B.; Hung, S. F.; Ding, J.; Cai, W.; Liu, L.; Gao, J.; Li, X.; Ren, X.; Kuang, Z.; et al. Elucidating the Electrocatalytic CO₂ Reduction Reaction over a Model Single-Atom Nickel Catalyst. *Angew. Chem., Int. Ed.* **2020**, *59*, 798–803.
- (134) Hossain, M. D.; Huang, Y.; Yu, T. H.; Goddard, W. A., III; Luo, Z. Reaction Mechanism and Kinetics for CO₂ Reduction on Nickel Single Atom Catalysts from Quantum Mechanics. *Nat. Commun.* **2020**, *11*, 2256.
- (135) Qin, X.; Zhu, S.; Xiao, F.; Zhang, L.; Shao, M. Active Sites on Heterogeneous Single-Iron-Atom Electrocatalysts in CO₂ Reduction Reaction. *ACS Energy Lett.* **2019**, *4*, 1778–1783.
- (136) Chen, Z.; Huang, A.; Yu, K.; Cui, T.; Zhuang, Z.; Liu, S.; Li, J.; Tu, R.; Sun, K.; Tan, X.; et al. Fe1N4–O1 Site with Axial Fe–O Coordination for Highly Selective CO₂ Reduction over a Wide Potential Range. *Energy Environ. Sci.* **2021**, *14*, 3430–3437.
- (137) Zu, X.; Li, X.; Liu, W.; Sun, Y.; Xu, J.; Yao, T.; Yan, W.; Gao, S.; Wang, C.; Wei, S.; et al. Efficient and Robust Carbon Dioxide

Electroreduction Enabled by Atomically Dispersed Sn(δ) (+) Sites. *Adv. Mater.* **2019**, *31*, 1808135.

(138) Yang, H.; Wu, Y.; Li, G.; Lin, Q.; Hu, Q.; Zhang, Q.; Liu, J.; He, C. Scalable Production of Efficient Single-Atom Copper Decorated Carbon Membranes for CO₂ Electroreduction to Methanol. *J. Am. Chem. Soc.* **2019**, *141*, 12717–12723.

(139) Cai, Y.; Fu, J.; Zhou, Y.; Chang, Y. C.; Min, Q.; Zhu, J. J.; Lin, Y.; Zhu, W. Insights on forming N,O- Coordinated Cu Single-atom Catalysts for Electrochemical Reduction CO₂ to Methane. *Nat. Commun.* **2021**, *12*, 586.

(140) Vijay, S.; Ju, W.; Brückner, S.; Tsang, S.-C.; Strasser, P.; Chan, K. Unified Mechanistic Understanding of CO₂ Reduction to CO on Transition Metal and Single Atom Catalysts. *Nat. Catal.* **2021**, *4*, 1024–1031.

(141) Wu, J.; Sharifi, T.; Gao, Y.; Zhang, T.; Ajayan, P. M. Emerging Carbon-Based Heterogeneous Catalysts for Electrochemical Reduction of Carbon Dioxide into Value-Added Chemicals. *Adv. Mater.* **2019**, *31* (13), 1804257.

(142) Wu, J.; Liu, M.; Sharma, P. P.; Yadav, R. M.; Ma, L.; Yang, Y.; Zou, X.; Zhou, X. D.; Vajtai, R.; Yakobson, B. I.; et al. Incorporation of Nitrogen Defects for Efficient Reduction of CO₂ via Two-Electron Pathway on Three-Dimensional Graphene Foam. *Nano Lett.* **2016**, *16* (1), 466–470.

(143) Siahrostami, S.; Jiang, K.; Karamad, M.; Chan, K.; Wang, H.; Nørskov, J. Theoretical Investigations into Defected Graphene for Electrochemical Reduction of CO₂. *ACS Sustain. Chem. Eng.* **2017**, *5*, 11080–11085.

(144) Wu, J.; Ma, S.; Sun, J.; Gold, J. I.; Tiwary, C.; Kim, B.; Zhu, L.; Chopra, N.; Odeh, I. N.; Vajtai, R.; et al. A Metal-free Electrocatalyst for Carbon Dioxide Reduction to Multi-carbon Hydrocarbons and Oxygenates. *Nat. Commun.* **2016**, *7*, 13869.

(145) Zou, X.; Liu, M.; Wu, J.; Ajayan, P. M.; Li, J.; Liu, B.; Yakobson, B. I. How Nitrogen-Doped Graphene Quantum Dots Catalyze Electroreduction of CO₂ to Hydrocarbons and Oxygenates. *ACS Catal.* **2017**, *7* (9), 6245–6250.

(146) Landers, A. T.; Fields, M.; Torelli, D. A.; Xiao, J.; Hellstern, T. R.; Francis, S. A.; Tsai, C.; Kibsgaard, J.; Lewis, N. S.; Chan, K.; et al. The Predominance of Hydrogen Evolution on Transition Metal Sulfides and Phosphides under CO₂ Reduction Conditions: An Experimental and Theoretical Study. *ACS Energy Lett.* **2018**, *3*, 1450–1457.

(147) Asadi, M.; Kumar, B.; Behranginia, A.; Rosen, B. A.; Baskin, A.; Repnin, N.; Pisasale, D.; Phillips, P.; Zhu, W.; Haasch, R.; et al. Robust carbon dioxide reduction on molybdenum disulphide edges. *Nat. Commun.* **2014**, *5*, 4470.

(148) Asadi, M.; Kumar, B.; Behranginia, A.; Rosen, B. A.; Baskin, A.; Repnin, N.; Pisasale, D.; Phillips, P.; Zhu, W.; Haasch, R.; et al. Robust Carbon Dioxide Reduction on Molybdenum Disulphide Edges. *Nat. Commun.* **2014**, *5*, 4470.

(149) Abbasi, P.; Asadi, M.; Liu, C.; Sharifi-Asl, S.; Sayahpour, B.; Behranginia, A.; Zapol, P.; Shahbazian-Yassar, R.; Curtiss, L. A.; Salehi-Khojin, A. Tailoring the Edge Structure of Molybdenum Disulfide toward Electrocatalytic Reduction of Carbon Dioxide. *ACS Nano* **2017**, *11* (1), 453–460.

(150) Xu, J.; Li, X.; Liu, W.; Sun, Y.; Ju, Z.; Yao, T.; Wang, C.; Ju, H.; Zhu, J.; Wei, S.; et al. Carbon Dioxide Electroreduction into Syngas Boosted by a Partially Delocalized Charge in Molybdenum Sulfide Selenide Alloy Monolayers. *Angew. Chem., Int. Ed.* **2017**, *56*, 9121–9125.

(151) Aljabour, A.; Coskun, H.; Zheng, X.; Kibria, M. G.; Strobel, M.; Hild, S.; Kehrner, M.; Stifter, D.; Sargent, E. H.; Stadler, P. Active Sulfur Sites in Semimetallic Titanium Disulfide Enable CO₂ Electroreduction. *ACS Catal.* **2020**, *10* (1), 66–72.

(152) Feaster, J. T.; Jongerius, A. L.; Liu, X.; Urushihara, M.; Nitopi, S. A.; Hahn, C.; Chan, K.; Nørskov, J. K.; Jaramillo, T. F. Understanding the Influence of [EMIM]Cl on the Suppression of the Hydrogen Evolution Reaction on Transition Metal Electrodes. *Langmuir* **2017**, *33* (37), 9464–9471.

(153) Unke, O. T.; Chmiela, S.; Saucedo, H. E.; Gastegger, M.; Poltavsky, I.; Schütt, K. T.; Tkatchenko, A.; Müller, K.-R. Machine Learning Force Fields. *Chem. Rev.* **2021**, *121*, 10142–10186.

(154) Ko, T. W.; Finkler, J. A.; Goedecker, S.; Behler, J. A Fourth-generation High-dimensional Neural Network Potential with Accurate Electrostatics including Non-local Charge Transfer. *Nat. Commun.* **2021**, *12*, 398.

(155) Gao, A.; Remsing, R. C. Self-consistent Determination of Long-range Electrostatics in Neural Network Potentials. *Nat. Commun.* **2022**, *13*, 1572.

(156) Zhao, Q.; Martirez, J. M. P.; Carter, E. A. Revisiting Understanding of Electrochemical CO₂ Reduction on Cu(111): Competing Proton-Coupled Electron Transfer Reaction Mechanisms Revealed by Embedded Correlated Wavefunction Theory. *J. Am. Chem. Soc.* **2021**, *143*, 6152–6164.

(157) Yang, F.; Elnabawy, A. O.; Schimmenti, R.; Song, P.; Wang, J.; Peng, Z.; Yao, S.; Deng, R.; Song, S.; Lin, Y.; et al. Bismuthene for Highly Efficient Carbon Dioxide Electroreduction Reaction. *Nat. Commun.* **2020**, *11* (1), 1088.

(158) Gao, S.; Lin, Y.; Jiao, X.; Sun, Y.; Luo, Q.; Zhang, W.; Li, D.; Yang, J.; Xie, Y. Partially Oxidized Atomic Cobalt Layers for Carbon Dioxide Electroreduction to Liquid Fuel. *Nature* **2016**, *529* (7584), 68–71.

(159) Kumar, A.; Bui, V. Q.; Lee, J.; Wang, L.; Jadhav, A. R.; Liu, X.; Shao, X.; Liu, Y.; Yu, J.; Hwang, Y.; et al. Moving Beyond Bimetallic-alloy to Single-atom Dimer Atomic-interface for All-pH Hydrogen Evolution. *Nat. Commun.* **2021**, *12*, 6766.

(160) Wang, J.; Liu, W.; Luo, G.; Li, Z.; Zhao, C.; Zhang, H.; Zhu, M.; Xu, Q.; Wang, X.; Zhao, C.; et al. Synergistic Effect of Well-defined Dual Sites Boosting the Oxygen Reduction Reaction. *Energy & Energy Environ. Sci.* **2018**, *11*, 3375–3379.

(161) Lu, Z.; Wang, B.; Hu, Y.; Liu, W.; Zhao, Y.; Yang, R.; Li, Z.; Luo, J.; Chi, B.; Jiang, Z.; et al. An Isolated Zinc–Cobalt Atomic Pair for Highly Active and Durable Oxygen Reduction. *Angew. Chem., Int. Ed.* **2019**, *58*, 2622–2626.

(162) Ren, W.; Tan, X.; Yang, W.; Jia, C.; Xu, S.; Wang, K.; Smith, S. C.; Zhao, C. Isolated Diatomic Ni-Fe Metal–Nitrogen Sites for Synergistic Electroreduction of CO₂. *Angew. Chem., Int. Ed.* **2019**, *58*, 6972–6976.

(163) Zhang, L.; Si, R.; Liu, H.; Chen, N.; Wang, Q.; Adair, K.; Wang, Z.; Chen, J.; Song, Z.; Li, J.; et al. Atomic Layer Deposited Pt-Ru Dual-metal Dimers and Identifying Their Active Sites for Hydrogen Evolution Reaction. *Nat. Commun.* **2019**, *10*, 4936.

(164) Geng, Z.; Liu, Y.; Kong, X.; Li, P.; Li, K.; Liu, Z.; Du, J.; Shu, M.; Si, R.; Zeng, J. Achieving a Record-High Yield Rate of 120.9 for N₂ Electrochemical Reduction over Ru Single-Atom Catalysts. *Adv. Mater.* **2018**, *30*, 1803498.

(165) Han, L.; Liu, X.; Chen, J.; Lin, R.; Liu, H.; Lü, F.; Bak, S.; Liang, Z.; Zhao, S.; Stavitski, E.; et al. Atomically Dispersed Molybdenum Catalysts for Efficient Ambient Nitrogen Fixation. *Angew. Chem., Int. Ed.* **2019**, *58*, 2321–2325.

(166) Zang, W.; Yang, T.; Zou, H.; Xi, S.; Zhang, H.; Liu, X.; Kou, Z.; Du, Y.; Feng, Y. P.; Shen, L.; et al. Copper Single Atoms Anchored in Porous Nitrogen-Doped Carbon as Efficient pH-Universal Catalysts for the Nitrogen Reduction Reaction. *ACS Catal.* **2019**, *9*, 10166–10173.

(167) Wu, Z.-Y.; Karamad, M.; Yong, X.; Huang, Q.; Cullen, D. A.; Zhu, P.; Xia, C.; Xiao, Q.; Shakouri, M.; Chen, F.-Y.; et al. Electrochemical Ammonia Synthesis via Nitrate Reduction on Fe Single Atom Catalyst. *Nat. Commun.* **2021**, *12*, 2870.

(168) Resasco, J.; Chen, L. D.; Clark, E.; Tsai, C.; Hahn, C.; Jaramillo, T. F.; Chan, K.; Bell, A. T. Promoter Effects of Alkali Metal Cations on the Electrochemical Reduction of Carbon Dioxide. *J. Am. Chem. Soc.* **2017**, *139*, 11277–11287.

(169) Thorson, M. R.; Siil, K. I.; Kenis, P. J. A. Effect of Cations on the Electrochemical Conversion of CO₂ to CO. *J. Electrochem. Soc.* **2013**, *160*, F69–F74.

(170) Monteiro, M. C. O.; Dattila, F.; Hagedoorn, B.; García-Muelas, R.; López, N.; Koper, M. T. M. Absence of CO₂ Electroreduction on

Copper, Gold and Silver Electrodes without Metal Cations in Solution. *Nat. Catal.* **2021**, *4* (8), 654–662.

(171) Gu, J.; Liu, S.; Ni, W.; Ren, W.; Haussener, S.; Hu, X. Modulating Electric Field Distribution by Alkali Cations for CO₂ Electroreduction in Strongly Acidic Medium. *Nat. Catal.* **2022**, *5*, 268–276.

(172) Garcés-Pineda, F. A.; Blasco-Ahicart, M.; Nieto-Castro, D.; López, N.; Galán-Mascarós, J. R. Direct Magnetic Enhancement of Electrocatalytic Water Oxidation in Alkaline Media. *Nat. Energy* **2019**, *4* (6), 519–525.

(173) Ren, X.; Wu, T.; Sun, Y.; Li, Y.; Xian, G.; Liu, X.; Shen, C.; Gracia, J.; Gao, H.-J.; Yang, H.; et al. Spin-polarized Oxygen Evolution Reaction under Magnetic Field. *Nat. Commun.* **2021**, *12*, 2608.

(174) Zhong, W.; Qiu, Y.; Shen, H.; Wang, X.; Yuan, J.; Jia, C.; Bi, S.; Jiang, J. Electronic Spin Moment As a Catalytic Descriptor for Fe Single-Atom Catalysts Supported on C₂N. *J. Am. Chem. Soc.* **2021**, *143*, 4405–4413.

(175) Li, Q.-K.; Li, X.-F.; Zhang, G.; Jiang, J. Cooperative Spin Transition of Monodispersed FeN₃ Sites within Graphene Induced by CO Adsorption. *J. Am. Chem. Soc.* **2018**, *140*, 15149–15152.

Recommended by ACS

Atomic Arrangement Modulation in CoFe Nanoparticles Encapsulated in N-Doped Carbon Nanostructures for Efficient Oxygen Reduction Reac...

Ravi Nandan, Karuna Kar Nanda, *et al.*

JANUARY 13, 2021

ACS APPLIED MATERIALS & INTERFACES

READ 

Serendipity for Topological Insulator as Multifunctional Electrocatalyst

Aizhu Wang, Mingwen Zhao, *et al.*

AUGUST 03, 2020

ACS APPLIED ENERGY MATERIALS

READ 

Structural Anisotropy Determining the Oxygen Evolution Mechanism of Strongly Correlated Perovskite Nickelate Electrocatalyst

Meilan Peng, Yifei Sun, *et al.*

MARCH 12, 2021

ACS SUSTAINABLE CHEMISTRY & ENGINEERING

READ 

Introducing Stacking Faults into Three-Dimensional Branched Nickel Nanoparticles for Improved Catalytic Activity

Zeno R. Ramadhan, Richard D. Tilley, *et al.*

JUNE 17, 2022

JOURNAL OF THE AMERICAN CHEMICAL SOCIETY

READ 

Get More Suggestions >